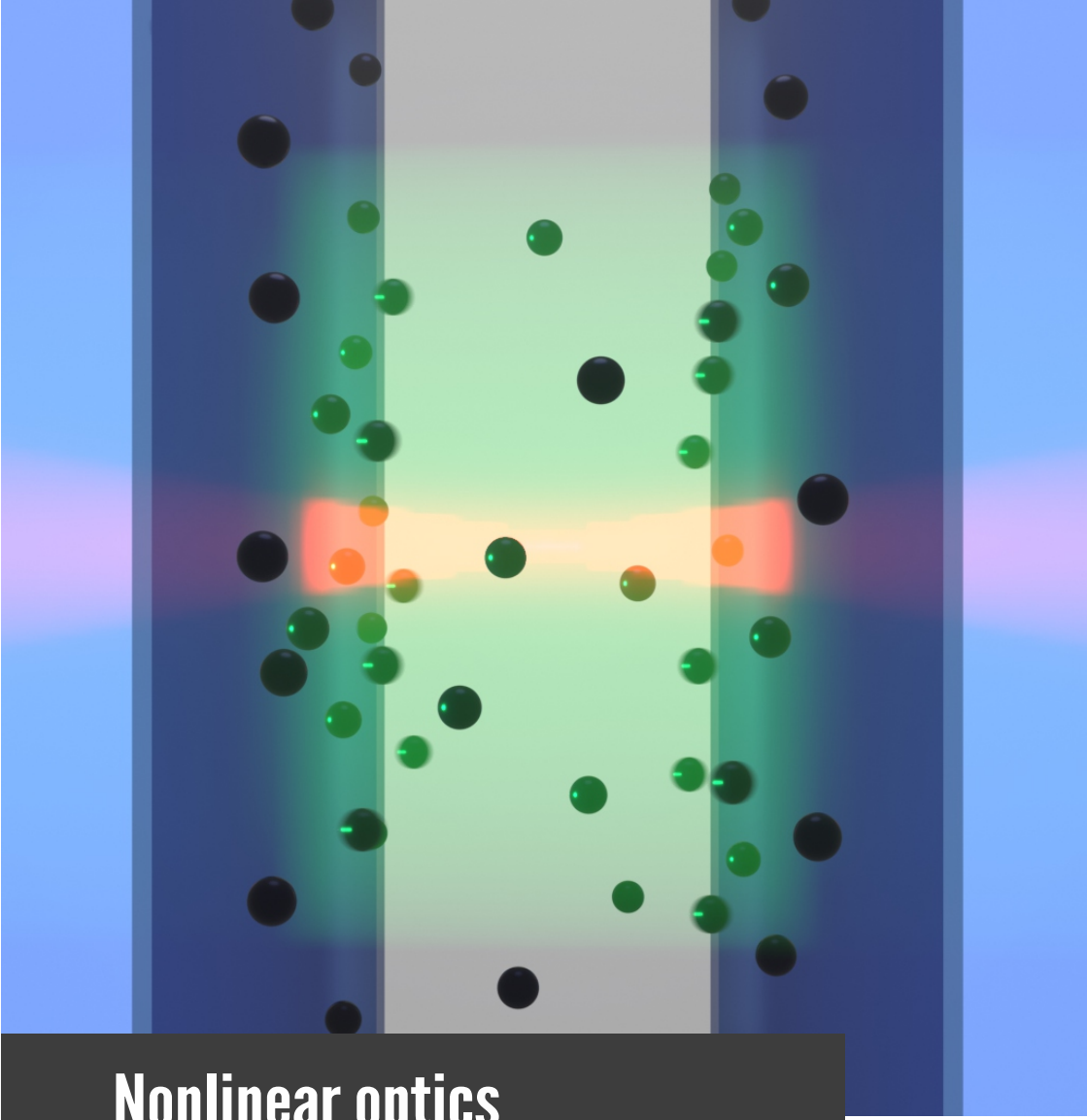

Nonlinear optics in dense atomic vapors

Florian Christaller

In this thesis, two building blocks for our next generation single-photon source, based on thermal rubidium Rydberg atoms, have been investigated. One of these is the coherent excitation of atoms within a four-wave mixing process on the nanosecond timescale. New laser systems, using Yb-doped fiber amplifiers, can drive the so called inverted four-wave mixing cycle with pulses at a MHz repetition rate. A first proof of capabilities shows coherent GHz Rydberg Rabi oscillations of the atomic ensemble.
The second effect is the light-induced atomic desorption, where the atomic density is increased by an off-resonant light pulse in a micrometer sized vapor cell on the nanosecond timescale. The time-resolved transmission spectra show a broadening and line shift due to the high density regime with $n \gg k^3$. Both broadening and line shift are attributed to dipole-dipole interactions between the rubidium atoms. These two building blocks could be the basis for future quantum devices based on the excitation blockade.

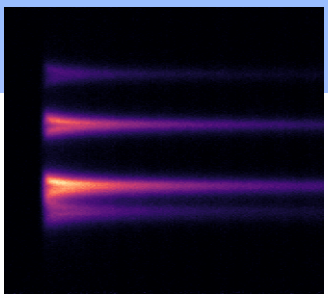

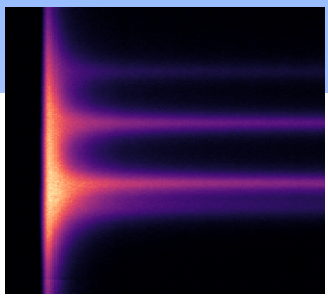

Nonlinear optics in dense atomic vapors

Von der Fakultät Mathematik und Physik der Universität Stuttgart
zur Erlangung der Würde eines Doktors der Naturwissenschaften
(Dr. rer. nat.) genehmigte Abhandlung

vorgelegt von

Florian Joachim Christaller

aus Tübingen

Hauptberichter:	Prof. Dr. Tilman Pfau
Mitberichter:	Prof. Dr. Harald Giessen
Prüfungsvorsitzender:	Prof. Dr. Hans Peter Büchler
Tag der mündlichen Prüfung:	20.04.2022

5. Physikalisches Institut
Universität Stuttgart
2022

List of publications

In the framework of this thesis, the author contributed to the contents of and prepared the following publications:

[1] Oliver de Vries, Marco Plötner, Florian Christaller, Hao Zhang, Annika Belz, Benjamin Heinrich, Harald Kübler, Robert Löw, Tilman Pfau, Till Walbaum, Thomas Schreiber, and Andreas Tünnermann, *Highly customized 1010 nm, ns-pulsed Yb-doped fiber amplifier as a key tool for on-demand single-photon generation*, Opt. Express **28**, 17362–17373 (2020)

[2] Florian Christaller, Max Mäusezahl, Felix Moumtsilis, Annika Belz, Harald Kübler, Hadiseh Alaeian, Charles S. Adams, Robert Löw, and Tilman Pfau, *Transient Density-Induced Dipolar Interactions in a Thin Vapor Cell*, Phys. Rev. Lett. **128**, 173401 (2022)

Further publications are:

[3] Ivan Mirgorodskiy, Florian Christaller, Christoph Braun, Asaf Paris-Mandoki, Christoph Tresp, and Sebastian Hofferberth, *Electromagnetically induced transparency of ultra-long-range Rydberg molecules*, Phys. Rev. A **96**, 011402(R) (2017)

[4] Asaf Paris-Mandoki, Christoph Braun, Jan Kumlin, Christoph Tresp, Ivan Mirgorodskiy, Florian Christaller, Hans Peter Büchler, and Sebastian Hofferberth, *Free-Space Quantum Electrodynamics with a Single Rydberg Superatom*, Phys. Rev. X **7**, 041010 (2017)

Contents

Zusammenfassung

Aufgrund des wachsenden Interesses nach effizienten und skalierbaren universellen Quantencomputern [5] werden immer neue Ansätze entwickelt. Neben anderen Plattformen ist die rein optische Berechnung von quantenmechanischen Systemen basierend auf Einzelphotonen und linearer Optik ein vielversprechender Kandidat [6, 7]. Die Quantenbits (engl.: *qubits*) sind dabei die Polarisation der Photonen, die über lineare optische Netzwerke, bestehend aus Strahlteilern und Phasenschiebern, miteinander wechselwirken.
Die Vorteile von Photonen sind die schnelle und robuste Übermittlung von Informationen mit Lichtgeschwindigkeit bei langer Kohärenzzeit. Deshalb werden Einzelphotonen auch für die Quantenkommunikation [8] verwendet, bei welcher ein vertraulicher Schlüssel mittels Photonen ausgetauscht wird. Für eine Kommunikation über große Distanzen werden dabei sogenannte Quantenverstärker [9, 10] benötigt, welche auf der Erzeugung und Speicherung von Einzelphotonen basieren.
Diese vollständig optischen Plattformen benötigt jedoch Einzelphotonenquellen mit Photonen auf Knopfdruck, hoher Wiederholungsrate, hoher Helligkeit der Quelle (engl.: *brightness*), und schmaler Bandbreite. Atome sind geeignete Kandidaten um schmalbandige und spektral ununterscheidbare Einzelphotonen [11] zu erzeugen. Um die genannten Anforderungen zu erfüllen sind komplexe experimentelle Anwendungen notwendig, wie das Kühlen der Atome zu ultratiefen Temperaturen und die Verwendung von optischen Resonatoren mit hoher Güte [12]. Ein weiterer Ansatz nutzt den Effekt von stark wechselwirkenden Rydberg-Atomen für die Unterdrückung von mehreren, gleichzeitigen Anregungen [13] in einem begrenzten Volumen. Diese sogenannte Rydberg-Blockade ist eine nicht resonante, Van-der-Waals Wechselwirkung zwischen Rydberg-Atomen und führt zu einer optischen Nichtlinearität. Photonen-Antibunching kann sowohl in ultra-kalten Rydberg-Atomen [14, 15] als auch in Raumtemperatur Dampfzellen [16] beobachtet werden.

In unserer Forschungsgruppe werden die Eigenschaften von so einer Raumtemperatur Einzelphotonenquelle, welche den Rydberg-Blockade-Effekt in einer mikroskopischen Dampfzelle ausnutzt, untersucht und optimiert. Um die Rydberg-Atome in einem thermischen atomaren Dampf kohärent zu

untersuchen [17], muss die Anregung der Atome mit intensivem, auf Nanosekundenzeitskala gepulstem Licht [18] erfolgen, sodass das Experiment schneller als die Dephasierung [19] stattfindet, bei welcher die Atome ihre Phaseninformation verlieren. Auf dieser Zeitskala bewegen sich die thermischen Atome im Vergleich zur Größe der Wellenlänge des Lichts fast nicht, weshalb die Atome als quasi eingefroren betrachtet werden können. Ein noch schnelleres Experiment ist nicht vorteilhaft, da dann die Rydberg-Blockade spektral nicht mehr aufgelöst werden kann, was durch das Fourier-Limit gegeben ist.
Die Anregung des Rydberg-Zustandes erfolgt in unserem Fall als Teil eines Vierwellenmischprozesses (engl.: *four-wave mixing, FWM*) [20–22]. Bei diesem Prozess koppeln drei Lichtfelder die Zustände eines Atoms, um die Erzeugung eines vierten Lichtfeldes zu begünstigen. Die Kernidee ist, dass der FWM-Prozess, unter Ausnutzung des Rydberg-Blockade-Effekts in einem begrenzten Anregungsvolumen, Einzelphotonen [16] erzeugt. Das begrenzte Volumen wird durch eine Dampfzelle mit mikroskopischem Abstand der Glasplatten [23] und einem stark fokussierten Anregungslaser umgesetzt. Für einen effizienten FWM-Prozess muss die atomare Dichte in der Dampfzelle hoch genug sein, um kollektive Effekte [24, 25] auszunutzen. Deshalb wird üblicherweise die Dichte in mikro- oder nanometergroßen Zellen [26, 27] mit Hilfe der Temperatur kontrolliert. Um die Temperatur in einem zerstörungsfreien Bereich ($\approx 200\,^{\circ}\mathrm{C}$) zu halten und dennoch hohe atomare Dichten zu erreichen, wird der Effekt der lichtinduzierten Desorption von Atomen (engl.: *light-induced atomic desorption, LIAD*) [28–33] verwendet.
Die Kombination von all den erwähnten Effekten führte zur ersten Beobachtung von Photonen-Antibunching mit Rubidium-Rydberg-Atomen bei Raumtemperatur [16]. Diese Einzelphotonenquelle erreicht eine Photonen-Korrelation von $g^{(2)}(0) = 0{,}19^{+0{,}09}_{-0{,}04}$, eine effektive Wiederholungsrate von 10 Hz und eine Helligkeit der Quelle von $\epsilon = 0{,}0392(5)$. Um diese Eigenschaften, vor allem die Wiederholungsrate, zu verbessern wurde ein anderes FWM Anregungsschema ausgewählt, als Schritt hin zur zweiten Generation unserer Einzelphotonenquelle. Dieses Thema wird im ersten Teil dieser Arbeit behandelt. Im zweiten Teil wird die Verwendung des LIAD Effekts verbessert und charakterisiert, um ein besseres Verständnis des Desorptionsprozesses zu bekommen.

Auf dem Weg zur zweiten Generation unserer Einzelphotonenquelle

Für die zweite Generation der Einzelphotonenquelle wird das Anregungsschema hin zum sogenannten invertierten FWM-Schema geändert. Die Anregung von Rubidium in den Rydberg-Zustand erfolgt mit einem resonanten Zwei-Photonen-Absorptionsprozess. Ausgehend vom Grundzustand $5S_{1/2}$ werden die Atome in den Zwischenzustand $6P_{1/2}$ angeregt [34, 35], der sich von dem bisher verwendeten Zwischenzustand $5P_{1/2}$ unterscheidet [16]. Aus dem Zwischenzustand werden die Atome in einen Rydberg-Zustand angeregt. Durch die Verwendung des Zwischenzustands $6P_{1/2}$ ändern sich die Übergangswellenlänge und die Kopplungsstärke der Zustände, was die Verwendung von neuen Lasersystemen ermöglicht.
In dieser Arbeit werden neue Lasersysteme vorgestellt, welche auf Yb-dotierten Faserverstärkern basieren und Licht bei einer Wellenlänge von ungefähr 1016 nm erzeugen. Die Vorteile von diesen Lasersystemen sind eine Wiederholungsrate von bis zu 1 MHz (bisher waren es 50 Hz) und eine Spitzenleistung von 100 W bei Pulsen mit einer Dauer von Nanosekunden. Erste Beobachtungen der kohärenten Rydberg-Anregung mit diesen Lasersystemen werden gezeigt. Dabei ist eine starke und schnelle Anregung des Zwei-Photonen-Rydberg-Übergangs in Form von GHz-Rabi-Oszillationen [36] zu beobachten. Die Ergebnisse werden mit Messungen des vorherigen Anregungsschemas [18] verglichen, als Richtwert für die Stärke der kohärenten Anregung in den Rydberg-Zustand.

Dynamische dichte-induzierte, dipolare Wechselwirkungen in dünnen Dampfzellen

Im zweiten Teil dieser Arbeit wird der LIAD Effekt genauer untersucht. Eine gängige Anwendung von LIAD ist das Laden von magnetooptischen Fallen [37–39]. Die Anwendung von LIAD zum Umschalten in einen Bereich mit hoher Dichte, in welchem die Dichte n deutlich größer als das Volumen der Wellenzahl k^3 des Lichtfeldes ist, ist bisher unerforscht. Bei atomaren Dichten im Bereich von $nk^{-3} \gg 1$, können resonante dipolare Wechselwirkungen beobachtet werden, welche bereits in dünnen Dampfzellen mit einer Dicke von 30–2000 nm bei einer Temperaturen über 300 °C [26, 27] untersucht wurden. In diesen Systemen wird die Dichte durch

den temperaturabhängigen Dampfdruck bestimmt, wodurch noch höhere Dichten mit Alkalidämpfen bei Temperaturen bis zu 800 °C erreicht werden können [40], was aber wiederum technisch anspruchsvoll ist, da thermische Zerstörung von Glas und optischen Beschichtungen auftritt.
Die dipolaren Wechselwirkungen führen zu einer Veränderung des Grundzustand-Übergangs, welcher sich in einer Selbstverbreiterung (Kollisionsverbreiterung) [41, 42] und einer Verschiebung (kollektiven Lamb-Verschiebung) [43, 44] des Transmissionsspektrums widerspiegelt. Diese kollektive Lamb-Verschiebung beinhaltet die Lorentz-Lorenz-Verschiebung [26, 44] und einen Interferenz Term, verursacht durch das Atomensemble. Aufgrund des kollektiven Effekts hängt die Verschiebung von der Anordnung der Atome im Ensembles ab, was in einem 2D Model [27, 45] beschrieben werden kann.
Durch die Verwendung des LIAD Effekts in einem gepulsten System ist es möglich die Dichte zu erhöhen und so dipolare Wechselwirkungen in einem dynamischen, dichten, atomaren Dampf auf der Zeitskala von Nanosekunden zu untersuchen. In unserem Experiment in einer dünnen Dampfzelle wird die atomare Dichte mit LIAD von einem Bereich ohne Wechselwirkungen mit $nk^{-3} < 1$ in einen Bereich mit Wechselwirkungen mit $nk^{-3} \approx 100$ erhöht. Dabei begrenzt die Dampfzelle das Atomensemble auf eine Dicke von 0,78–6,24 µm.
In dieser Arbeit werden die dipolaren Wechselwirkungen für die beiden Übergänge $5S_{1/2} \rightarrow 5P_{1/2}$ (D_1) und $5S_{1/2} \rightarrow 5P_{3/2}$ (D_2) von Rubidium, mit Blick auf die Verbreiterung und Verschiebung des Transmissionsspektrums, untersucht. Diese beiden Übergänge haben unterschiedliche Dipolmomente, welche einen Einfluss auf die Stärke der Dipol-Dipol-Wechselwirkungen haben.
Neben den Beobachtungen von Wechselwirkungen bei hohen Dichten wird LIAD auch mit geringer Intensität in nicht-wechselwirkenden Systemen ($nk^{-3} < 1$) untersucht. Dabei wird ein erweitertes Verständnis des LIAD Prozesses durch ein Model der desorbierten Atome in einer Simulation erreicht. Vor allem die Geschwindigkeitsverteilung der desorbierten Atome ist grundlegend für zukünftige Anwendungen, welche auf dem gepulsten LIAD-Prozess in Dampfzellen aufbauen.

Ergebnisse dieser Arbeit

Als Teil dieser Arbeit wurde eines der beiden neuen Faser-Verstärker Lasersysteme [1] in das Experiment integriert. Bei einer Wellenlänge von 1016 nm können Pulse mit einer Dauer von 10 ns, einer Wiederholungsrate von 100 kHz und einer Spitzenleistung von 100 W erzeugt werden. Dabei sind Zeit- und Amplitudenfluktuationen auf einem niedrigen Level von < 10 ps und < 1 %. Die damit erzeugten Fourier-limitierten Pulse wurden in einem Experiment verwendet, bei welchem die Zwei-Photonen Rydberg-Anregung gemessen wird.
In diesem 3-Level System wird der Übergang vom $5S_{1/2}$ in den $6P_{1/2}$ Zustand durch einen schwachen Laser getrieben, welcher eine Wellenlänge von 422 nm hat. Der Übergang in den $32S_{1/2}$ Rydberg-Zustand wird durch den starken Puls bei 1016 nm getrieben. Die Kohärente Dynamik in diesem System wurde durch die Messung von Rydberg-Rabi-Oszillationen beobachtet. Dabei oszilliert die Besetzung der atomaren Zustände zwischen dem mittleren und dem Rydberg-Zustand mit einer Rabi-Frequenz von ≈ 1 GHz. Diese Messung zeigt die Möglichkeiten der neuen Lasersysteme zur kohärenten Anregung von Rydberg-Zuständen im invertierten FWM-Schema auf einer Zeitskala unter einer Nanosekunde.

Im zweiten Teil der Arbeit wurde der LIAD-Effekt [2] genauer untersucht. Dabei wurde die optische Tiefe in Abhängigkeit der Zeit nach dem LIAD Puls und der Laserverstimmung gemessen, welche proportional zur atomaren Dichte ist. Durch den Nanosekundenpuls des LIAD Lasers kann die atomare Dichte von $n_{\mathrm{temp}} \approx 10^{14}\,\mathrm{cm}^{-3}$ auf $n_{\mathrm{LIAD}} \approx 10^{16}\,\mathrm{cm}^{-3}$ erhöht werden. Durch diese Erhöhung der Dichte ist $n \ll k^3$, wodurch dipolare Wechselwirkungen wenige Nanosekunden nach dem Puls studiert werden können. Für den D_2 Übergang wurde eine Verbreiterung von $\Gamma_{\mathrm{self},D_2} \approx 840\Gamma_0$ und eine Dipol-Dipol Verschiebung von $\Delta_{\mathrm{dd},D_2} \approx -90\Gamma_0$ beobachtet bei $t = 2$ ns nach dem Desorptionspuls und einer Desorptionsintensität von $I = 317(32)\,\mathrm{MW\,cm}^{-2}$. Dabei ist $\Gamma_0 = 2\pi \times 6{,}07$ MHz [46] die natürliche Linienbreite des D_2 Übergangs.
Ein Vergleich mit dem Model für dipolare Wechselwirkungen von Atomen im Gleichgewichtszustand liefert eine gute Übereinstimmung zu unseren dynamischen Dichte-induzierten Wechselwirkungen. Ob die dipolare Wechselwirkung selbst dynamische Effekte besitzt kann mit unserem Ex-

periment weder belegt, noch widerlegt werden, da die zu schlechte Zeitauflösung und die dynamische Änderung der Dichte solche Effekte überlagern. Zusätzlich war es möglich den Desorptionsprozess bei geringer Dichte zu untersuchen. Dafür wurde ein kinematisches Model entwickelt, welches den Desorptionsprozess nachbilden soll. Mithilfe einer Monte-Carlo Simulation wurde die optische Tiefe eines Atomensembles numerisch berechnet und mit der Messung verglichen. Dabei konnte eine Geschwindigkeitsverteilung der desorbierten Atome bestimmt werden, welche der Kombination einer Maxwell-Boltzmann Verteilung mit dem $\cos(\theta)$-Knudsen Gesetz [47] entspricht. Folglich werden die Atome nicht isotrop, sondern wahrscheinlicher entlang des Desorptions-Laserstrahls gerichtet abgelöst. Für eine gute Übereinstimmung mit der Messung wurde eine Re-Desorption eines Atoms, nachdem es in eine Wand eingeschlagen ist, in die Simulation integriert. Die Simulation liefert ein mögliches Model des Desorptionsprozesses, welches mit weiteren Effekten verbessert werden kann, um genauere Vorhersagen treffen zu können.

Introduction

Due to the increasing interest for an efficient and scalable quantum computer, various competing architectures for universal quantum computers [5] are actively being developed and investigated. Among other platforms, all-optical quantum computation based on single photons and linear optics is a promising candidate [6, 7]. There, the quantum bits (qubits) are the polarization of the photons, which are interacting with each other via linear optical networks, consisting of readily available beam splitters and phase shifters.
The benefits of photons lie in the fast, robust transport of quantum information at the speed of light and rather long coherence times. This makes single photons as qubits powerful to use for quantum information processing and quantum communication [8]. For an efficient and stable operation over long distances quantum repeaters [9, 10] are required, which are based on the generation and storage of single photons, ideally using the same architecture.
All these purely optical platforms however require on-demand, high rate, high brightness, narrow linewidth single-photon sources. Among other systems, atoms are well suited to produce narrow linewidth and spectrally indistinguishable single photons [11]. Meeting all aforementioned requirements demands complex experimental techniques, like cooling the atoms to ultra-cold temperatures and placing them inside of high-finesse cavities [12]. Another approach uses strongly interacting Rydberg atoms to suppress multiple simultaneous excitations [13]. The so called Rydberg blockade is an off-resonant, van der Waals-type interaction between Rydberg atoms and introduces an optical non-linearity. Photon antibunching has previously been observed in both ultra-cold Rydberg atom clouds [14, 15] and room-temperature vapor cells [16].

Our group investigates and optimizes the properties of such a room-temperature single-photon source. To coherently observe Rydberg atoms in thermal atomic ensembles [17], the excitation of the atoms has to be performed with intense, nanosecond-pulsed light fields to drive the atoms [18] faster than any dephasing [19]. On this timescale, the thermal atoms al-

most stay at the same location compared to the wavelength of the light such that they can be viewed as quasi-frozen. Even faster operation is not advantageous, since the Rydberg blockade would not be resolved spectrally due to the Fourier-limit.
The excitation of the Rydberg state is performed within a four-wave mixing (FWM) [20–22] cycle. In this process, three light fields coupling the states of an atom enhance the generation of a fourth light field, which closes the cycle. By enforcing the Rydberg blockade effect through a confined excitation volume, the FWM process generates antibunched photons [16]. This confined excitation volume is realized by a microscopic spaced vapor cell [23] and a tightly focused excitation laser. For an efficient FWM process, the atomic density in the vapor cell has to be accordingly high to exploit collective effects [24, 25]. Therefore, the atomic density in a micro- or nano-cell [26, 27] is commonly controlled via the temperature of the cell. To keep the temperature in a non-destructive range ($\approx 200\,^{\circ}\mathrm{C}$) and still reach high atomic densities, light-induced atomic desorption (LIAD) [28–33] is used.
The combination of all mentioned effects led to the first observation of single photons generated with room-temperature rubidium Rydberg atoms [16]. This single-photon source reaches a photon-pair correlation of $g^{(2)}(0) = 0.19^{+0.09}_{-0.04}$, an effective repetition rate of 10 Hz and a brightness of $\epsilon = 0.0392(5)$. To improve these features, especially the repetition rate, a different FWM excitation scheme is chosen as a step towards the second generation single-photon source based on thermal Rydberg atoms. This topic is treated in the first part of this thesis. In the second part, the use of the LIAD effect is improved and characterized to have a better understanding of the desorption process.

Towards the second generation single-photon source

For our second generation single-photon source the excitation scheme is changed to the so called inverted FWM scheme. The excitation of rubidium into the Rydberg state is performed with a resonant two-photon absorption process. Starting from the ground state $5S_{1/2}$, the atoms are excited to the $6P_{1/2}$ intermediate state [34, 35], which is different to the previously used $5P_{1/2}$ intermediate state [16]. From the intermediate

state, the atoms are excited into a Rydberg state. By using the $6P_{1/2}$ intermediate state, the transition wavelengths and coupling strength of the states change, which allows the usage of high repetition rate laser systems.
In this work, these new laser systems are presented, which are based on Yb-doped fiber amplifiers with a wavelength around 1016 nm. The advantages of these laser systems are a repetition rate up to 1 MHz and a peak power of 100 W for nanosecond long pulses. First coherent observations of the Rydberg excitation are shown, exhibiting an intense and fast driving of the two-photon Rydberg excitation, which is observable in form of GHz Rabi oscillations [36]. The results are benchmarked against measurements in the previous excitation scheme [18].

Transient density-induced dipolar interactions in a thin vapor

In the second part of this thesis, the LIAD effect is studied in more detail. LIAD is commonly used as an unconventional atom source, e.g. to load magneto optical traps [37–39]. However, the application of LIAD to reach a dense regime, where the density n is significantly larger than the wavenumber cubed k^3 of the coupling light field, is so far unexplored. By reaching a regime with $nk^{-3} \gg 1$, resonant dipolar interactions are observable, which already have been studied in systems with a high steady-state density in thin vapor cells with a thickness of 30–2000 nm at temperatures above 300 °C [26, 27]. It is possible to prepare even higher densities with alkali vapors at temperatures up to 800 °C [40], which is however technically challenging due to destruction of glass and optical coatings.
The dipolar interactions lead to a change of the ground-state transition, resulting in a self-broadening (collisional broadening) [41, 42] and a collective Lamb shift [43, 44] of the transmission spectra. This collective Lamb shift includes the Lorentz-Lorenz shift [26, 44] and a cavity-induced term caused by the collective ensemble of atoms. The shift depends on the geometry of the atom ensemble and can be described in our system in a 2D model [27, 45].
By using the LIAD effect in a pulsed fashion, it becomes possible to study dipolar interactions in a transient dense atomic vapor on nanosecond timescales. In our experiment the atomic density is increased into the

dense regime (up to $nk^{-3} \approx 100$) in a thin vapor by LIAD. The vapor cell confines the atomic ensemble to a thickness of 0.78–6.24 µm.
In this work, the dipolar interactions for the two transitions D_1: $5S_{1/2} \rightarrow 5P_{1/2}$ and D_2: $5S_{1/2} \rightarrow 5P_{3/2}$ of rubidium are investigated with respect to broadenings and shifts of the transmission spectra. There, the properties of the dipole-dipole interactions are studied based on their different transition dipole moments.
Besides the emerging interactions at high densities, LIAD with low intensity in the non-interacting regime ($nk^{-3} < 1$) is studied. There, a better understanding of the desorption process is obtained by modeling the desorbed atoms in a simulation. Knowledge about the microscopic velocity distribution of the desorbed atoms is fundamental for further applications based on the pulsed LIAD process in atomic vapor cells.

Part I

Towards the second generation single-photon source

Outline

This part of the thesis is about the path towards the second generation single-photon source based on our approach of using thermal rubidium Rydberg atoms combined with inverted four-wave mixing (FWM).
In the first chapter, the principle idea of our single-photon source is presented. This is discussed in detail by Fabian Ripka in his PhD thesis [48]. Based on the experiment by Fabian Ripka, the second generation of the experiment is planned, where the limitations of the old laser systems, like a low repetition rate and high jitters, are resolved. This is primarily done by choosing a different excitation scheme, which is based on other atomic states and therefore other laser sources are required. The selected FWM scheme, including a Rydberg state, is described in the second chapter. For the excitation into a Rydberg state, laser systems based on fiber amplifiers are used. The characterization of these laser systems is discussed in the third chapter. In the last chapter, one of the fiber amplifiers is used to excite atoms into the Rydberg state, where Rabi oscillations are observed on the nanosecond timescale.
Central results of this part are published in [1] and have been investigated in our group by Annika Belz [49].

Chapter 1

Principle idea of single-photon generation

1.1 General overview

With the idea of quantum computation [5], a need for single-photon generation arises. These single photons are used as the quantum bits (qubits) in the optical network of a quantum computer [6, 7].
But it is not straight forward, to generate single photons, which are observed as antibunching of the photon emission [11]. There are several systems present, based on quantum dots in semiconductors [50], color-centers in diamond [51] and single molecules [52]. The emitted single photons from these systems are spectrally broad and efficiently generated only at cryogenic temperatures. Other systems use atoms [11] or ions [53] as single-photon source. There, the photons are spectrally narrow, but the systems are often based on ultra-cold ensembles. However, at room temperature, there are heralded sources available, e.g. the process of parametric down-conversion [54], which generates a pair of photons. A drawback of these sources is the spontaneous emission of the photons at random times, which are therefore not suited for a synchronous computation.
By using the excitation of atoms as single-photon source, the emission of photons can be controlled via the excitation lasers in a pulsed fashion. A Rydberg excitation in an ensemble of atoms will lead to the so called Rydberg blockade effect, where only one excitation to the Rydberg state within a certain volume is possible [13]. In a small-enough atomic en-

semble, the Rydberg blockade will eventually lead to the emission of a antibunched photon. These kinds of single-photon sources were first realized in ultra-cold atom clouds [14, 15] and recently also in thermal vapor cell experiments [16].

1.2 Our approach to generate single photons

For our single-photon source, several components and effects have to play together. The key ingredients are: a micro-cell filled with an alkali-vapor, the effect of light-induced atomic desorption to increase the atomic density, a volume confinement by a tightly focused excitation laser and by the wedged micro-cell smaller than the Rydberg blockade radius to allow only one excitation, and a pulsed excitation on the nanosecond timescale to stay in the quasi frozen regime and to be faster than any dephasing.
In our group in 2018, a first demonstration of an on-demand single-photon source with room-temperature atoms [16] was built, based on the components and effects above. The brightness of this source was $\epsilon = 0.0392(5)$, which is not high compared to other single-photon sources [55]. The limits are a low efficiency during the excitation and imperfect temporal and spatial overlap of the light modes. To overcome these issues, a different excitation scheme is implemented, where up-to-date laser systems can be used. This scheme allows a stronger coupling to the Rydberg state, enhancing the brightness of the single-photon source.
There are other properties, which can be improved, e.g. the repetition rate of the single-photon generation and the purity of the photons (correlation between photons should go to zero). Some inherent features of our approach can not be achieved using other single photon sources. For example, our system emits single photons on-demand and they can be interfaced with atom-based memories. The actual apparatus, without the lasers and optics, is small, as only a small vapor cell at room temperature is needed. This makes our approach scalable and integrable.
A schematic illustration of our single-photon generation approach can be see in figure 1.1. In the following, the main components and effects are summarized, which are needed to build this type of single-photon source.

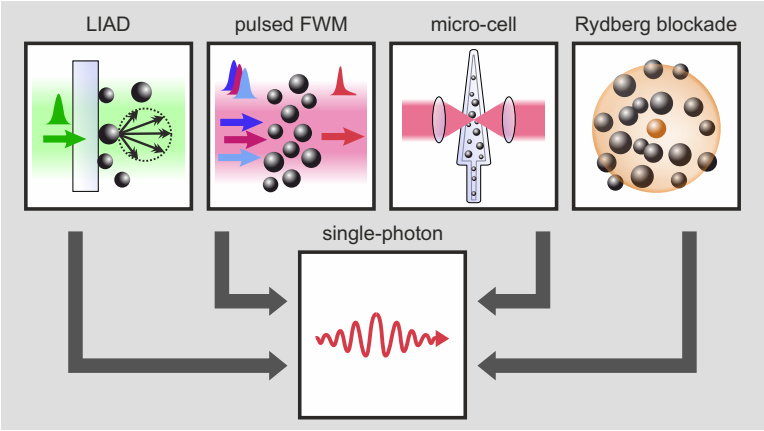

Figure 1.1 Single-photon generation components and effects: The four main components and effects are illustrated (top row), which are essential for our approach to generate single photons. With light-induced atomic desorption (LIAD), the atoms are desorbed from the glass surface. The atoms are driven via pulsed four-wave mixing (FWM). For the volume confinement, a micro-cell and focused laser beam is used. The included Rydberg state leads to a Rydberg blockade of the atom ensemble. Finally, all components and effects combined lead to the generation of a single photon (bottom).

1.2.1 Confinement of the volume

The micro-cell and a tight focus of the first excitation laser lead to a strong confinement of the excitation volume. The cell has a thickness of one micrometer, leading to a confinement along the optical axis. A further description and characterization of the micro-cell is shown in section 6.2. Using a focusing lens with a short focal length and a high numerical aperture (high-NA), the first excitation laser is strongly focused and has a beam waist radius of approximately 1 µm in the focus. This confines the volume in transversal direction of the optical axis.

1.2.2 Rydberg blockade

The radius of the confined volume is on the same order of magnitude as the so called Rydberg blockade radius, which defines a volume, where only one Rydberg excitation is possible. For example, the Rydberg 40S state has a blockade radius of approximately 1 µm for an excitation with a bandwidth of $\approx 400\,\mathrm{MHz}$.
This Rydberg blockade is used as optical non-linearity to generate a single photon with the excitation of a single Rydberg atom in the confined volume.

1.2.3 Light-induced atomic desorption

The light-induced atomic desorption (LIAD) effect is used to desorb atoms, which are sitting on the glass surfaces in the vapor cell, to temporally increase the density. In our setup, a strong off-resonant green laser pulse leads to the desorption of the atoms on the nanosecond timescale. As this LIAD effect is a key tool for the single-photon source, the pulsed LIAD effect is characterized in more detailed as well as the observed dipolar effects in the transient high-density regime.
A description of the measurements with LIAD and a detailed evaluation of the observed effects can be found in part II.

1.2.4 Four-wave mixing

The effect of FWM occurs if three transitions are driven by light fields, while the remaining transition, closing the excitation loop, emits coherent photons.
In our case, a diamond shaped excitation scheme is used, including a Rydberg state. Further details about our FWM scheme can be read in chapter 2.

1.2.5 Pulsed excitation

Another important fact is the pulsed, on-demand excitation of the atoms on the nanosecond timescale. As thermal atoms are used, their velocity is rather high ($\bar{v} \approx 300\,\mathrm{m\,s^{-1}}$ at 200 °C), compared to ultra-cold experiments. To overcome the motion of the atoms, the excitation is done with a short

pulse, while the measurement on the atoms is performed within a few nanoseconds. Therefore, the observations are in the so called quasi frozen regime, where the thermal motion is negligible, within the experiment cycle.
Another factor is the dephasing of the coherent atomic excitation due to the thermal motion. The phases of the atoms in the collective ensemble are scrambled after a few nanoseconds, making the observation of coherent effects, like the Rydberg blockade, almost impossible.
The key-tools for the single-photon source are the pulsed laser systems driving the Rydberg transitions and will therefore be described in more detail in chapter 3.

Chapter 2

Four-wave mixing with Rydberg states

To describe the excitation of atoms with a light field, which is fundamental for the FWM process, the theory for the atom-light interaction is formulated. As our FWM process includes a Rydberg state, the properties of Rydberg atoms are discussed afterwards. Finally, the FWM process is explained.

2.1 Atom-light interaction

In order to understand the physical processes of the interaction between an atom and a light field, a theoretical treatment of the atom-light interaction is necessary. The theory of the atom-light interaction is well established in many standard atomic physics textbooks. The formalism presented here provides the basic idea of the theory to understand the measurements and simulations within this thesis. The treatment of the atom-light interaction follows the notation in [48, 49, 56].

2.1.1 Density matrix formalism

In a quantum mechanical system, an atom is characterized by an energy eigenvalue (energy level) $\mathcal{E}_i = \hbar\omega_{\mathrm{a},i}$ for a corresponding eigenstate $|i\rangle$, where $\hbar$ is the reduced Planck constant and ω_{a} the resonance frequency of the atom. Without any external fields or internal dissipation effects, the

Hamiltonian of the atom is given by

$$H_{\text{atom}} = \sum_i \mathcal{E}_i \left|i\right\rangle \left\langle i\right| . \tag{2.1}$$

To include the interaction between a classical light field $\boldsymbol{E}$ and an atom, a second Hamiltonian is used, which treats the interaction as follows

$$H_{\text{int}} = -\boldsymbol{d} \cdot \boldsymbol{E} , \tag{2.2}$$

where $\boldsymbol{d}$ is the dipole operator. The system is described by the sum of the Hamiltonians with

$$H = H_{\text{atom}} + H_{\text{int}} . \tag{2.3}$$

The state in an atomic ensemble is not a pure but rather a mixed quantum state. There it is not possible to describe the system as a superposition of all eigenstates of the atom. But for a mixed quantum state, the density matrix operator

$$\rho = \sum_{i,j} \rho_{ij} \left|i\right\rangle \left\langle j\right| , \tag{2.4}$$

can be used. In this density matrix, the diagonal elements with ρ_{ii} contain the information about the population of state $|i\rangle$ and the off-diagonal elements with ρ_{ij} contain the so called coherence between the states $|i\rangle$ and $|j\rangle$. The density operator is hermitian $\rho = \rho^\dagger$ and the overall population in the atom is conserved by $\text{trace}(\rho) = 1$.
The time evolution of the system, where the density matrix as well as the Hamiltonian are time-dependent, follows the von Neumann equation (e.g. [57])

$$\frac{\partial \rho(t)}{\partial t} = -\frac{\mathrm{i}}{\hbar} \left[H(t), \rho(t)\right] , \tag{2.5}$$

where the brackets $[\cdot, \cdot]$ are the commutator. This equation describes the coherent coupling between states of an atom and a light field.

2.1.2 Decoherence effects

In the real world, there are several decoherence processes, which also influence the system. The two main effects, considered in this treatment, are the decay and the dephasing of states.

The decay rate Γ of a state includes all possible decay paths into the ground state. This is also known as the spontaneous decay Γ_0, which is anti-proportional to the natural lifetime. A decay means, that the population in the initial state $|i\rangle$ decreases, while the population in the final state $|f\rangle$ increases with Γ_{if}. Therefore, also the coherence changes, which is a measure of the correlation of the two states.
This is different for a dephasing process γ_{deph}, where the population stays unaffected and only the coherence changes. In other words, the phase of the atom in the initial state changes, such that it has a different phase than the final state. A dephasing can be caused by collisions of atoms, or by motion-induced dephasing [58].
Both decoherence effects can be described by the so-called Lindblad operator [59]

$$L(\rho(t)) = L_{\mathrm{decay}}(\rho(t)) + L_{\mathrm{deph}}(\rho(t))\,. \tag{2.6}$$

The two terms are

$$\begin{aligned} L_{\mathrm{decay}} &= \sum_{\{i\to f\}} \Gamma_{i\to f}\left(\sigma_{i\to f}\rho\sigma_{i\to f}^{\dagger} - \frac{1}{2}\left\{\sigma_{i\to f}^{\dagger}\sigma_{i\to f},\rho\right\}\right) \\ &= \sum_{\{i\to f\}} \Gamma_{i\to f}\left(|f\rangle\,\rho_{ii}\,\langle f| - \frac{1}{2}\left\{|i\rangle\,\langle i|\,,\rho\right\}\right) \end{aligned} \tag{2.7}$$

and

$$\begin{aligned} L_{\mathrm{deph}} &= \sum_{i} \gamma_{i,\mathrm{deph}}\left(\sigma_{i\to i}^{\dagger}\rho\sigma_{i\to i} - \frac{1}{2}\left\{\sigma_{i\to i}^{\dagger}\sigma_{i\to i},\rho\right\}\right) \\ &= \sum_{i} \gamma_{i,\mathrm{deph}}\left(|i\rangle\,\rho_{ii}\,\langle i| - \frac{1}{2}\left\{|i\rangle\,\langle i|\,,\rho\right\}\right)\,, \end{aligned} \tag{2.8}$$

where $\sigma_{i\to f} = |f\rangle\,\langle i|$ is the atomic transition operator and the curly brackets $\{\cdot,\cdot\}$ are the anti-commutator.
Including the decoherence effects into the system leads to the von Neumann equation in Lindblad form

$$\frac{\partial\rho(t)}{\partial t} = -\frac{\mathrm{i}}{\hbar}\left[H(t),\rho(t)\right] + L(\rho(t))\,. \tag{2.9}$$

2.1.3 Rotating wave approximation

In order to solve equation 2.9 it is useful to transform the system into a rotating frame. This frame oscillates with the frequency of one of the involved light fields ω_1. All other light fields and interactions will thereby have slow frequencies in the rotating frame. The transformation into the rotating frame and the neglect of fast oscillating terms (oscillating with $2\omega_1$) is called rotating wave approximation (RWA). Therefore, the unitary transformation operator U is used to transform the density matrix by

$$\tilde{\rho} = U^\dagger \rho U \,. \tag{2.10}$$

Operators in the rotating frame are denoted by a tilde ($\sim$). The transformed Hamiltonian (for more details see [60]) is given by

$$\tilde{H} = U^\dagger H U - \mathrm{i}\hbar U^\dagger \frac{\partial U}{\partial t} \,. \tag{2.11}$$

The Lindblad operator is not affected by the transformation, resulting in $\tilde{L}(\tilde{\rho}) = L(\tilde{\rho})$. The transformed von Neumann equation has almost the same form as equation 2.9

$$\frac{\partial \tilde{\rho}(t)}{\partial t} = -\frac{\mathrm{i}}{\hbar}\left[\tilde{H}(t), \tilde{\rho}(t)\right] + L(\tilde{\rho}(t)) \,. \tag{2.12}$$

The transformation matrix U is diagonal with the form $U = \exp(\mathrm{i}\varphi_{1\to i}\,|i\rangle\langle i|)$, where $\varphi_{1\to i}$ is the summed phase over all possible transition "paths" from state $|1\rangle$ to $|i\rangle$ (for more details see [48]). Finally, the transformed entries of the density matrix are

$$\tilde{\rho}_{ii} = \rho_{ii} \quad \text{and} \quad \tilde{\rho}_{ij} = \rho_{ij} e^{\mathrm{i}\varphi_{i\to j}} \,. \tag{2.13}$$

The diagonal elements are unaffected, while the off-diagonal elements acquire the phases due to the transformation to the rotating frame, which are slowly varying terms.
The diagonal entries of the transformed atom Hamiltonian can be described via the sum of detunings Δ_{ab} between the resonance frequency ω_a

of the atom and the frequency of the light field ω_l with

$$\begin{aligned}(\tilde{H}_\mathrm{atom})_{ii} &= \hbar\omega_{\mathrm{a},i} \pm \sum_{\{ab|1\to i\}} \hbar\omega_{\mathrm{l},ab} \\ &= \mp \sum_{\{ab|1\to i\}} \hbar\Delta_{ab}\,.\end{aligned} \tag{2.14}$$

There, ab should indicate, that the overall transition can be split into many sub-transitions from $|a\rangle$ to $|b\rangle$ with the sign of each detuning Δ_{ab} depending on whether a photon gets absorbed or emitted (see also [48]). For the off-diagonal entries of the transformed Hamiltonian, the light field $\boldsymbol{E}$ has to considered. For simplification, the light field is assumed to be a plane wave propagating in z direction

$$\begin{aligned}\boldsymbol{E}_{ij}(t) &= \frac{1}{2}\left(E_{0,ij}e^{\mathrm{i}(\omega_{\mathrm{l},ij}t - k_{ij}z)} + c.c.\right)\boldsymbol{e_z} \\ &= \frac{1}{2}\left(E_{0,ij}e^{\mathrm{i}\varphi_{ij}} + E^*_{0,ij}e^{-\mathrm{i}\varphi_{ij}}\right)\boldsymbol{e_z}\,,\end{aligned} \tag{2.15}$$

where $k = |\boldsymbol{k}|$ is the wavenumber of the light, as the wavevector $\boldsymbol{k}$ is parallel to the z direction. The light field is plugged into equation 2.2 to calculate the transformed interaction Hamiltonian

$$\begin{aligned}(\tilde{H}_\mathrm{int})_{ij} &= -\boldsymbol{d}_{ij}\cdot\boldsymbol{E}_{ij}(t)\,e^{-\mathrm{i}\varphi_{ij}} \\ &= -d_{ij}\frac{1}{2}\left(E_{0,ij} + E^*_{0,ij}e^{-\mathrm{i}2\varphi_{ij}}\right)\,,\end{aligned} \tag{2.16}$$

where d_{ij} is the dipole matrix element of the transition from $|i\rangle$ to $|j\rangle$ and the last term oscillates at twice the light frequency ($e^{-\mathrm{i}2\varphi_{ij}} \propto e^{-\mathrm{i}2\omega_{\mathrm{l},ij}t}$) which is neglected in the RWA. With the definition of the Rabi frequency

$$\Omega_{ij} = -\frac{d_{ij}E_{0,ij}}{\hbar}\,, \tag{2.17}$$

the transformed interaction Hamiltonian becomes

$$(\tilde{H}_\mathrm{int})_{ij} = -d_{ij}\frac{1}{2}E_{0,ij} = \frac{1}{2}\hbar\Omega_{ij}\,. \tag{2.18}$$

2.1.4 Rabi frequency

The Rabi frequency is a measure of the strength of the coupling between two states. The electric field of the coupling light is assumed to be a Gaussian beam. Therefore, the electric field in the focus of the Gaussian beam with a $1/e^2$ waist radius w and the power P is defined as

$$E_0 = \sqrt{\frac{4P}{c\epsilon_0 \pi w^2}}\,, \tag{2.19}$$

where c is the speed of light and ϵ_0 the vacuum permittivity. Using this expression, the Rabi frequency from equation 2.17 can be written as

$$\Omega_{ij} = -\frac{d_{ij}}{\hbar}\sqrt{\frac{4P}{c\epsilon_0 \pi w^2}}\,. \tag{2.20}$$

2.1.5 Two-level atom

The simplest system to observe atom-light interaction is an atom with two states coupled via a light field. The ground state $|1\rangle = \left(\begin{smallmatrix}1\\0\end{smallmatrix}\right)$ and the excited state $|2\rangle = \left(\begin{smallmatrix}0\\1\end{smallmatrix}\right)$ have the energy eigenvalues of $\mathcal{E}_1 = \hbar\omega_{\mathrm{a},1}$ and $\mathcal{E}_2 = \hbar\omega_{\mathrm{a},2}$, while the transition frequency is $\omega_{\mathrm{a},12} = \omega_{\mathrm{a},2} - \omega_{\mathrm{a},1}$. The excited state decays with Γ and dephasing effects are neglected in this basic example. The energy of the light field is $\hbar\omega_{\mathrm{l},12}$, which is used to define the detuning as $\Delta = \omega_{\mathrm{l},12} - \omega_{\mathrm{a},12}$.

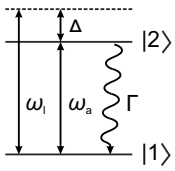

Figure 2.1 Two-level atom: The variables are explained in the text.

Using this system, shown in figure 2.1, the Hamiltonian and the Lindblad operator result from equation 2.3 and equation 2.6, which are transformed into the rotating frame, as

$$\tilde{H} = \hbar \begin{pmatrix} 0 & \frac{1}{2}\Omega \\ \frac{1}{2}\Omega^* & \Delta \end{pmatrix} \tag{2.21}$$

and

$$L(\tilde{\rho}) = \Gamma \begin{pmatrix} \tilde{\rho}_{22} & -\frac{1}{2}\tilde{\rho}_{12} \\ -\frac{1}{2}\tilde{\rho}_{21} & -\tilde{\rho}_{22} \end{pmatrix} . \tag{2.22}$$

With those operators, the von Neumann equation can be set up, according to equation 2.12, to gain four coupled differential equations for the entries of the density matrix

$$\frac{\partial}{\partial t}\tilde{\rho}_{11} = \Gamma\tilde{\rho}_{22} - \mathrm{Im}\left(\tilde{\rho}_{12}\Omega^*\right) , \tag{2.23a}$$

$$\frac{\partial}{\partial t}\tilde{\rho}_{12} = \left(-\frac{\Gamma}{2} - \mathrm{i}\Delta\right)\tilde{\rho}_{12} - \mathrm{i}\frac{\Omega}{2}\left(\tilde{\rho}_{22} - \tilde{\rho}_{11}\right) , \tag{2.23b}$$

$$\frac{\partial}{\partial t}\tilde{\rho}_{21} = \left(-\frac{\Gamma}{2} + \mathrm{i}\Delta\right)\tilde{\rho}_{12} + \mathrm{i}\frac{\Omega}{2}\left(\tilde{\rho}_{22} - \tilde{\rho}_{11}\right) , \tag{2.23c}$$

$$\frac{\partial}{\partial t}\tilde{\rho}_{22} = -\Gamma\tilde{\rho}_{22} + \mathrm{Im}\left(\tilde{\rho}_{12}\Omega^*\right) . \tag{2.23d}$$

These differential equations are also called optical Bloch equations. The time evolution of these equations, for a system with the initial population

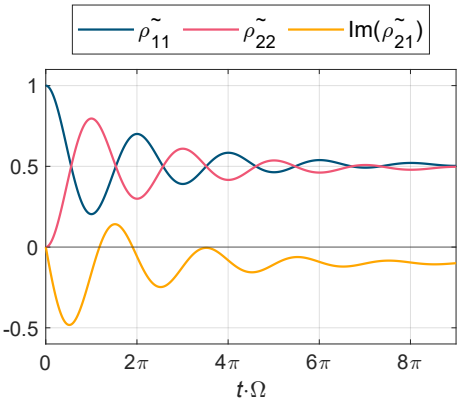

Figure 2.2 Two-level atom evolution: Time evolution of the optical Bloch equations for a two-level atom. The population is initially in the ground state $\tilde{\rho}_{11}(t = 0) = 1$ and starts to oscillate between the ground (blue) and excited (red) state with the coupling Rabi frequency Ω. The decay of $\Gamma = 0.2\,\Omega$ leads to a damping of the oscillations. The imaginary part of the coherence (yellow) also oscillates with the Rabi frequency.

in the ground state $\tilde{\rho}_{11}(t = 0) = 1$, a detuning of $\Delta = 0$, a Rabi frequency of Ω, and a decay of $\Gamma = 0.2\,\Omega$, is shown in figure 2.2.
The populations $\tilde{\rho}_{11}$ and $\tilde{\rho}_{22}$ oscillate with the Rabi frequency between the two atomic states. This coherent effect of population transfer is called Rabi oscillation. Due to the decay, the oscillation is damped and reaches a so called steady-state value for larger times.
The imaginary part of the coherence $\mathrm{Im}(\tilde{\rho}_{21})$ is proportional to the transmission [61] of the coupling light through an atom. Consequently, the transmission also oscillates with the Rabi frequency, as shown in figure 2.2. In a real experiment, the transmission is often the only measurable quantity, which can therefore be used to characterize the system.
The presented atom-light interaction theory is the basis for further simulations within this thesis. The simple two-level atom can be straightforward extended to four atomic states, which are needed to simulate the FWM process including a Rydberg state.

2.2 Rydberg atom

One central effect of our single-photon source is the Rydberg blockade effect. To understand the underlying physics, the properties of Rydberg atoms and the resulting blockade are presented briefly.
A Rydberg atom [62] is an atom, where a single or multiple electrons, normally from the outermost shell, are excited into a high lying energy state. The electron is transferred into a large electron orbit, such that the nucleus and the inner electrons of the Rydberg atom can be considered as positively charged core. This core and the Rydberg electron can be treated similar to the hydrogen atom. The excitation of the electron is stated with the principle quantum number n.
The element, used in this thesis, is the alkali-metal rubidium. Therefore, the effects of Rydberg atoms are explained with the example of rubidium atoms. The rubidium atom has one valence electron. The lowest energetic state is the $5S_{1/2}$ state, where the principle quantum number is $n = 5$ and the orbital angular quantum number of the electron is $L = 0$. The total angular quantum number, including the spin of the electron, is defined as $J = 1/2$. This is written as subscript at the end of the state description.
An excited state with a principle quantum number $n > 10$ can be called Rydberg state. Typical Rydberg states used in this thesis are the $32S_{1/2}$ state and the $40S_{1/2}$ state. In principle, Rydberg states above $n = 200$ [63] can be reached. For high Rydberg states, the electron is on a very large orbit and a small perturbation leads to the ionization of the Rydberg atom as the binding energy is small. Besides the Rydberg S states, it is also possible to excite a Rydberg P or D state. They have an orbital quantum number of $L = 1$ and $L = 2$, respectively.
The scaling laws of the important properties of Rydberg atoms are listed in table 2.1. Note, that the so called quantum defect is reducing the principle quantum number n to an effective principle quantum number n^*. This is skipped in this thesis, but can be read in the literature [62].
The large orbital radius of Rydberg atoms leads to a strong polarizability and thereby to a strong Rydberg-Rydberg interaction. As the electron wave function of a Rydberg state is larger than the electron wave function of lower states, the overlap is small, which results in a small transition dipole moment and a long lifetime of the Rydberg atom.

Table 2.1 Scaling laws of properties of Rydberg atoms: The table shows the scaling of Rydberg atom properties depending on the principle quantum number n of the Rydberg state [64].

Property	Scaling
Binding energy	n^{-2}
Orbital radius	n^2
Polarizability	n^7
Natural lifetime	n^3

2.2.1 Rydberg blockade

The weakly bound electron interacts with neighboring atoms via the dipole-dipole interaction, thereby a narrow band excitation of a second atom close to a Rydberg atom is not possible, as the Rydberg state of the second atom is shifted out of resonance. This effect is called Rydberg blockade [65–67], as a second Rydberg excitation is blocked within a certain radius, respective volume, around a Rydberg atom.
The effect of the Rydberg blockade is essential for our approach of a single-photon source, as mentioned in chapter 1. This effect will lead to the suppression of multiple, simultaneous excitations in the confined volume. The blockade radius for the $40S_{1/2}$ state is on the order of 1 µm for an excitation with a bandwidth of ≈ 400 MHz. The excitation volume is chosen to be a similar size as the blockade volume. Ideally, this would only allow one Rydberg excitation in the micro-cell, leading to the emission of antibunched photons.
As there are many atoms within the excitation volume, the Rydberg blockade is considered as a collective effect. Therefore, the Rydberg excitation is coherently shared among all atoms within the Rydberg blockade volume [24, 25].

2.3 Four-wave mixing scheme

To exploit the effect of the Rydberg blockade, a two photon excitation from the ground state to the Rydberg state and a two photon deexcitation back to the ground state is used. Therefore, it is possible to drive the atom in a closed FWM cycle.

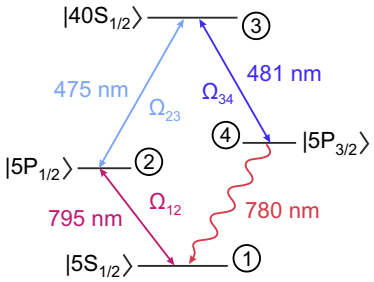

Figure 2.3 FWM scheme: The excitation scheme shows the atomic states of rubidium, involved in the FWM cycle. The excitation path is clock-wise, starting at the $5S_{1/2}$ ground state. The three coupling light fields (defined by a wavelength and Rabi frequency Ω_{ij}) transfer the population from the ground state via the $5P_{1/2}$ and the $40S_{1/2}$ into the $5P_{3/2}$ state. Then, the FWM effect leads to the emission of photons at 780 nm, closing the FWM cycle.

2.3.1 Normal FWM scheme

In a so called FWM cycle the coupling of four atomic states with three coupling light fields will lead to the emission of the fourth light field, such that the cycle is closed.
In our case, the excitation starts from the ground state via a nP_J intermediate state into a $n'S_{1/2}$ Rydberg state. The path back to the ground state goes via another $nP_{J'}$ intermediate state, such that the system can be illustrated in a diamond shape (see figure 2.3).
For rubidium, a common two photon excitation into a Rydberg state is based on the $5P_J$ intermediate states. With a near-infrared laser (795 nm) and a visible blue laser (475 nm) one can excite an atom from the $5S_{1/2}$ ground state into the $40S_{1/2}$ Rydberg state via the $5P_{1/2}$ intermediate state. By adding a third laser (481 nm), coupling the Rydberg state to the second intermediate state, namely the $5P_{3/2}$ state, the FWM cycle will be closed by the emission of photons at a wavelength of 780 nm. The FWM scheme for the $40S_{1/2}$ Rydberg state is shown in figure 2.3.
In this figure, the couplings of the atomic states are labeled with the Rabi frequencies Ω_{ij}. There, i and j are the numbers of the states, which are numbered clock-wise, starting at the ground state $5S_{1/2}$ with 1.

This FWM scheme was used in the experiment of Fabian Ripka [16, 48] and is called "normal" FWM scheme in this work.
The blue laser systems to excite into the Rydberg state in the normal FWM scheme in this experiment have the disadvantage of a low repetition rate of only 50 Hz and a large time jitter, which is on the order of the pulse duration. These disadvantages arise from complex laser systems, based on dye-amplifiers, to produce strong pulses at 475 nm and 481 nm. To circumvent these limitations, new laser systems should be used for the second generation single-photon source. Therefore, a different excitation scheme to excite rubidium Rydberg atoms has to be found.

2.3.2 Inverted FWM scheme

First of all, the Rydberg state should be a S state, which has an unperturbed Rydberg blockade, respective Rydberg pair state potential (see [48]). As a direct excitation from the ground state to the Rydberg S state is dipole forbidden, a $n\mathrm{P}_J$ intermediate state will be used. For larger n the transition energy from the intermediate to the Rydberg state becomes smaller, which means that the wavelength becomes larger. For example an intermediate state with quantum number $n = 8$, requires lasers with a wavelength of a few micrometer to reach a Rydberg state, which are not common or have not enough power, while the transition from the ground to the intermediate state requires a wavelength in the ultra-violet range, which is also not optimal.
Therefore, the best suited intermediate states are the two $6\mathrm{P}_J$ states, instead of the previous used $5\mathrm{P}_J$ states. The energy of the first transition increases, while the energy of the second transition decreases for the excitation via the $6\mathrm{P}_J$ intermediate states. The first transition is in the visible blue range (422 nm) and the second transition in the infrared range (1011 nm to $40\mathrm{S}_{1/2}$).
As the red and blue wavelength switched their role compared to the normal FWM scheme, we call the scheme with the $6\mathrm{P}_J$ intermediate states the "inverted" FWM scheme. The inverted FWM scheme for the $40\mathrm{S}_{1/2}$ Rydberg state is shown in figure 2.4.

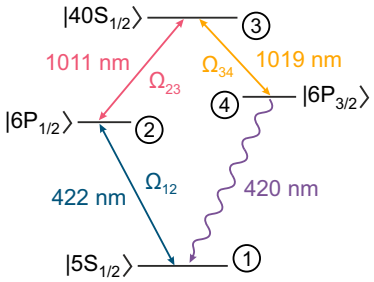

Figure 2.4 Inverted FWM scheme: The inverted FWM scheme is similar to the normal FWM scheme (see figure 2.3), where only the intermediate states are different. The excitation path is clock-wise, stating from the ground state $5S_{1/2}$. The inverted FWM cycle is closed by the emission of 420 nm photons. The transitions are defined by a wavelength and a Rabi frequency Ω_{ij}.

2.3.3 Comparison of the FWM schemes

By changing the intermediate states from $5P_J$ to $6P_J$, not only the wavelength and thereby the laser systems are changing, but also other physical properties of the FWM system are changing. To find the pro and contra of the inverted FWM scheme the two presented FWM schemes are compared.
The physical properties of the two FWM schemes are listed in table 2.2.

Table 2.2 Comparison of FWM schemes: The table shows the physical properties of the two FWM schemes for the $40S_{1/2}$ Rydberg state (the given values are rounded and taken from [68]). The subscript indices at the variables indicate the associated transition (compare with figure 2.3 and figure 2.4).

Property	normal	inverted
Wavelength of Rydberg excitation, λ_{23}	475 nm	1011 nm
Wavelength of emitted photons, λ_{41}	780 nm	420 nm
Dipole matrix element first transition, d_{12}	$2.99\,e\,a_0$	$0.24\,e\,a_0$
Dipole matrix element second transition, d_{23}	$0.012\,e\,a_0$	$0.023\,e\,a_0$

The dipole matrix elements show how strong the atomic states are coupled to each other. The normal FWM scheme has a roughly ten times larger

dipole matrix element for the first transition from the ground state to the intermediate state. Therefore, it needs a smaller electric field, respective weaker light field, to reach the same Rabi frequency according to equation 2.17.
On the other hand, the dipole matrix element of the second transition is larger for the inverted FWM scheme by roughly a factor of two. As the matrix elements, which couple to the Rydberg state, are typically small compared to the excitation into the intermediate state, this factor of two between the normal and inverted scheme is an important advantage of the inverted FWM scheme.
Also the wavelength for the Rydberg excitation is in the infrared regime for the inverted scheme, where rare-earth doped fiber laser systems can be used to generate the coupling light field. Such laser systems in the infrared regime are more powerful and easier to handle compared to high power, visible blue lasers, which are needed for the normal FWM scheme. In the experimental setup, used by Fabian Ripka, the Rydberg excitation was realized by two pulsed dye-amplified laser systems. These systems produced pulses in the blue wavelength regime with a peak power of roughly 60 W and a pulse length of ≈ 2 ns. One drawback of the pulses was the large temporal jitter of 1.5 ns, which is almost as large as the pulse duration, which leads to a complex post-selection of measured data. Another big disadvantage of the dye-amplified laser systems was the slow repetition rate of the pulses, which was only 50 Hz, compared to 100 kHz of up-to-date laser systems, and the degeneracy of the dye on a timescale of hours, leading to a decrease of the peak power. These facts have made the data acquisition for a statistical analysis tedious. Among other aspects, the disadvantages just mentioned have been the main reasons to change the excitation scheme to the inverted FWM scheme.

Chapter 3

Fiber amplifier

The decision to use the inverted FWM scheme opens the opportunity to use rare-earth doped fiber laser systems to generate the infrared laser light for the Rydberg transitions. In addition, there are also diode lasers available at the desired wavelength.
To define the requirements for the two laser systems, used for the Rydberg excitation and deexcitation, a simulation to estimate the key properties of the laser systems (see subsection 3.1.3) was done.

3.1 Simulation of the requirements

The here presented results of the simulation of the inverted FWM scheme have been investigated in the Bachelor theses of Annika Belz [34] and Benjamin Heinrich [35].
The involved atomic states are shown in figure 2.4. For the simulations the 40S Rydberg state is used. Neighboring Rydberg states will have different transition energies, respective wavelengths, and different dipole matrix elements, but for the general result of the simulation this will not change much.
By solving the time-dependent von Neuman equation in Lindblad form (see section 2.1), the time-dependent evolution of the density matrix $\rho(t)$ is obtained. This density matrix has the information of the population of each state in the diagonal entries $\rho_{ii}(t)$ and the coherence between the states in the off-diagonal entries $\rho_{ij}(t)$. The four level system is driven by the Rabi frequencies Ω_{ij}, which couple the atomic states.

3.1.1 Excitation pulses

In our experimental setup, the coupling light field is not continuously on, but it is pulsed. The pulse is represented by the power of the light, which is time-dependent $P(t)$. Therefore, the Rabi frequency is also time-dependent $\Omega_{ij}(t)$.
To perform FWM, three light pulses are propagating through the ensemble of atoms to retrieve photons on the fourth transition. This is reproduced in the simulation, where the start time, the duration, the peak power, and the shape of the three pulses can be varied to change the amount and timing of the retrieved photons. Using the amount of retrieved photons as figure of merit, the pulses can be optimized.
In principle the pulses can be arbitrary. But to gain practical results for the optimized pulses, some constrains were set for the pulse shape and duration. The pulse shape should be a Blackman-like pulse [69], where the peak value is held for an arbitrary time. The rising and falling edges of the pulses should be limited to $\approx 500\,\mathrm{ps}$ (10 % to 90 %), which corresponds to a bandwidth of $\approx 700\,\mathrm{MHz}$, in order to be able to use common electronics with a bandwidth of 4 GHz to monitor the pulses. This limits the minimal full-width at half maximum (FWHM) pulse duration to $\approx 500\,\mathrm{ps}$.
The maximized number of retrieved photons (within the experimental bounds) can be achieved with the three pulses shown in figure 3.1, labeled with the corresponding Rabi frequency Ω_{ij}.
The Gaussian beam waists for the shown simulation were determined to approximate the sizes in the experiment. Therefore, the beam waist for the first transition should be on the size of the Rydberg blockade, while the other two beams should be larger for a homogeneous overlap with the first transition beam. The beam waist for the blue pulse is $w_{12} = 0.5\,\mu\mathrm{m}$, which leads to a peak Rabi frequency of $\Omega_{12} = 2\pi \times 1340\,\mathrm{MHz}$ for the peak power of $P_{12} = 209\,\mu\mathrm{W}$. The two pulses, coupling to the Rydberg level, both have a waist of $w_{23} = w_{34} = 35\,\mu\mathrm{m}$. This results in a Rabi frequency of $\Omega_{23} = 2\pi \times 1800\,\mathrm{MHz}$ for the peak power of $P_{23} = 96\,\mathrm{W}$ and $\Omega_{34} = 2\pi \times 720\,\mathrm{MHz}$ for the peak power of $P_{34} = 17\,\mathrm{W}$. These values are the result from the optimization of the number of retrieved photons, which is shown in figure 3.2.

3.1.2 Retrieved photons

The goal of the simulation is the maximization of the number of retrieved photons, which have a wavelength of 420 nm. The number of retrieved photons can be calculated from the coherence between the final state with $i = 4$ and the ground state with $j = 1$. The coherence value is the off-diagonal element $\rho_{41}(t)$ of the density matrix. The number of retrieved photons in a time-interval from $t = 0$ to $t = t_0$ is defined as

$$N_{\mathrm{ph}}(t_0) = \frac{1}{2}\frac{\omega_{\mathrm{a},41}}{\hbar\epsilon_0 c} n^2 \left|d_{41}\right|^2 L^2 A \int_0^{t_0} \left|\rho_{41}(t)\right|^2 dt\,, \tag{3.1}$$

where $\omega_{\mathrm{a},41}$ is the angular frequency of the atomic transition, n is the atomic density, L is the thickness of the cell and A is the illuminated cross section.
The geometry is fixed to values of $L = 1\,\mu\mathrm{m}$ and $A = \pi\,(0.5\,\mu\mathrm{m})^2$. For a given steady atomic density of $n = 1.4 \times 10^{15}\,\mathrm{cm}^{-3}$ and a fixed end

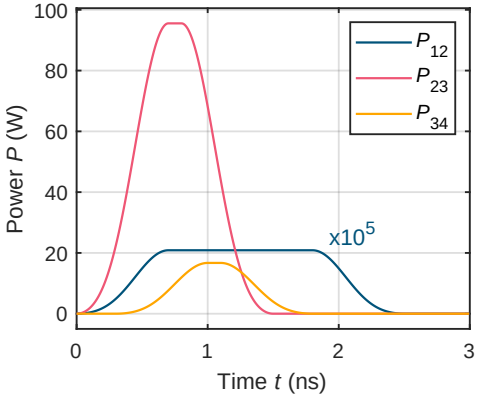

Figure 3.1 Simulated FWM pulses: These pulses are used for the time-dependent simulation of the FWM. With the displayed power and a defined Gaussian beam waist, the Rabi frequencies can be calculated (see text). The power of the first transition (blue) is multiplied by 10^5 for illustration. The first two pulses start at the same time, while the third pulse is delayed by 0.3 ns. A similar figure has already been published by the author of this thesis in [1].

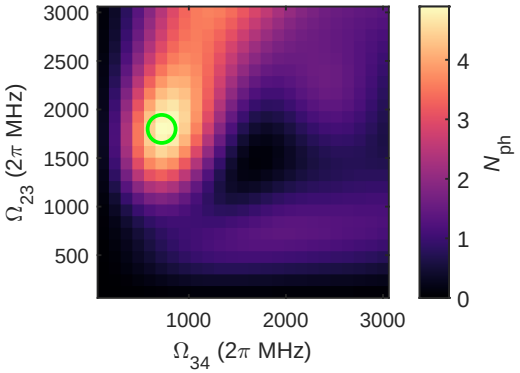

Figure 3.2 Simulated number of retrieved photons: The number of retrieved photons N_{ph}, which have a wavelength of 420 nm, depends among other things on the Rabi frequencies Ω_{23} and Ω_{34} of the two Rydberg transitions, while the Rabi frequency of Ω_{12} is constant for this plot. The maximum is marked with a green circle, which corresponds to Rabi frequencies of $\Omega_{12} = 2\pi \times 1340\,\mathrm{MHz}$ (not in the plot), $\Omega_{23} = 2\pi \times 1800\,\mathrm{MHz}$ and $\Omega_{34} = 2\pi \times 720\,\mathrm{MHz}$. As the simulation does not include the Rydberg blockade, the number of retrieved photons can exceed one, which would be ideally limited to one photon by the Rydberg blockade. A similar figure has already been published by the author of this thesis in [1].

time of $t_0 = 10\,\mathrm{ns}$ the number of retrieved photons can be maximized by maximizing the integral over the absolute coherence squared, which is the term $\int_0^{t_0} |\rho_{41}(t)|^2\, dt$.
In a first step, which is not shown here, the pulse start times and durations have been optimized. In a second step, the peak power of the three pulses is varied, to change the Rabi frequencies and thereby the populations of the states and the coherences between the states. The Rabi frequencies of the two Rydberg transitions Ω_{23} and Ω_{34} are the most important values, as there a high laser peak power is needed in order to reach those. For a fixed Rabi frequency of the first transition Ω_{12} the other two Rabi frequencies are varied to find the maximum number of retrieved photons, which is shown in figure 3.2.
The maximized number of retrieved photons exceeds one, as the nonlinearity of the Rydberg blockade effect is not included in the simulation. Ideally, the Rydberg blockade will limit the number of photons to one, as

only one Rydberg excitation is possible at the same time within a confined volume. The temporal limit of the blockade effect is the lifetime of the collective Rydberg excitation, which is called Rydberg polariton [19] and has a value of $\tau_{\text{polariton}} = 1.2\,\text{ns}$. Nevertheless, the goal of the simulation is the optimization of the FWM process and to define the requirements for the laser systems, which will be used to drive the FWM cycle.

3.1.3 Requirements for the new laser systems

From the simulation of the inverted FWM cycle and with the experiences gained from the previous experiment [48], the requirements for the laser systems can be presented. Here, the focus is on the laser systems for the Rydberg excitation, with the following key requirements (see also [1]):

- Wavelength between 1008 nm and 1024 nm (discrete values for each Rydberg state, e.g. for 32S and 40S)
- Pulse peak power $> 100\,\text{W}$
- Pulse peak power fluctuation $< 1\,\%$
- Pulse repetition frequency (PRF) from 50 Hz to 1 MHz
- Pulse duration between 0.5 ns and 10 ns
- Pulse duration jitter $< 100\,\text{ps}$
- Bandwidth-limited pulses
- Suppression of amplified spontaneous emission (ASE) $> 60\,\text{dB}$
- Stable polarization (polarization extinction ratio $> 20\,\text{dB}$)

As no commercially available laser system meets all requirements for this experiment, a custom laser system based on rare-earth doped fibers has to be built. Experts in the field of specialized fiber laser systems are a group at the Fraunhofer Institute for Applied Optics and Precision Engineering (IOF) in Jena. One of their publications on a high power fiber amplifier [70], producing continuous wave laser light at a wavelength of 1009 nm, is already in the needed wavelength range. Finally, the group

at IOF was able to design and build two ytterbium-doped fiber amplifier systems, which meet our requirements and are presented in a joint publication [1].

3.2 Laser system based on a fiber amplifier

The design of the laser systems is based on the combination of a master-oscillator with a ytterbium-doped fiber amplifier. Therefore, the frequency control is done at the continuous wave (cw) master-oscillator, which is necessary to drive the excitations at the atomic resonance frequencies. For the frequency control, common frequency stabilization techniques can be used, e.g. the Pound-Drever-Hall technique [71]. The master-oscillator is an external-cavity diode laser (ECDL) producing up to 100 mW cw output power, which is coupled into a fiber. The cw light is chopped into short pulses, which are amplified in a cascade of fiber amplifiers. A small portion of the cw light is used for frequency stabilization.

3.2.1 Components of the fiber amplifier system

As the name already indicates, all components of the amplifier are fiber-based and additionally polarization maintaining for a defined polarization throughout the amplification. The first component of the fiber amplifier is an electro-optical intensity modulator (EOIM), cutting pulses with a PRF of 3 MHz and the desired pulse shape and duration from the cw light. The reference pulse for the following characterization is an almost square pulse with a duration of 1 ns. The peak power is 100 mW after the chopping, neglecting coupling losses. These pulses have to be amplified by a gain of 1000 to reach a peak power of 100 W. Including the transmission loss from every component, the total gain of the system has to be on the order of 10^6 to compensate these losses.
The amplification of the pulses is realized in four amplification stages. After the second amplification stage, an acousto-optical modulator (AOM) is used for pulse-picking. In order to reduce the PRF by a factor of 3-30. The third amplification stage in double pass configuration is combined with a wavelength selective, fiber-based reflector, which is called fiber Bragg grating (FBG). With the FBG, only the desired wavelength is reflected back

into the amplifier system. Note, that the FBGs are designed for specific wavelengths, which are needed in our experiment. The first three amplifiers are called pre-amplifiers. After the fourth amplification stage, which is called main-amplifier, a second AOM is used for pulse-picking to an output PRF between 50 Hz and 1 MHz. A free-space spectral filter is placed behind the fiber coupler of the output.
The calculations for the design and the assembly of the fiber amplifier system were performed at the IOF in Jena. A detailed description of the fiber amplifier system can be read in the publication [1]. There, also the technical details are discussed, to synchronize the AOMs for stable pulse-picking. A schematic drawing of the components of the laser system is shown in figure 3.3.
To control the optical output of the fiber amplifier laser system, several parameters have to be set. The main parameters are the frequency of the light, the shape and duration of the electrical pulses, as well as the PRF

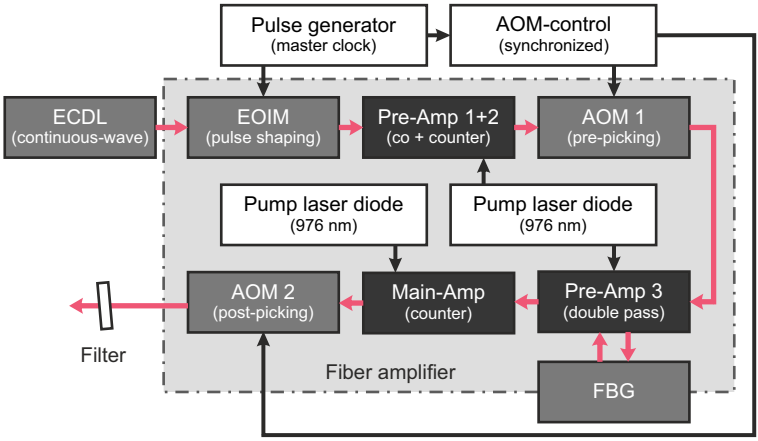

Figure 3.3 Fiber amplifier scheme: This scheme shows, how the components of the fiber amplifier are connected (ECDL: external-cavity diode laser; EOIM: electro-optical intensity modulator; AOM: acousto-optical modulator; FBG: fiber Bragg grating). The red arrows indicate the light path, while black arrows are electrical signals and the pump light. This figure is adapted from [1].

and the peak power of the optical pulses.
Our master-oscillator is an ECDL (DLpro) from Toptica, which can be monitored on a wavelength-meter, an optical cavity [49, 72] and via two photon EIT (electromagnetically induced transparency [17, 73]) spectroscopy. Therefore, the frequency of the laser can be set resonant to e.g. the transition $6P_{1/2}$ to $40S_{1/2}$ of rubidium.
Our pulse generator is a PulseStreamer from Swabian Instruments, which is able to generate square-like electrical pulses with a minimal duration of 1 ns. With this pulse generator it is not possible to generate shorter pulses, as stated in the requirements. To drive the full dynamics of the EOIM (iXblue, NIR-MX-LN-10), a voltage amplitude of 3.7 V is needed. As the pulse generator does not reach this amplitude, a radio frequency (RF) amplifier (DR-PL-10-MO) from iXblue is used to drive the EOIM. To compensate for the temperature drifts of the EOIM, an additional DC controller (MBC-DG-LAB) from iXblue is used, which stabilizes the transmission to a minimum in between pulses [74].
The PRF and the pulse peak power can be set via the controller of the fiber amplifier. There, the pulse-picking factor for AOM1 and AOM2 can be set. Additionally, the timings and the RF phase of the AOMs can be adjusted to optimize the pulse picking time-window. Depending on the PRF, the power of the pump laser diodes has to be adjusted, to maintain an output peak power of 100 W. In principle by reducing the power of the second pump laser diode, which is pumping only the main amplification stage, the output peak power can be reduced.

3.2.2 Spectral characterization

The gain-medium in a fiber amplifier is a doped fiber-core. In this case, the fiber-core is doped with ytterbium (Yb) ions to modify the absorption and emission cross sections of the glass. By plotting these cross sections over the wavelength, shown in figure 3.4, the amplification range is visible [75].
In a Yb-doped fiber, it is possible to create an inversion by pumping the fiber with light at the strongest absorption cross section around the wavelength of 975 nm. By additionally coupling a seed laser at the desired wavelength into the doped fiber, a stimulated emission at the seed wave-

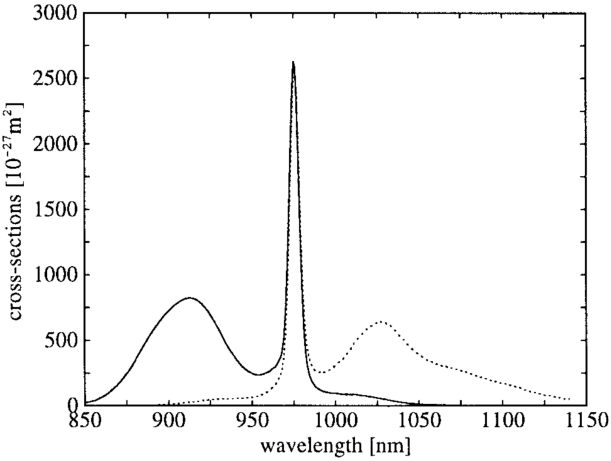

Figure 3.4 Cross sections of Yb-doped glass: The wavelength dependent absorption cross section of a Yb-doped germanosilicate glass is plotted with a solid line, while the emission cross section is plotted with a dotted line. This figure is taken from [75].

length will occur because of the high inversion. This is only possible, if the seed laser has a wavelength, where the emission cross section for a Yb-doped fiber is large. So the amplification, respective emission, range is 1000–1100 nm, which covers the required wavelength range.
The broad width of the emission range leads to the effect of amplified spontaneous emission (ASE), where the spontaneous emission of a few photons at a wavelength inside the emission range is also amplified, caused by the high inversion in the fiber-core. This ASE is hard to suppress, as the wavelength of the ASE is spectrally close to the seed wavelength. Therefore, a FBG with a spectral width of roughly 0.5 nm is integrated into the amplifier system, which reflects the seed wavelength back into the system and removes most of the ASE, as well as the pump light. Behind the output fiber of the fiber amplifier, an interference filter is placed to suppress the ASE contribution from the last amplification stage. The strongest ASE occurs at the gain maximum of the Yb-doped fiber at 1030 nm.
The AOMs in the system will lead to a temporal filtering of the light,

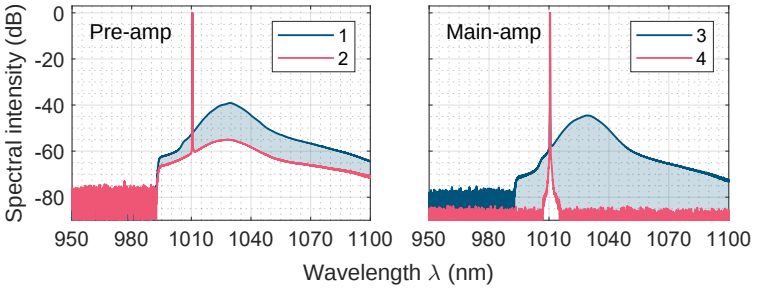

Figure 3.5 Fiber amplifier spectra: The measured spectra are normalized to see how ASE occurs and how the individual components suppress it. The spectra after the pre-amplifier stages (left) are measured without (spectrum 1) and with (spectrum 2) the FBG and AOM1. Analogous, the spectra after the main-amplifier stage (right) are measured without (spectrum 3) and with (spectrum 4) the AOM2 and interference filter. In both cases, the spectral and temporal filtering reduces the ASE significant. The final output shows an ASE suppression $> 85\,\mathrm{dB}$ at a PRF of 1 MHz. Note, that the PRF for spectrum 1 is at 3 MHz and reduced by a factor of 3 after AOM1. A similar figure has already been published by the author of this thesis in [1]. The shown data were taken by Oliver de Vries at the IOF.

besides the discussed spectral filtering. The AOMs are used to gate a time-window when the actual pulse arrives, so that the AOMs block the transmission in between two pulses with a specified suppression of $> 40\,\mathrm{dB}$. This will also reduce the power of ASE, which accumulates in between pulses.

A spectrum of the output light after the pre-amplifier stages (including stage 1 to 3) and after the main-amplifier was measured. During the assembly of the fiber amplifier it is possible to see the effect of different filter components, by taking several spectra before and after the integration of these components. The measured spectra in figure 3.5 show, how the ASE is suppressed by the different components.

From the shown measurements, an ASE suppression $> 85\,\mathrm{dB}$ at a PRF of 1 MHz is reached, by spectral and temporal filtering. Another measurement at a PRF of 1 kHz (not shown) results in an ASE suppression of $> 65\,\mathrm{dB}$, which is limited by the dynamics of the optical spectrum analyzer. This limit is caused by the low average power of 110 µW at a PRF

of 1 kHz. Overall, the required ASE suppression is reached.
It should also be mentioned, that the spectral width of the laser light is ideally Fourier-limited by the pulse shaping with the EOIM. The shown measurement has not a high enough resolution to confirm this.

3.2.3 Pulse characterization

One important part of the pulsed excitation within the FWM process is the exact control over the optical pulses and their temporal overlap. As the pulses are initially generated by an electrical pulse generator, the resulting optical pulses from the fiber amplifier are compared to the electric pulses in terms of duration and shape.
In a first step, the raw output of the pulse generator is compared with the amplified pulses after the RF amplifier. Therefore, the electrical pulses from the PULSE STREAMER are measured for pulse durations of 1 ns and 2 ns with a fast oscilloscope.
The electrical pulses are amplified by the RF amplifier from iXBLUE. The comparison of the raw and amplified pulses is shown in figure 3.6.

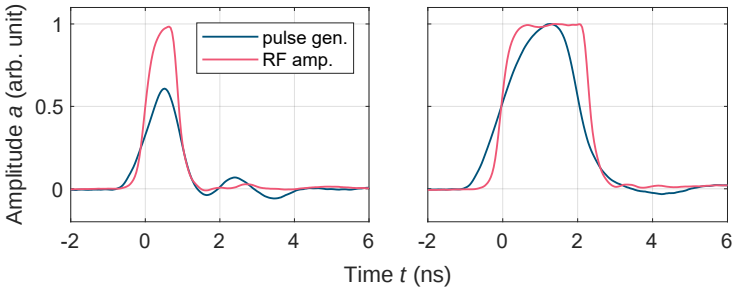

Figure 3.6 Measured pulses: The measured raw (blue) and amplified (red) electrical pulses are globally normalized to see how good they overlap. Pulses with a pulse duration of 1 ns (left) and 2 ns (right) are compared. The amplified pulses have a steeper rising and falling slope compared to the raw pulses, which originates from the nonlinear amplification of the RF amplifier. This also leads to the effect, that the amplified pulse has a duration of ≈ 2.5 ns instead of the set 2 ns. And the 1 ns amplified pulse reaches the same peak amplitude as the 2 ns pulse, even if the raw pulse has a lower peak amplitude. The shown data are averaged over 500 pulses.

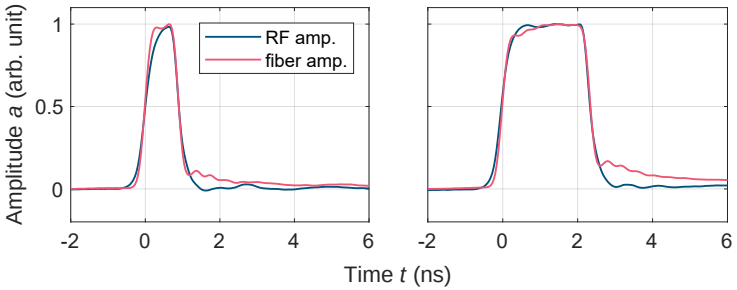

Figure 3.7 Measured pulses: The measured amplified electrical (blue) and optical (red) pulses are globally normalized to see how good they overlap. Pulses with a pulse duration of 1 ns (left) and 2 ns (right) are compared. The optical pulses overlap with the amplified electrical pulses with a good agreement. The signal distortion at the end of the rising slope and after the falling slope of the optical pulses occur from electrical ringing and charge effects in the electronics of the photodiode. The shown data are averaged over 500 pulses.

To generate pulses with an almost square shape, the used RF amplifier works well, as this electrical amplifier generates steep slopes, even if the raw pulses do not have steep slopes. Only the duration of the pulses is slightly different after the RF amplifier. On the other hand, this nonlinear response is not suited for other pulse shapes.

To further characterize the behavior of the fiber amplifier, the optical pulses are compared with the amplified electrical pulses shown in figure 3.7.

To generate the optical pulses, the amplified electrical pulses are used to modulate the transmission of the laser light with the EOIM. After passing the fiber amplifier, the optical pulses are measured on a fast photodiode (Thorlabs DET08CL/M) with a bandwidth of 5 GHz.

The shown comparison proofs, that the fiber amplifier has a high enough bandwidth, to generate optical pulses, which linearly follow the amplified electrical signal. The ringing and slowly decaying signal after the falling slope of the optical pulses is caused by electrical charges in the electronics of the photodiode. The optical signal will reach zero amplitude faster, following the amplified electrical signal, which is measurable with a single-photon counting module or a different photodiode, like in

the measurement of the pulses in [1].

3.3 Further ideas

As the fiber amplifier and the pulse shaping EOIM, both have a bandwidth of 10 GHz or higher, it will be possible to generate an arbitrary optical pulse shape with slopes below the 100 ps time scale. Therefore, a high bandwidth arbitrary waveform generator (AWG) is needed, to generate electrical pulses, which are fed into the fiber amplifier system.
As our currently used RF amplifier has a nonlinear response, a better electrical amplifier after an AWG should be implemented to generate arbitrary electrical and optical pulse shapes. This opens the opportunity to use arbitrary pulses, which are optimized during extensive simulations. In order to use a double or two-step pulse shape and to control the rising and falling slope individually. In the end, it's all about shaping the perfect optical pulses for the single-photon generation.

Chapter 4

Rydberg Rabi oscillation

The first implementation of one of the fiber amplifier systems into our experimental setup was done by Annika Belz [49]. With this, it is possible to perform the pulsed excitation of rubidium atoms to the Rydberg state, using the inverted excitation scheme. Observations of the strong atom-light coupling show the Rabi oscillations. This proves, that the system can be coherently driven faster than any dephasing.

4.1 Rabi oscillations

By driving a transition from one atomic state to another with a light field, the populations of the two states are oscillating with the Rabi frequency over time (see section 2.1). This periodic change of the population is called Rabi oscillation [18]. In a two level system, the coherence between these two energy levels is also oscillating with the Rabi frequency as a result of the oscillating population. By measuring the transmission of the driving light field, which is proportional to the imaginary part of the coherence, the Rabi oscillation will be visible on the transmission signal.
As these Rabi oscillations are a coherent effect of the system, it is difficult to ob-

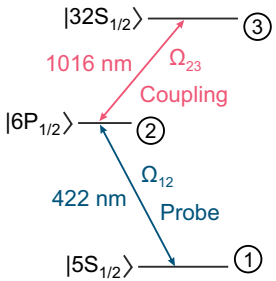

Figure 4.1 Three-level ladder scheme: In this scheme, the coupling of the intermediate and Rydberg state, caused by the "coupling" laser with Ω_{23}, is observed via the transmission of the weak "probe" laser (Ω_{12}).

serve them in a thermal vapor, where motion and collisions reduce the coherence time significantly compared to ultra-cold atoms. Therefore, the oscillations have to be fast compared to the decoherence time, driven by a strong laser light field, to observe them on a time scale below 10 ns.
In contrast to the two-level atom, now a ladder scheme with three states is considered, where the transition of the two lower states is weakly driven by a so called "probe" laser. The transition from the intermediate to the upper state is strongly driven by a so called "coupling" laser. The level scheme used in this work is shown in figure 4.1.
The coupling laser has a high Rabi frequency, such that the population oscillates between the intermediate and Rydberg state. The transmission, respective coherence, of the probe laser is influenced by this as follows:

- After the first round-trip of the population from the intermediate state to the Rydberg state and back to the intermediate state, the atom acquires a phase of π. Therefore, the initial population in the intermediate state is out of phase to the ground state transition, which leads to a refilling of the intermediate state by the probe laser, decreasing the probe transmission.

- Only after the second round-trip of the initial population via the Rydberg state, the phase accumulates to 2π. This will increase the population in the intermediate state and stops the "refill" process from the ground state, which increases the transmission of the probe to it's initial value.

The above described oscillations of the population and coherence in the three-level system can also be simulated using the theory in section 2.1. For the simulation, the probe laser light is cw with a Rabi frequency of $\Omega_{12,\,\mathrm{sim}} = 2\pi \times 25\,\mathrm{MHz}$ and the coupling laser light is a square pulse with a duration of 10 ns and a Rabi frequency of $\Omega_{23,\,\mathrm{sim},\,\mathrm{peak}} = 2\pi \times 500\,\mathrm{MHz}$. All detunings are zero and the natural decay of $\Gamma_{21} = 7.73 \times 10^6\,\mathrm{s}^{-1}$ and $\Gamma_{31} = 33.2 \times 10^3\,\mathrm{s}^{-1}$ [68] is included. The dynamics of the system is plotted in figure 4.2.
The weak probe laser light leads to a steady-state situation in the beginning. There, the Rydberg state has no population, the intermediate state has a small population ($\approx 3\,\%$) and most of the population is in the ground state ($\approx 97\,\%$). The coherences are almost zero, due to the weak

probe laser and no coupling laser. During the pulse, where the strong coupling laser is on, the populations in the intermediate $\tilde{\rho}_{22}$ and Rydberg $\tilde{\rho}_{33}$ state are oscillating back and forth. At the same time, the population in the ground state $\tilde{\rho}_{11}$ decreases, as the probe excites the atom into the less populated intermediate state. After the pulse, the populations decay into the steady-state, which happens slower than the plotted 35 ns. The lifetimes of the states are $\approx 129\,\text{ns}$ for $\tilde{\rho}_{22}$ and $\approx 30\,\mu\text{s}$ for $\tilde{\rho}_{33}$.
The coherence between the Rydberg and intermediate state $\text{Im}(\tilde{\rho}_{32})$ oscillates with the Rabi frequency Ω_{23} as expected. Finally, the oscillation of the populations, is visible in the coherence between the intermediate and ground state $\text{Im}(\tilde{\rho}_{21})$, which is proportional to the transmission of the probe laser. The transmission can be measured in the experiment and shows an oscillation with half the Rabi frequency $\Omega_{\text{osc}} \approx \frac{1}{2}\Omega_{23}$ according to the simulation.

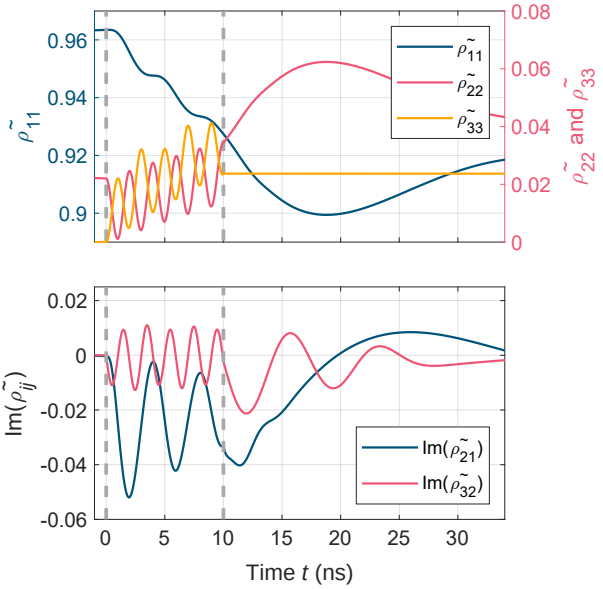

Figure 4.2 Three-level simulation: This simulation shows how the populations $\tilde{\rho}_{ii}$ (top plot) and coherences $\mathrm{Im}(\tilde{\rho}_{ij})$ (bottom plot) evolve in time. The probe laser light is cw and the coupling laser light is a square pulse, which is turned on at $t = 0\,\mathrm{ns}$ until $t = 10\,\mathrm{ns}$, shown with the vertical dashed lines. While the coupling laser light is on, some population oscillates between the intermediate state $i = 2$ and the Rydberg state $i = 3$. This oscillation causes a transfer of population from the ground state $i = 1$ into the intermediate state. Therefore, the coherence $\mathrm{Im}(\tilde{\rho}_{21})$ oscillates with half the Rabi frequency of the coupling light. After the pulse, the populations and coherences decay into the steady-state on a timescale according to the decay rates.

4.2 Experimental observation

To observe the resulting effect of Rydberg Rabi oscillations on the transmission of the probe light, a cw weak probe laser at a wavelength of 421.67 nm and one fiber amplifier system, producing strong pulses at a wavelength of 1016 nm, is used. Both lasers are overlapped in a rubidium vapor cell.

4.2.1 Experimental setup

The probe laser is an ECDL laser from TOPTICA at 421.67 nm. A few milliwatt of the probe laser is used for a reference vapor cell to set the laser frequency according to the $5S_{1/2}$ to $6P_{1/2}$ absorption spectrum.
The coupling laser, an ECDL laser at 1016 nm connected to a fiber amplifier, has a cw side-output before the light is pulsed and amplified in the fiber amplifier system. This is used to set the laser frequency. Therefore, the coupling and the probe laser are overlapped counter propagating in a 20 cm long reference cell to observe a two photon EIT [17, 73] signal. With this, the coupling laser can be tuned to excite rubidium to the 32S Rydberg state. More details, how to set the laser frequencies, can be read in [49].
For the observation of Rabi oscillations, the lasers are locked to the atomic resonances and overlapped counter propagating in a 5 mm long vapor cell filled with rubidium. The cell is placed inside an oven and is heated to 150 °C. The reservoir tube of the cell can be heated separately to a temperature of 130 °C, which determines the rubidium vapor pressure in the cell. The reservoir is also colder than the cell to prevent condensation in the cell. The probe beam is focused into the cell with a beam waist radius of $w_{\text{probe}} = 17.03(150)\,\mu\text{m}$, while the coupling laser has a beam waist radius of $w_{\text{coupling}} = 37.35(65)\,\mu\text{m}$. The coupling beam is larger than the probe laser, such that the Gaussian intensity profile of the coupling is almost homogeneous where it overlaps with the probe, because of a Rayleigh length of $z_{\text{R, coupling}} \approx 4.3\,\text{mm}$. A schematic drawing of the experimental setup is shown in figure 4.3.
The polarization of the probe beam is linear and orthogonal to the optical table. The coupling light out of the fiber is linear and adjusted with a waveplate to be the same as the probe.

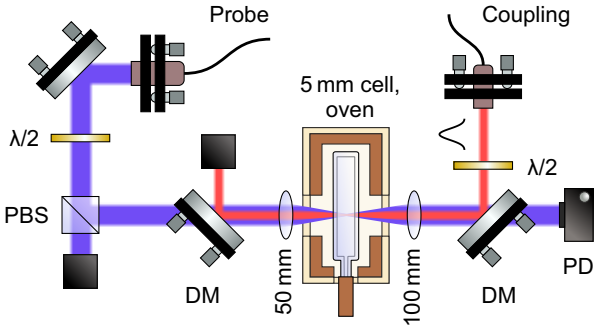

Figure 4.3 Rydberg excitation setup: The cw probe light (blue) is overlapped counter propagating with the pulsed coupling light (red) in the rubidium vapor cell. The beams are focused into the cell with a lens for each laser (probe: $f = 50\,\text{mm}$, coupling: $f = 100\,\text{mm}$). Dichroic mirrors (DM) are used to overlap and separate the two wavelength. The polarization of the beams is set via half-waveplates ($\lambda/2$) and polarization beam-splitters (PBS). The transmission of the probe is measured with a fast photodiode (PD).

To reach a large Rabi frequency for the coupling laser, the pulsed output of the fiber amplifier is used, where the pulses are generated as described in chapter 3. For this experiment, the pulses have a pulse duration of 10 ns, a peak power of 90 W, and a PRF of 100 kHz.
To measure the time-dependent transmission of the probe beam on a nanosecond timescale, an AC-coupled fast photodiode (Femto HSA-X-S-1G4-SI) is used, which has a bandwidth from 10 kHz to 1.4 GHz. The pulses are monitored at the same time on a fast photodiode (Thorlabs DET08CL/M), which is not shown in the drawing.

4.2.2 Measurement

During the experiment, the pulse shape of the coupling laser and the transmission of the probe laser is measured. The results are shown in figure 4.4.

The pulse shape is different to the pulses shown in subsection 3.2.3. The top of the pulse is not flat, but has a rising slope from 1 ns to 3 ns and a

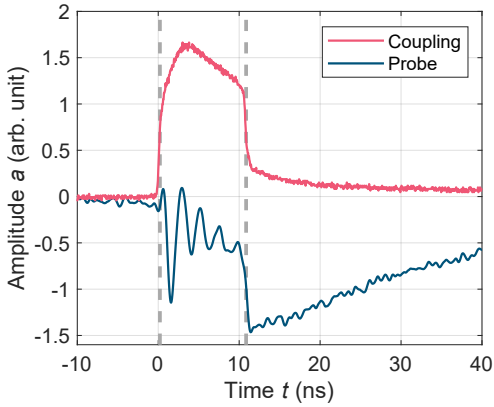

Figure 4.4 Measured Rabi oscillations: The measured coupling pulse (red) has a duration of $\approx 10.5\,\mathrm{ns}$. The pulse shape is discussed in the text. The transmission of the probe (blue) shows oscillations, which are caused by the Rabi oscillation between the intermediate and Rydberg level. The features of the transmission curve are discussed in the text. The gray dashed, vertical lines mark the beginning and the end of the pulse. The shown data is the average over 10000 pulses. This figure is adapted from [49].

falling slope from 3 ns to 10 ns. The rising slope is caused by the AOMs in the fiber amplifier, which are used to gate the pulses. After the measurement, we noticed that the times of the AOMs were not set correctly (a new measurement was not possible, as the experimental setup was already changed). Therefore, the maximum transmission through the AOMs was not reached until $t = 3\,\mathrm{ns}$, leading to the rising slope at the top of the pulse.

The falling slope is caused by a decreasing amplification in the fiber amplifier. For a 10 ns long pulse, the amount of inversion in the gain medium is decreasing after a few nanoseconds, while the pump source can not restore the full inversion. This results in a lower gain at the end of longer pulses. The tail after the coupling pulse is caused by the photodiode.

For this measurement the probe laser, which has an average power of $P_{\mathrm{probe}} = 50\,\mu\mathrm{W}$ and a beam waist radius of $w_{\mathrm{probe}} \approx 17.03\,\mu\mathrm{m}$, drives the lower transition with a Rabi frequency of $\Omega_{12,\,\mathrm{theo}} = 2\pi \times 27.34\,\mathrm{MHz}$.

The transmission of the weak probe laser shows a clear oscillation during the presence of the coupling laser pulse. These observations are similar to measurements with the $5P_{1/2}$ intermediate state [18]. The frequency of the oscillation in our measurement has a value of $\Omega_{\text{osc}} = 2\pi \times 381(95)\,\text{MHz}$, which is according to the explanation in section 4.1 approximately half of the coupling laser Rabi frequency.
Finally, the Rabi frequency of the coupling laser has a value of $\Omega_{23,\,\text{meas}} = 2\pi \times 762(190)\,\text{MHz}$. The theoretical coupling laser Rabi frequency (using equation 2.20) has a value of $\Omega_{23,\,\text{theo}} = 2\pi \times 1637.13\,\text{MHz}$, using a waist radius of $w_{\text{coupling}} \approx 37.35\,\mu\text{m}$ and a peak power of $P_{\text{coupling, peak}} \approx 90\,\text{W}$. The theoretical calculated value is higher, which can be explained by a slight misalignment of the probe and coupling laser beams in the experiment and other deviations from the theory, e.g. in the experiment, the probe laser is probing the system where the power of the coupling laser is not homogeneous.
Before the oscillations, the transmission of the probe laser has a constant steady-state value, which is not detected by the fast photodiode, as this is AC-coupled. After the coupling laser pulse, at $t \approx 10.5\,\text{ns}$, the population in the Rydberg and intermediate state is non zero and different from the initial steady-state value, where the Rydberg state was empty. Therefore, the population is decaying back into the intermediate and ground state, which is visible as a slowly vanishing signal in the probe transmission. The decay time is a combination of the lifetime of the involved states and the transient effect, as the thermal atoms leave the probe volume after a short time. The Rabi oscillations of the probe laser are too slow to be visible because of the low Rabi frequency.

4.3 Comparison to the simulation

To estimate, if the measured transmission follows the theory, the measured coupling pulse is plugged into the three-level simulation (see section 2.1) to calculate the coherence of the probe laser numerically.
The tail of the measured pulse is a measurement artifact and therefore cut for the simulation. Also the peak power, and thereby the Rabi frequency of the coupling pulse, is reduced for the simulation to gain a better agreement compared to the measurement. The peak value of the coupling laser Rabi

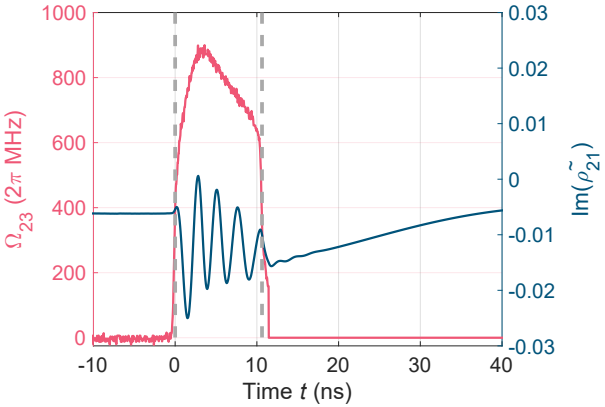

Figure 4.5 Simulated Rabi oscillations: The simulation of the three-level system shows oscillations of the probe coherence ($\mathrm{Im}(\rho\tilde{21})$, blue). The coupling Rabi frequency (Ω_{23}, red) is given by the measured pulse, while the tail at 10.5 ns is cut. Also decay and dephasing terms are included, which are dominated by the transient dephasing effect. This figure is adapted from [49].

frequency is set to $\Omega_{23,\,\mathrm{sim,\,peak}} = 2\pi \times 900\,\mathrm{MHz}$, while the average Rabi frequency during the pulse is $\Omega_{23,\,\mathrm{sim,\,avg}} = 2\pi \times 750\,\mathrm{MHz}$, which is close to the measured value. The cw probe laser has a Rabi frequency of $\Omega_{12,\,\mathrm{sim}} = 2\pi \times 15\,\mathrm{MHz}$.

The result of the simulation is shown in figure 4.5. There, the detunings are zero and the decay and dephasing terms are the following: $\Gamma_{21} = 7.73 \times 10^6\,\mathrm{s}^{-1}$, $\Gamma_{31} = 33.2 \times 10^3\,\mathrm{s}^{-1}$ and $\gamma_{ii} = 24.7 \times 10^6\,\mathrm{s}^{-1}$. The dephasing is the same for all states and given by the transient effect of the atoms flying through the probe volume. There, the dephasing is the dominant decoherence effect on a timescale of $\approx 40\,\mathrm{ns}$.

The simulated coherence of the probe laser, which is proportional to the transmission, shows a qualitative good agreement to the measurement in figure 4.4. Also minor features, like the small increase of the coherence during the rising slope of the pulse, are reproduced in the simulation. This little peak would not be there with a perfect square pulse in the simulation, shown in figure 4.2, and is only visible by plugging the real pulse shape

into the simulation. The slow decay into the steady-state value after the pulse is reproduced as well.

4.4 Conclusion

The comparison of the measurement with the simulation shows, that the fiber amplifier system works as expected and fulfills the requirements. It is not straight forward to excite and detect rubidium Rydberg atoms in thermal vapor. With the fiber amplifier system it is even possible to observe coherent dynamics in form of GHz Rabi oscillations including the Rydberg 32S state. With an optimization of the experimental setup it will be possible to reach Rabi frequencies around $2\pi \times 1800\,\mathrm{MHz}$ (for a beam with $w = 35\,\mu\mathrm{m}$ and $P = 96\,\mathrm{W}$ at 1011 nm), which are necessary to generate a high number of photons in the FWM process, according to the simulation in subsection 3.1.2.

4.5 Further ideas

Logical next steps will be the integration of both fiber amplifiers into the system to perform inverted FWM. A challenging task will be to separate the generated photons at 420.30 nm from the laser at 421.67 nm. This can be achieved by thin-film interference filters or by an etalon, where the resonance is only a few GHz wide.
Another challenging aspect of the inverted FWM is the detection of photons with a blue wavelength. There, common single-photon counting modules have only a poor detection efficiency $< 10\,\%$ (see [76]). If it becomes technically possible, superconducting single-photon detectors for the blue wavelength would be a good choice, as they have a high temporal resolution and large quantum efficiency [77].

Part II

Transient density-induced dipolar interactions in a thin vapor

Outline

This part of this thesis is about the effect of light-induced atomic desorption (LIAD). In this scheme, atoms sitting on a surface are desorbed (ejected) by a light field. In our experiment, LIAD is used to increase the density, to exploit collective effects [24, 25] during the FWM process. The pulsed desorption has the additional advantage, that the increase of the atomic density is controlled on the nanosecond timescale.
The first chapter introduces the LIAD effect. Then the pulsed LIAD setup and measurements of the LIAD effect are described. A closer look is taken at the micro-cell, since it is the central component of the experiment. In the next chapter, simulations of the LIAD effect are presented, which are based on a self-developed kinematic model. The fourth chapter deals with dipolar interactions caused by high atomic densities, which are observable in our pulsed LIAD setup on the nanosecond timescale in a thin vapor.
Central results of this part are published in [2] and have been investigated in our group by Felix Moumtsilis [78].

Chapter 5

Introduction to LIAD

5.1 General overview

The LIAD effect was first studied in the last decade of the 20th century. A. Gozzini et al. observed the "light-induced ejection of alkali atoms in polysiloxane coated cells" [28], where they increased the density of alkali atoms above the thermal equilibrium using different light sources to illuminate the cell. In the year after, M. Meucci et al. named that effect "light-induced atom desorption" [29], which is the term still used. The discovery of the LIAD effect opened the field for experiments in many different systems. There are several elements, surface materials and light sources combined to investigate the properties of the LIAD effect [28–33, 79]. A common application of LIAD is the loading of a magneto-optic trap (MOT) [37–39] using e.g. white or ultra-violet light to desorb atoms from the windows of a vacuum chamber, which can be captured in a MOT.

5.2 Atomic desorption with light

Atoms which are weakly bound to the surface can be desorbed by light. These atoms are previously adsorbed to the surface, where they are in a certain binding potential. In the case of quartz glass (SiO_2) and alkali atoms, a bound between the oxygen on the surface and the alkali atom is possible [80–82]. Other forces might also influence the bound of the adsorbed atoms (ad-atoms), e.g. the van der Waals force can lead to an attraction to the surface [83, 84].
The adsorption process should not be mixed up with the absorption pro-

cess, where particles penetrate into a material and usually have a much higher binding energy. Absorbed atoms can be ejected from the substrate e.g. by laser induced thermal desorption [85, 86]. The ad-atoms, on the other hand, can be ejected from the surface by light. Compared to thermal effects, which are sluggish, the desorption with light is instantaneous. As the bandgap energy of quartz glass ($E_g = 8.2\,\text{eV}$ [80]) and sapphire (Al_2O_3, $E_g = 6.2\,\text{eV}$ [87]) are higher than the desorption photon energy, the desorption process probably occurs at surface defects, where the binding energy is lower. Therefore, the wavelength of the desorption light and the surface properties are important parameters for the efficiency of this process.
There are different light sources used to desorb atoms. In general a white light source will work, as all visible wavelengths are present. To have a better control of the LIAD effect however, a narrowband light source can be used. These can be lasers or light-emitting diodes (LEDs). The photon energy E_{photon} of the desorbing light is anti-proportional to its wavelength λ according to the Planck-Einstein relation $E_{\text{photon}} = hc/\lambda$, where h is the Planck constant and c is the speed of light. So the desorption rate (the number of desorbed atoms per time) depends on the wavelength, respectively the energy, of the desorption light.
In an experiment with porous glass and rubidium atoms A. Burchianti et al. [88] observed, that there are two wavelength regimes, where atoms are desorbed. One regime is the resonant desorption around 780 nm and one is the off-resonant regime towards blue wavelengths. The off-resonant contribution is caused by non-thermal desorption, which is the classic LIAD process, while the resonant desorption process is based on surface-plasmon induced desorption (SPID) [89]. The two regimes are shown in figure 5.1.

The LIAD effect, represented by the blue exponential curve, shows, that for higher photon energy and respectively shorter wavelength the desorption rate increases. So ideally one would use an ultra-violet laser to desorb atoms from a glass surface. This is limited by the higher absorption of ultra-violet light in the glass, leading to damage of the glass at higher light intensities and a poor availability of such light sources. The ultra-violet light might also lead to the ionization of the desorbed atoms, which is not practical for atomic physics experiments. A wavelength in the visible blue

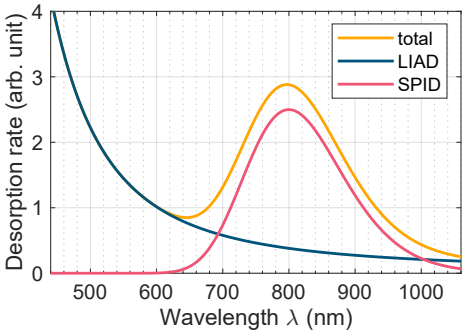

Figure 5.1 Wavelength dependent desorption: The desorption rate of rubidium atoms sitting on a porous glass surface depends on the desorption wavelength. The yellow line (labeled "total") is the sum of the resonant desorption regime (red Gaussian like curve, labeled "SPID") and the off-resonant regime (blue exponential curve, labeled "LIAD"). This figure is adapted from [88].

to green range should work well.

In our case a laser at a wavelength of 532 nm is used, which leads to a high desorption rate, while the glass can withstand a high intensity at this wavelength without damage. In addition, lasers at this wavelength are common and available in several configurations (continuous wave or pulsed, with a pulse length down to the femtosecond regime).

Chapter 6

Pulsed LIAD

In our experimental setup the LIAD effect is used in a pulsed fashion. The desorption of the atoms is not continuous, but temporarily confined by a pulse on the nanosecond timescale. This is realized by a pulsed laser at a wavelength of 532 nm and a full-width at half maximum (FWHM) pulse length of 1.1 ns. The green light is off-resonant to any atomic transition and desorbes atoms, which are adsorbed on the glass surfaces. In our case, the glass surfaces are formed by a micro-cell filled with natural rubidium (72% ^{85}Rb, 28% ^{87}Rb).
An illustration of the LIAD effect is shown in figure 6.1. The inner surface is coated with a sapphire layer. Atoms, which are flying from one cell surface to the other can be probed with a red probe laser. The desorption properties (depicted by the white arrows in figure 6.1) are discussed within the simulation of the LIAD effect in chapter 7.

6.1 Pulsed LIAD laser

Our laser is a WedgeHF 532 diode-pumped solid-state laser from Bright-Solutions. This pulsed laser at 532 nm produces pulses with a length of 1.1 ns (FWHM) a repetition rate of up to 100 kHz and a pulse energy up to 90 µJ. For this work the laser runs at a repetition rate of 50 kHz and polarization optics is used to reduce the pulse energy, respectively the peak power, to a level needed in the setup.
The laser was set up and characterized by Philipp Noack [90]. Besides the already mentioned properties, the jitter of the pulses has to be specified, both, the temporal jitter and the peak power jitter. A main limitation

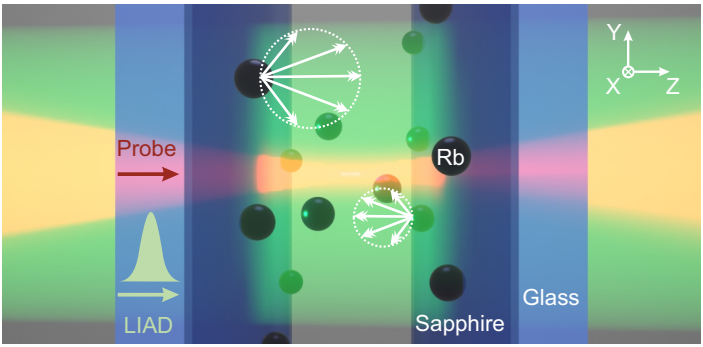

Figure 6.1 LIAD principle: The rubidium atoms are sitting on the inner surfaces of the micro-cell (glass, coated with sapphire) and can be desorbed by a short green LIAD laser pulse. After desorption, the atoms fly into the cell volume with a certain velocity (white arrows at the atoms). There, the desorbed atoms are probed with a tightly focused red probe laser. A similar figure has already been published by the author of this thesis in [2].

for the prior experimental setup, used by Fabian Ripka [48], was the large time jitter (1.5 ns) of the laser pulses. For measurements with nanosecond long pulses, the time jitter should be smaller than the pulse length for reproducible measurements. Otherwise, the pulse timing has to be monitored for every single pulse and used for post-selection of the data.
To determine the jitter, 200 consecutive pulses were measured with a fast photodiode (EOT ET-4000 GaAs). The average pulse is shown in figure 6.2. The pulse length is given as the full-width at half maximum of the 200 individual pulses averaged. At a repetition rate of 50 kHz the FWHM pulse length has a value of $t_{\mathrm{pulse}} = 1.1\,\mathrm{ns}$ with a time jitter of $t_{\mathrm{jitter}} = 0.5\,\mathrm{ns}$. The peak power jitter is proportional to the amplitude jitter measured on the photodiode. The amplitude jitter is given by the standard deviation (STD) of the amplitude at every point in time. The percentage STD is also plotted in figure 6.2 and has a value of $a_{\mathrm{jitter}} < 10\,\%$. The amount of desorbed atoms depends on the peak-power P_{peak} of the LIAD pulse, which is linear proportional to the peak-intensity I of the

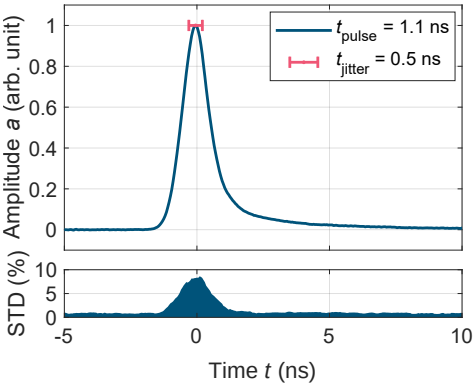

Figure 6.2 Desorption laser pulse: The average desorption pulse (average over 200 pulses) was measured with a fast photodiode. The FWHM pulse length and FWHM time jitter are listed in the legend. The amplitude jitter is given by the standard deviation (STD) and shown in the small plot below the pulse.

pulse for a fixed beam waist w_{LIAD},

$$I = \frac{P_{\mathrm{peak}}}{\pi w_{\mathrm{LIAD}}^2} \,. \tag{6.1}$$

In the further discussion of the LIAD effect, the LIAD peak-intensity is used to characterize the strength of the desorption.

6.2 The micro-cell

The micro-cell, used throughout this work, was already described in detail by Fabian Ripka [48]. Here, a summary of the important parameters of this micro-cell will be given. This micro-cell is also part of the volume confinement, which is necessary to exploit the Rydberg blockade effect in the experiment.

The micro-cell is a self-made, wedge-shaped, and sapphire-coated vapor cell. The main part of the cell are two quartz-glass plates with a height of 25 mm, a width of 50 mm and a thickness of 1.2 mm. The two glass plates are covered on one side with a 14 nm thick sapphire layer. The two

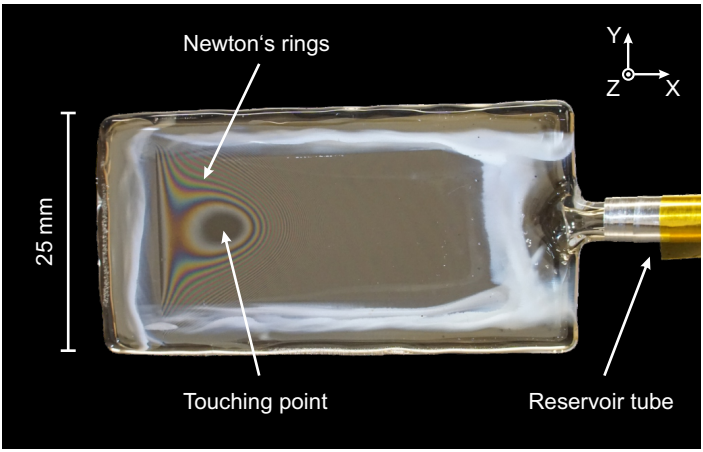

Figure 6.3 Photo of the micro-cell: The two glass plates have a touching point, visible as a dark disc. Originating from this point, one can see interference patterns, the so called Newton's rings. They indicate, that the distance between the glass plates increases in steps of $\lambda/2$. On the right side of the glass plates, there is the reservoir tube attached, which contains a macroscopic amount of rubidium metal. The photo shows true-color, while the cell is illuminated with white light. A similar figure has already been published by the author of this thesis in [2].

coated surfaces are the inner surfaces of the cell. One of the glass plates has a bevel, such that the two plates touch at the edge of the bevel. On the other end the plates have a distance of a few hundred micrometer. At this open end of the wedge, there is a glass tube (reservoir tube) attached, which contains a macroscopic amount of rubidium metal. By heating the wedge cell independent of the reservoir tube, the vapor pressure in the micro-cell can be controlled.

A photo of the micro-cell can be seen in figure 6.3, which shows interference effects in the cell. The two glass plates act as a low finesse optical resonator (optical cavity), because of the reflectivity of glass. This reflectivity is caused by different refractive indices of the glass and the vacuum in the micro-cell. Depending on the distance between the two plates, light at a certain wavelength is resonant to a "local" cavity. This "local" cavity changes its length according the the wedge-shape of the micro-cell. The

observable interference stripes or rings are so called Newton's rings [91]. There is a point of contact between the two glass plates, which is visible as a dark disc in figure 6.3. Originating from this point, the distance between the glass plates is increasing. This distance will be called "cell thickness", in the following. To determine the local cell thickness, the already mentioned interference effect is used. The interference is measured in transmission of a laser beam. Therefore, a 780 nm laser is taken, which is tuned to a frequency not resonant with a rubidium transition. The laser is focused to have a small beam waist radius of $w \approx 2\,\mu\text{m}$ in the cell. The measured transmission contains the information only about the local interference, respectively the local cell thickness.
By moving the micro-cell with respect to the laser beam, the local thickness is probed two-dimensional across the x and y axes of the micro-cell. The interference condition leads to a maximum (constructive interference), if the cell thickness L is a multiple of half the laser wavelength λ, so if

$$L = N\frac{\lambda}{2}\,, \tag{6.2}$$

where $N \in \mathbb{N}$. With a fixed laser frequency, respectively a fixed wavelength, the transmission through the wedge-shaped micro-cell is shown in figure 6.4.
The touching point and the interference rings, respectively stripes, can be observed in the transmission map, similar to the photo of the micro-cell. According to Fabian Ripka's thesis the so called "touching point" has a cell thickness $L \to 0$. He used a spectroscopic method to confirm, that the spectroscopy signal vanishes towards the touching point. So the first transmission maximum around the touching point corresponds to a cell thickness of $\lambda/2 = 390\,\text{nm}$. All consecutive maxima occur at positions where the cell thickness is $\lambda/2$ larger than the maximum before.
With this type of measurement the local cell thickness is calibrated. The cell is positioned, with respect to the probe laser, to the x and y position given by the transmission map, for a measurement of the LIAD effect at a specific cell thickness. During the measurement at one spot of the cell, the glass coating gets damaged by the strong pulses of the LIAD laser depending on the intensity and time, as mentioned in section 6.1. Consequently, the transmission through the micro-cell at this spot decreases,

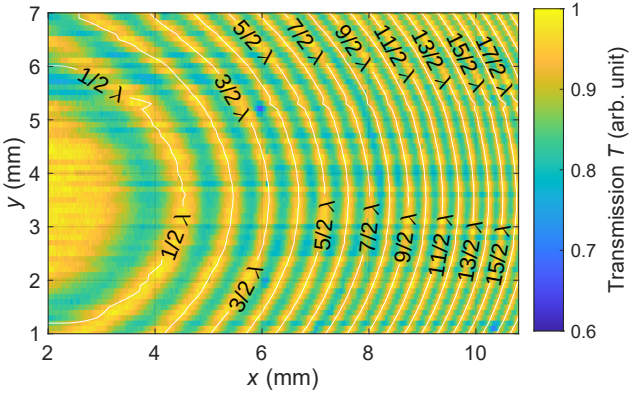

Figure 6.4 Transmission through the micro-cell: The transmission T is measured with a 780 nm laser at each point in the xy plane of the micro-cell. Due to the interference effects in the cavity, given by the two glass plates of the cell, the transmission shows maxima. These maxima are always at positions, where the cell thickness is a multiple of $\lambda/2$. The half circle was measured to be the touching point of the two glass plates, that means $L \to 0$. The first maximum around this point has a thickness of $\lambda/2$. All following maxima have a cell thickness $\lambda/2$ larger than the one before. Every second maximum is also labeled in the transmission map. At the dark-blue small regions the transmission is low because of damaged spots in the glass plates.

which is also visible as dark-blue spots in the transmission map in figure 6.4 (e.g. at $x = 6\,\text{mm}, y = 5.2\,\text{mm}$). For example, a measurement with a peak intensity of $I \approx 317\,\text{MW}\,\text{cm}^{-2}$ of the LIAD beam reduces the transmission by approximately 15 % after an exposure time of 4 h. If one spot is damaged, the cell can be moved along one interference maximum to continue measuring with the same cell thickness.

For the measurements presented in this thesis a cell thicknesses between $L = 0.78(2)\,\mu\text{m} \approx \lambda$ and $L = 6.24(7)\,\mu\text{m} \approx 8\lambda$ is used. The uncertainty of the cell thickness is calculated from the accuracy of the micrometer stage, on which the cell is mounted, and the interference transmission map. Therefore, the horizontal slices of the map are fitted with a second degree polynomial to gain a function of the cell thickness $L(x)$ depending on the stage position x. Using the x position and the accuracy of

the stage Δx, the uncertainty of the cell thickness can be calculated with $\Delta L(x) = \frac{\mathrm{d}L(x)}{\mathrm{d}x}\Delta x$.

6.3 Experimental setup

To measure the effect of LIAD a resonant, continuous wave probe laser is used to observe the transmission through the ensemble of rubidium atoms in the micro-cell. In the cell volume, there are thermal atoms, caused by the vapor pressure for a certain temperature, and there are the atoms, which are desorbed from the glass surfaces by LIAD. In a measurement all atoms are probed in the cell volume by measuring the time-dependent transmission. During the data evaluation the thermal background signal is separated from the signal caused by the desorbed atoms.
The probe laser has a wavelength of 795 nm (D_1 transition of Rb, $5S_{1/2} \rightarrow 5P_{1/2}$) or 780 nm ($D_2$ transition of Rb, $5S_{1/2} \rightarrow 5P_{3/2}$). In the experimental setup only one probe laser can be used at the time, but it is possible to switch between the probe lasers, while the rest of the setup is unaffected. The pulsed LIAD laser and the probe laser are aligned collinearly in front of the cell. The experimental setup is illustrated in figure 6.5. The probe laser has a measured Gaussian beam waist radius ($1/e^2$) of $w_{\mathrm{probe}} = 2.0(2)\,\mu\mathrm{m}$ at the center of the cell, while the LIAD laser has a waist radius of $w_{\mathrm{LIAD}} = 13.7(1)\,\mu\mathrm{m}$. The small waist of the probe laser is reached by a lens with a high numerical aperture (high-NA) NA = 0.55 and an effective focal length of $f_{\mathrm{eff}} = 3.89\,\mathrm{mm}$. The glass plates of the micro-cell are taken into account when focusing the light with the high-NA lens (Geltech, lens no. 352080). The small waist of the probe also leads to a Rayleigh length of $Z_{\mathrm{R,\ probe}} \approx 16.1\,\mu\mathrm{m}$, which is a measure for the length of the focus according to the Gaussian beam optics. As the micro-cell is inside the oven, it is not straight forward to place the cell in the focus of the probe beam. To do this, the rubidium absorption spectrum is measured while moving the cell along the optical axis of the probe beam. The intensity in the focus is the highest, which leads to a saturation of the absorption signal. By placing the cell at the weakest absorption, it will be in the focus of the probe.
For the actual measurement the intensity of the probe is on the few-photon level, to be in the weak probe regime. After the probe photons passed

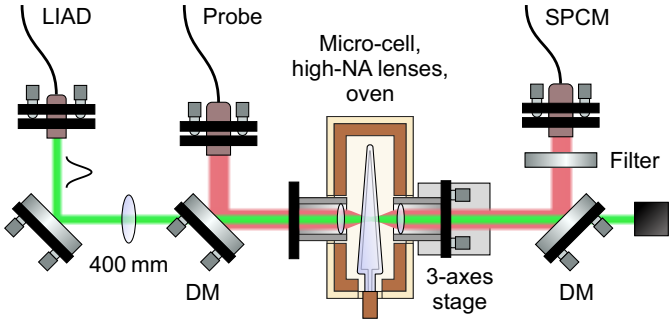

Figure 6.5 LIAD measurement setup: The pulsed LIAD beam (green) and the probe beam (red) are overlapped with a dichroic mirror (DM) infront of the micro-cell. The first high-NA lense inside the oven lead to a tight focus of the probe beam, while the LIAD beam is larger due to the additional lens with $f = 400\,\mathrm{mm}$. With the second high-NA lens on a stage, the probe light is redirected into a fiber to the single-photon counting module (SPCM). Before the SPCM, the LIAD beam is removed with a DM and filters. This figure is adapted from [48].

through the cell, they are collimated (collected) with a second high-NA lens and detected on a single-photon counting module (SPCM). The average photon count rate on the SPCM is on the order of $R_{\mathrm{probe}} = 10^6\,\mathrm{c/s}$, while the dark count rate is $R_{\mathrm{dark}} = 1.5 \times 10^3\,\mathrm{c/s}$. With the photon energy of a 780 nm photon E_{photon}, the count rate and the beam waist the intensity of the probe can be estimated to

$$I_{\mathrm{probe}} = \frac{R_{\mathrm{probe}} E_{\mathrm{photon}}}{\pi w_{\mathrm{probe}}^2} \approx 0.002\,\mathrm{mW\,cm^{-2}}\,, \tag{6.3}$$

which is well below the resonant saturation intensity of the D_2 transition $I_{\mathrm{probe}} < 0.01 I_{\mathrm{sat},D_2}$. In the optical path, there are spectral filters (e.g. a notch filter at 532 nm) and also a narrow-band etalon, with a resonance line width of $\approx 2\,\mathrm{GHz}$, before the SPCM to remove the light from the green LIAD pulse. The photons of the probe light are coupled via a multi-mode optical fiber into the SPCM. Both the optical fiber and the SPCM are placed in an opaque box to shield them from room light.
The electrical trigger from the SPCM (SPCM-AQRH-10-FC from Ex-

CELITAS) are detected with a time tagger module (TIME TAGGER 20 from SWABIAN INSTRUMENTS). This device stores the timestamps of the single-photon events with a time resolution of 34 ps. The raw timestamps can then be used to evaluate the transmission of photons. Therefore, a difference in the transmission can be observed before and after the LIAD pulse hits the cell.
The time resolution of the measurements is limited by the measured time jitter of the LIAD pulse (500 ps) and the time jitter of the single-photon counting module (350 ps), according to the data sheet. The resolution of the time tagger is neglected, as it is one order of magnitude better than the time jitter of the SPCM.

6.4 Time-resolved measurement

As our LIAD laser is pulsed on the nanosecond timescale and the desorbed atoms probably move with a fast velocity ($v \approx 200$–$300\,\mathrm{m\,s^{-1}}$), the measurement of the transmission has to be performed on that timescale, too. The elementary measurement consists of tuning the probe laser on resonance with one rubidium hyper-fine transition and detect the transmitted photons after the LIAD pulse. The evaluation of the measurements of the LIAD effect is already described by Felix Moumtsilis in [78]. A histogram of the detected photons is shown in figure 6.6. The time axis is adjusted, such that the peak of the LIAD pulse arrives at 0 ns. This is possible, since a few photons from the LIAD pulse are visible on the SPCM and can be used to set the offset of the time axis. In the measurement a small peak is still visible at 0 ns, which is higher than the background counts and originates from photons of the strong LIAD pulse.
The signal, before the LIAD pulse arrives, is used as the background signal $T_0 = \bar{T}(t < 0)$. The counts of the histogram can be converted into a transmission by dividing the signal by the average background counts. The resulting transmission signal

$$T_{\mathrm{norm}}(t) = \frac{T(t)}{T_0} \tag{6.4}$$

is shown in figure 6.7 (top), where t is the time after the LIAD pulse. The drop of the transmission direct after the LIAD pulse is clearly visible. This

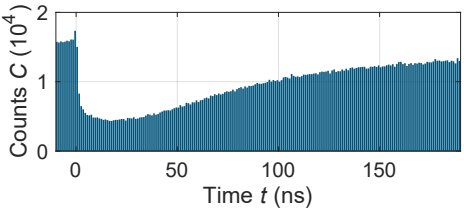

Figure 6.6 Counts during a LIAD measurement: The histogram shows how many counts were detected in a time interval after the LIAD pulse. For the plot the time bin width is set to 1 ns. After the LIAD pulse, the continuous rate of transmitted probe photons is decreased, as the desorption leads to a higher number of atoms in the cell leading to a higher absorption. The shown data are part of a 10 h measurement.

happens because of the increasing amount of atoms in the cell volume. The experimental parameters for this measurement are a cell thickness of 6.24(7) µm, a cell temperature of 160 °C and a reservoir temperature of 140 °C. The probe laser is tuned to the ^{85}Rb $F_g = 2$ transition of the D_2 line. The peak-intensity of the LIAD laser is at $I = 7.9(8)\,\mathrm{MW\,cm^{-2}}$. In general, the transmission T is connected to the optical depth OD according to the Beer-Lambert law,

$$T = e^{-\mathrm{OD}}\,. \tag{6.5}$$

For the further data analysis, only the change of the optical depth is of interest, which is caused by the desorbed atoms, leading to

$$\Delta\mathrm{OD}(t) = -\ln\left(\frac{T(t)}{T_0}\right) = -\ln\left(T_{\mathrm{norm}}(t)\right). \tag{6.6}$$

The $\Delta\mathrm{OD}(t)$ curve is shown in figure 6.7 (bottom). This measurement in a 6.24(7) µm thick cell indicates that the atoms fly in the cell for a certain time, before they leave the interaction volume of the probe beam. The velocity of the desorbed atoms is defined, among other things, by the surface binding energy of the atoms and the energy of the desorption photons. Before the next LIAD pulse hits the cell the signal from the desorbed atoms vanishes. This can be verified by decreasing the repetition rate.

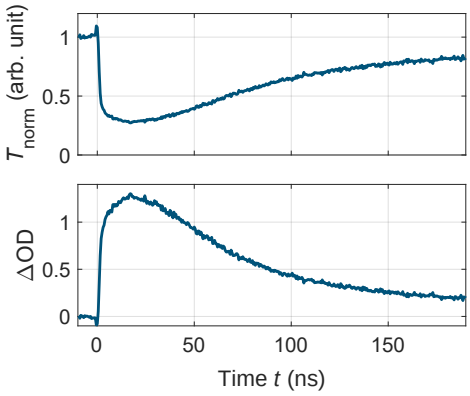

Figure 6.7 Transmission and ΔOD during a LIAD measurement: The normalized transmission T_{norm} (top) is calculated from the counts of the histogram. The peak in the transmission above 1 is caused by the strong LIAD pulse, leaking through the filters. The change of optical depth ΔOD (bottom) results from the transmission curve and shows, how the desorbed atoms contribute to the optical depth. The time bin width is 0.5 ns. The shown data are part of a 10 h measurement.

6.5 Detuning-resolved measurement

The measurement in figure 6.7 shows the response of the optical depth only for one frequency, where the probe laser is on resonance with a transition of rubidium. To gain further information about the desorption process the LIAD signal can be measured while the probe laser frequency is scanned over the full D_2 transition. This can either be done by locking the probe laser to a discrete frequency and a step wise detuning of the lock-point, or by continuously scanning the probe laser over the transition with a very slow frequency, such that the laser frequency is quasi constant on a timescale of 200 µs. We use the second approach and scan the probe laser with a frequency of 11 Hz, while the LIAD laser sends pulses with a repetition rate of 50 kHz. The advantage of this technique is the direct information about the whole spectrum after a short time, while for a locked laser all steps across the detuning have to be performed after another. On the other hand, if the frequency offset of the scanning laser is drifting after hours of measurement, the measured spectra have to be referenced

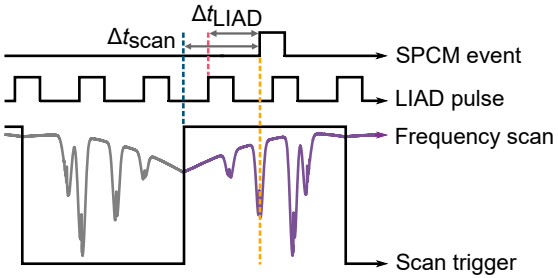

Figure 6.8 Trigger sequence during a LIAD measurement: From the detected timestamps, the time differences between the trigger events can be calculated. The time difference Δt_{LIAD} is used to set the time axis t with respect to the LIAD pulse. Δt_{scan} is converted with the use of a rubidium spectrum (purple) into a frequency axis δ, respective detuning of the probe laser. A similar figure has already been published by the author of this thesis in [2].

correctly to combine them, while the locked laser will not drift.
On the time tagger module the trigger of the SPCM, of the probe scan and of the LIAD pulse are detected. Each detected photon is set in relation to the last probe scan trigger and to the last LIAD pulse trigger. A schematic timing sequence is shown in figure 6.8.
The time difference between photon detection and the last LIAD pulse is

$$\Delta t_{\mathrm{LIAD}} = t_{\mathrm{SPCM}} - t_{\mathrm{LIAD}} \,, \tag{6.7}$$

while the difference to the last scan trigger is

$$\Delta t_{\mathrm{scan}} = t_{\mathrm{SPCM}} - t_{\mathrm{scan}} \,. \tag{6.8}$$

With the time differences, the time axis is defined as

$$t = \Delta t_{\mathrm{LIAD}} + t_{\mathrm{offset}} \,, \tag{6.9}$$

where t_{offset} is a constant time offset given by different delays between the electrical trigger from the SPCM and the electrical pulse generator. This offset can be determined for example by observing photons from the LIAD pulse on the SPCM (see section 6.4).

The frequency axis is calibrated with a rubidium spectrum. In this case, the rubidium D_2 transition is observed on a photodiode. The probe laser is scanned linearly, in first approximation, while a trigger marks each change of the scan direction. Therefore, the angular laser frequency is calculated with

$$\omega_\mathrm{l} = A\Delta t_\mathrm{scan} + \omega_\mathrm{spectrum}\,, \tag{6.10}$$

where A is the linear factor converting time to frequency and ω_spectrum is the absolute frequency of the start of the scan.
Note, that all frequencies in this part are given as angular frequencies. The probe laser detuning δ is defined as the difference between the laser frequency ω_l and the resonant atomic transition frequency ω_a with

$$\delta = \omega_\mathrm{l} - \omega_\mathrm{a}\,. \tag{6.11}$$

Analog to the evaluation in section 6.4, the histogram of the transmitted photons is used to calculate the time-dependent and now also the detuning-resolved transmission $T(t, \delta)$. The transmission matrix is shown in figure 6.9.
The background spectrum in the transmission matrix along the detuning axis for times before the LIAD pulse ($t < 0\,\mathrm{ns}$) is clearly visible. Depending on the detuning of the probe, the transmission drops for a few nanoseconds up to hundreds of nanoseconds, until the signal rises again and approaches the background. The experimental parameters are identical to the fixed frequency measurement in section 6.4.
To calculate the change of the optical depth, caused by the desorbed atoms, the background signal before the LIAD pulse $T_0(\delta)$ is used to normalize every detuning slice. With this, $\Delta\mathrm{OD}$ can be defined as

$$\Delta\mathrm{OD}(t, \delta) = -\ln\left(\frac{T(t, \delta)}{T_0(\delta)}\right). \tag{6.12}$$

The resulting time- and detuning-resolved map is shown in figure 6.10.
At the time $t = 0\,\mathrm{ns}$ the LIAD pulse hits the cell, which desorbes the atoms and increases the optical depth. There are two strong features observable, one for positive detunings and one for negative detunings. The $\Delta\mathrm{OD}$ at positive detuning, a blue-detuning with $\delta > 0$, is caused by atoms flying

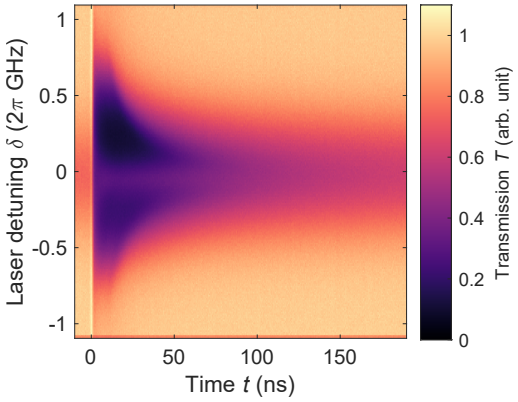

Figure 6.9 Time- and detuning-resolved transmission: The shown transmission $T(t, \delta)$ is a scan over the ^{85}Rb $F_g = 2$ transition of the D_2 line. The signal before the LIAD pulse is the background signal $T_0(\delta)$, which is caused by the atoms in the thermal vapor. The transmission is decreased after the LIAD pulse, because of the increased number of atoms in the cell volume. Detailed features of the measurement are discussed in the text. The shown data are a 10 h measurement.

in laser propagation direction, which originate from the entry facet of the micro-cell. The signal at negative detuning, a red-detuning with $\delta < 0$, corresponds to atoms flying against the laser propagation direction, which left the exit facet of the cell.

There is an asymmetry between the features of positive and negative detuning. This asymmetry shows, that more atoms from the entry facet are desorbed. This is not expected, but might occur because of an unequal heating of the two sides of the cell and because of differences in the surface properties of the two inner cell surfaces. For example, the sapphire coating can be different, the temperature in the cell oven can have a gradient between the two sides, or it might make a difference, if the LIAD laser hits the inner surface from the glass side or the vacuum side. By flipping the micro-cell by 180°, an inverted asymmetry in a measurement of the LIAD effect is observed, while the experimental parameters are identical (for more details see Appendix A). This strongly indicates, that the two sapphire coated surfaces have different properties.

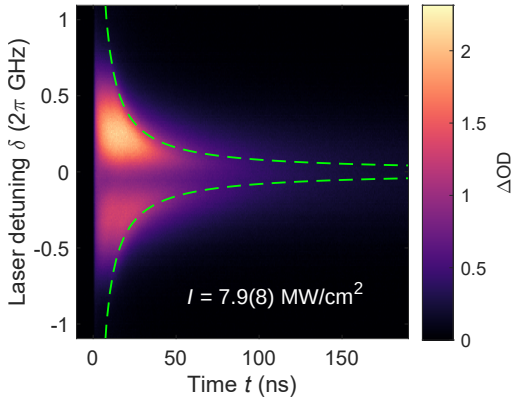

Figure 6.10 Time- and detuning-resolved ΔOD: This map results from the transmission shown in figure 6.9. The two strong features in the ΔOD map for positive and negative laser detuning correspond to atoms flying in and against the laser propagation direction. The green dashed lines show the time-of-flight curves. The stated intensity is the peak-intensity of the LIAD pulse. The shown data are a 10 h measurement. A similar figure has already been published by the author of this thesis in [2].

Besides the asymmetry, the ΔOD is weaker for detunings around zero, which is also not obvious. The spectrum along the detuning axis is a direct measurement of the z component of the velocity, as the probe laser is parallel to the z axis. So the weak signal at $\delta = 2\pi \times 0\,\mathrm{GHz}$ shows, that it is less probable to desorb atoms with a low z velocity. In other words, it is more probable to desorb atoms in forward or backward direction along the z axis, which have a z velocity larger than zero. Information about the x and y component of the velocity can not be measured with our setup, but a possible 3-dimensional velocity distribution is discussed in the kinematic model in chapter 7.

As already mentioned, the probe laser is parallel to the z axis of our system, such that the wavevector $\boldsymbol{k}$ of the probe laser only has a z component. The length of the wavevector is the wavenumber $k = |\boldsymbol{k}|$. An atom with a velocity $\boldsymbol{v}$ experiences the Doppler-effect, so the probe laser has to be detuned to hit the resonance of the moving atom. Therefore the laser

detuning required for resonant interaction is given by

$$\delta = \boldsymbol{k} \cdot \boldsymbol{v} = k v_z \,, \tag{6.13}$$

where v_z is the z component of the atom velocity. Depending on their v_z, atoms travel for a certain time, which is limited in z direction by the cell thickness L. This time is called time-of-flight TOF and depends on the laser detuning δ, respective the z velocity

$$\mathrm{TOF}(\delta) = \frac{L}{|v_z|} = \frac{Lk}{|\delta|} \,. \tag{6.14}$$

Here, the absolute values are used, to cover both atoms flying in or against the laser propagation direction, which have positive or negative v_z but identical time-of-flight. The two $\mathrm{TOF}(\delta)$ curves are drawn into figure 6.10 as dashed green lines.
In a simple model of atoms flying once through the cell, the ΔOD should vanish beyond the TOF curve, as the atoms hit the opposite cell wall. In our measurement, signal wings beyond the respective TOF curves are observed. These wings might occur because of reemissions from the surfaces, after they are hit by the arriving atoms. Additionally, broadening effects can lead to a smeared out signal. A possible origin of the wings is discussed within the kinematic model in chapter 7.

Chapter 7

LIAD model and simulation

For a better understanding of the measurements of the LIAD effect, a simple kinematic model is developed, where atoms fly through a box and interact with a probe light. This kinematic model is used in a Monte Carlo simulation to generate a time- and detuning-dependent map of the optical depth numerically.
As an overview of the following description of the simulation a program flow diagram is shown in figure 7.1. This diagram illustrates the connection of the physical and the kinematic model. The output of the simulation can be compared with a measurement to find optimized parameters for the kinematic model.

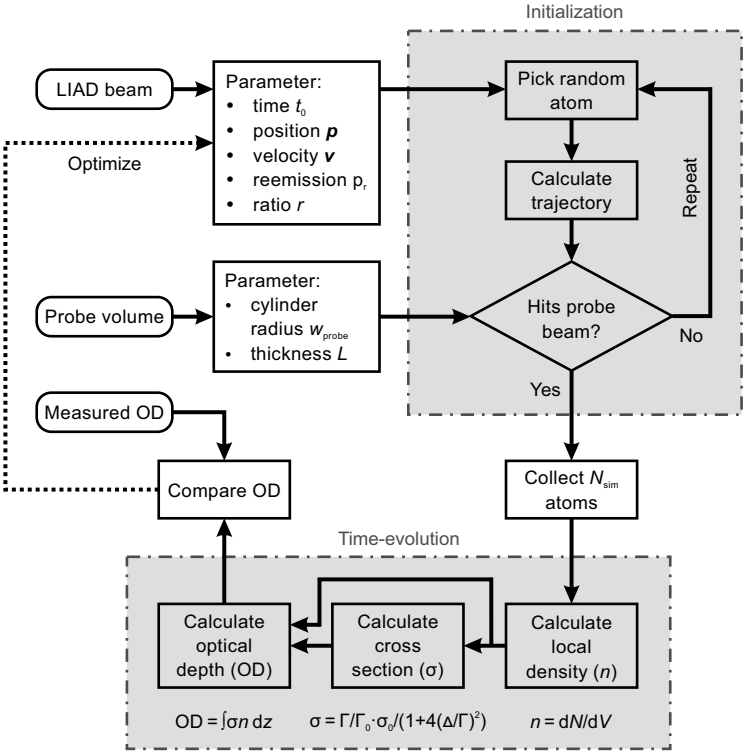

Figure 7.1 Simulation program flow diagram: This diagram shows, how the kinematic model is constructed and how the simulation is conducted. The three boxes on the left with rounded corners are the input for the simulation. According to these input information, the parameters of the kinematic model are set. The parameters are used to initialize N_{sim} atoms randomly. As the atoms move with a certain velocity, the time-evolution of the density, of the scattering cross section and finally of the optical depth is calculated. The supervised optimization is realized by closing the cycle after comparing the simulated with the measured OD. Therefore, some of the parameters can be changed during the optimization.

7.1 Physical model

In this simulation the interaction of the probe light is considered with every atom individually. The atoms do not interact with each other and in principle can fly through each other. The scattering cross section σ of every atom is calculated to implement the interaction between the atoms and the light.

7.1.1 Scattering cross section

A derivation of the scattering cross section for a two-level atom can be found in [92]. The resulting equation has the form

$$\sigma(\Delta, I_{\text{probe}}) = \frac{\sigma_0}{1 + 4(\Delta/\Gamma_0)^2 + (I_{\text{probe}}/I_{\text{sat}})}\,, \tag{7.1}$$

where σ_0 is the resonant scattering cross section, Δ is the detuning of the probe light to the atomic resonance, Γ_0 is the natural decay rate, I_{probe} is the intensity of the probe light and I_{sat} is the saturation intensity.
The resonant cross section (for $\Delta = 0$) is defined with the atomic transition frequency ω_{a} by [92]

$$\sigma_0 = \frac{\hbar\omega_{\text{a}}\Gamma_0}{2I_{\text{sat}}}\,, \tag{7.2}$$

where $\hbar$ is the reduced Planck constant. The decay rate Γ_0 is a natural constant of a certain atomic transition and describes how fast an atom in the excited energy level decays into the lower energy level. For the rubidium D_2 transition the natural decay rate has a value of $\Gamma_0 = 2\pi \times 6.07\,\text{MHz}$ [46]. The intensity I_{probe} of the probe light plays a role, if the value is on the order of the saturation intensity or above. Then the last term in the denominator of σ leads to a broadening of the cross section, which is also known as power broadening. The saturation intensity I_{sat} itself depends on natural constants, atomic properties of the transition and the probe light. Here, the saturation intensity [92] is defined as

$$I_{\text{sat}} = \frac{c\epsilon_0\Gamma_0^2\hbar^2}{4|\boldsymbol{\epsilon}\cdot\boldsymbol{d}|^2}\,, \tag{7.3}$$

where c is the speed of light, ϵ_0 is the vacuum permittivity, $\boldsymbol{\epsilon}$ is the unit polarization vector of the probe light and $\boldsymbol{d}$ is the atomic dipole moment

vector. Depending on the probe light (polarization, detuning and laser linewidth), the term $|\boldsymbol{\epsilon} \cdot \boldsymbol{d}|$ becomes a dipole matrix element d_q, with q being a quantum number to describe the reduction of the dipole matrix element to a certain quantum number.
In our case, the probe light intensity is well below the saturation intensity $I_{\mathrm{probe}} \ll I_{\mathrm{sat}}$. Therefore, the term with the intensity in the denominator of $\sigma$is neglected and equation 7.1 becomes

$$\sigma(\Delta) = \frac{\sigma_0}{1 + 4(\Delta/\Gamma_0)^2} \,. \tag{7.4}$$

The detuning Δ depends in our case on the atomic transition frequency, the laser frequency, and the velocity of the probed atom. Therefore, the atom detuning is defined as

$$\Delta_{\mathrm{atom}} = \omega_{\mathrm{a}} - \omega_{\mathrm{l}} + \boldsymbol{k} \cdot \boldsymbol{v} = -\delta + k v_z \,. \tag{7.5}$$

Additionally, a density dependent interaction effect is included, which leads among other things to a line shift of the transition and is therefore added to the detuning term. This interaction is based on the dipolar properties of the atoms, which becomes relevant in high densities where the atoms are close to each other. The so called dipole-dipole shift Δ_{dd} is discussed in detail in chapter 8. Here, this shift is just added to the detuning, which results in

$$\Delta = \Delta_{\mathrm{atom}} + \Delta_{\mathrm{dd}} \,. \tag{7.6}$$

The scattering cross section in equation 7.4 is given by a Lorentzian curve with a full-width at half maximum, set by the natural decay rate Γ_0. But as the atoms are moving through the probe volume or through a dense atomic ensemble, there are additional effects, which lead to a broadening of the scattering cross section.
To include broadening effects into the scattering cross section, one has to take care of the normalization of the integrated cross section. Therefore,

an amplitude factor A_Γ is included to correct this effect

$$A_\Gamma = \frac{\int \sigma(\Delta, \Gamma_0) \mathrm{d}\Delta}{\int \sigma(\Delta, \Gamma_0 + \Gamma_{\mathrm{add}}) \mathrm{d}\Delta} = \frac{\Gamma_0}{\Gamma_0 + \Gamma_{\mathrm{add}}}\,, \tag{7.7}$$

where Γ_{add} are the additional broadening terms. The resulting scattering cross section, which is now dependent on the total broadening $\Gamma = \Gamma_0 + \Gamma_{\mathrm{add}}$, has the form

$$\sigma(\Delta, \Gamma) = \frac{\Gamma_0}{\Gamma} \frac{\sigma_0}{1 + 4(\Delta/\Gamma)^2}\,. \tag{7.8}$$

If the scattering cross section curve is broader, the maximum will decrease while the integral of the cross section over the detuning axis stays constant. This is shown in figure 7.2 for two different total broadenings.
The total broadening is the sum of different broadening effects. A geometric effect in the broadening is the transient broadening. This effect occurs, as the atoms fly into the small probe volume and interact with the light

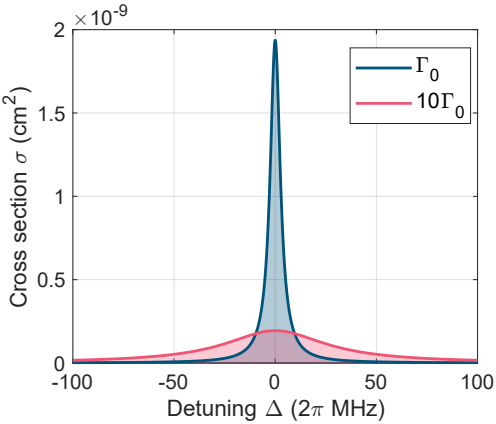

Figure 7.2 Scattering cross section curve: The cross section depends on the detuning and on the total broadening. The two curves show the cross section for different detuning values for a broadening of $\Gamma = \Gamma_0$ (blue) and $\Gamma = 10\Gamma_0$ (red). The areas under the curves have the same value for the range $\Delta = -\infty$ to $\Delta = \infty$.

only for a short time. The time, how long the atom already interacted with the light, is called transit time τ_{tt}, which is anti-proportional to the transit broadening. Therefore, a broadening term of $1/\tau_{\mathrm{tt}}$ is included in the simulation.
Analog to the line shift, there is also a density dependent broadening effect. The dipolar interactions lead to a so called self-broadening Γ_{self}, which is discussed in chapter 8. The velocity-based Doppler broadening, which is also influenced by the temperature, is already included via the atomic detuning into the calculation as $\boldsymbol{k} \cdot \boldsymbol{v}$.
The total broadening is defined as

$$\Gamma = \Gamma_0 + \frac{1}{\tau_{\mathrm{tt}}} + \Gamma_{\mathrm{self}}\,, \tag{7.9}$$

which is used in equation 7.8 to calculate the shifted and broadened scattering cross section of each atom.

7.1.2 Desorption pulse

In our experiment, and also in the simulation, the desorption process is pulsed. The pulsed laser, which is used for LIAD, is described in section 6.1. In the experimental system it is not clear whether the atoms are only desorbed during the LIAD pulse or whether there is an after-pulse effect in which atoms are still desorbed.
To tackle this, the opportunity to use different desorption pulse shapes in the simulation is taken to figure out, which shape fits best. One possible pulse shape would be a Delta function, where all atoms are desorbed at one point in time. This is not very likely in the experiment, so a pulse shape similar to the experimental measured LIAD pulse is needed. Therefore, a function called “Blackman window” is used. This pulse shape is symmetric around the peak of the function and is based on a sum of cosine functions. The wings are similar to a Gaussian distribution, but do not extend to infinity. An exemplary Blackman pulse is shown in figure 7.3 (top).
In the figure, there is a difference visible at the tail of the pulse between the ideal Blackman pulse and the measured LIAD pulse. The measured curve is above the Blackman curve at $t \approx 2\,\mathrm{ns}$. This is probably a charge

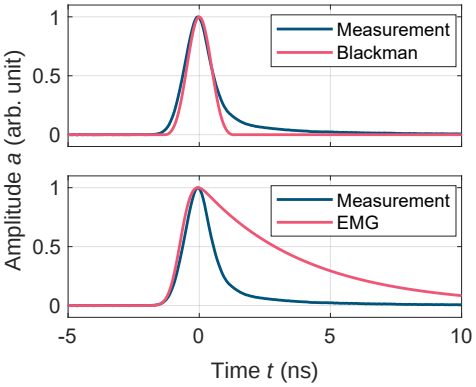

Figure 7.3 Simulation LIAD pulses: These pulse shapes are used for the simulation. The idea is to check, which pulse shape leads to the best agreement with the measurement of the LIAD pulse itself and with the ΔOD measurement. The Blackman pulse (top, red curve) is plotted with the measured LIAD pulse (blue curve). The exponential modified Gaussian (EMG) pulse (bottom, red curve) is shown together with the measured LIAD pulse (blue curve) as reference. This exponentially decaying pulse is used to answer the question, if there are after-pulse desorption effects.

effect in the fast photodiode used for the measurement of the optical LIAD pulse. So the optical pulse should look more like the simulated Blackman pulse.

For the simulation, the number of desorbed atoms per time interval is proportional to the amplitude of the desorption pulse. The total number of desorbed atoms, which is proportional to the area under the pulse, is scaled according to the peak-intensity of the LIAD pulse in the experiment.

As already mentioned, it is not clear, whether the desorption process takes place only during the LIAD laser pulse, or if there is an after-pulse effect. This after-pulse effect can occur because of thermal heating in the glass cell or because of phonon excitations. To test this in the simulation, a pulse shape with an asymmetric curve is taken. An exponential modified Gaussian (EMG) function has this features and combines a steep increase on one side with an exponential decay on the other side of the pulse.

The length of the exponential tail can be adjusted via the variables in the equation of the EMG. An exemplary pulse is shown in figure 7.3 (bottom).

7.2 Kinematic model

In our kinematic model the atoms are handled as point particles, which fly through a volume. These atoms are initially placed on the two cell walls and released with a certain velocity distribution.

7.2.1 Initial position

The start point for the simulation is the setup of the kinematic model, where all simulated atoms are adsorbed on the cell walls and no atoms are in the volume. The spatial distribution of atoms on the cell walls, with the z position $z = 0$ and $z = L$, is given by the LIAD laser. So the distribution of the atoms in the xy plane is proportional to the 2-dimensional Gaussian intensity distribution of the LIAD laser. Using this, only the atoms which are desorbed from the surface are simulated, which is the case where the LIAD beam hits the cell walls. The normal distribution along the x and y axis has a width according to the LIAD beam waist radius of $w_{\mathrm{LIAD}} = 13.7(1)\,\mu\mathrm{m}$. The number of atoms starting at $z = 0$ and $z = L$ is set by a ratio variable r. This ratio represents the asymmetry, which is observed in the measurement in figure 6.10. In figure 7.4 the initial positions of 10 representative atoms are shown.
The positions are picked randomly according to the spatial distribution. The green discs illustrate the LIAD laser. There are also atoms outside the green discs desorbed, as these discs only represent the $1/e^2$ waist of the Gaussian distribution.

7.2.2 Initial velocity

In the kinematic model, the velocity vector $\boldsymbol{v}$ for each atom is defined via spherical coordinates. The spherical coordinates are defined, that the azimutal angle ϕ is in the xy plane, with respect to the x axis, and the polar angle θ is the angle with respect to the polar axis, which is the z axis. This has the advantage, that the initial angular and the absolute velocity components can be defined with simple distributions. The two

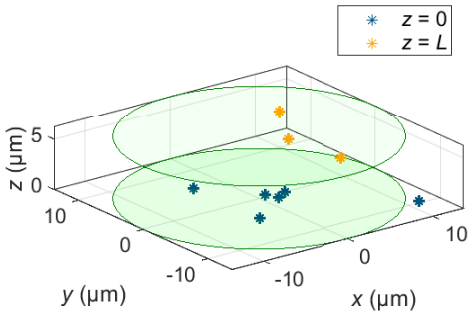

Figure 7.4 Atom start positions: The atoms (marked with a "$*$") are distributed on the two cell walls at $z = 0$ and $z = L$, where $L = 6.24\,\mu\text{m}$ is the cell thickness. Here only 10 atoms are displayed for the sake of clarity. The green discs represent the beam waist of the LIAD laser with a radius of $w_{\text{LIAD}} = 13.7\,\mu\text{m}$.

angles define the direction of the velocity vector. The absolute velocity (speed) v is the length of the velocity vector.
The distribution of the azimuthal angle is uniform, as there is no preference to emit an atom into a specific x or y direction. The polar angle is weighted with a cosine function. This $\cos(\theta)$-Knudsen law [47] is common for desorption processes, e.g. as described for molecules by G. Comsa [93]. A distribution of $\cos^m(\theta)$ is used for the polar angle, where $m \in \mathbb{N}$ is a factor to enhance the forward characteristics of the $\cos(\theta)$-Knudsen law. If not stated explicitly, m is set to $m = 1$.
The absolute velocity of the atoms is described by a distribution similar to the Maxwell-Boltzmann (MB) distribution[1]. There, the probability for an atom with $v = 0$ is zero and the maximum of the MB distribution corresponds to the most probable velocity v_{p}. Towards high velocities the probability decreases exponentially. The MB distribution function has the

[1] We are aware, that this assumption is not very precise, as the desobed atoms are far from any equilibrium, which is expected by MB.

form

$$f(v) = \frac{1}{v_\mathrm{p}^3} 4\pi v^2 e^{\left(-\frac{v^2}{v_\mathrm{p}^2}\right)}, \tag{7.10}$$

where the most probable velocity is defined as

$$v_\mathrm{p} = \sqrt{\frac{2k_\mathrm{B}T}{m}}. \tag{7.11}$$

There, k_B is the Boltzmann constant, T is the temperature, and m is the mass of the particle, which is in this case a rubidium atom.
In the kinematic model the distributions for the angle and absolute velocity are combined to one distribution, which has the equation

$$f(v, \phi, \theta) = a v^2 e^{\left(-\frac{v^2}{b^2}\right)} \cos(\theta). \tag{7.12}$$

Here, v_p and the pre-factors of the MB distribution are replaced with the variables a and b. With this variables the MB distribution can be modified. Note that the distribution $f(v, \phi, \theta)$ also assumes to depend on ϕ, but as the angle ϕ is uniform distributed, it will not change any probability.
So every atom gets initialized with a velocity according to equation 7.12. To illustrate this, a velocity vector is drawn at the atoms in figure 7.4, which is shown in figure 7.5.
Resulting from the velocity distribution, there are almost no atoms flying parallel to the surface in the xy plane, because there θ is $\pi/2$ and $\cos(\pi/2) = 0$.

7.2.3 Interaction volume

In the kinematic model an approximation of the probe beam is made by using a cylindrical beam with homogeneous intensity instead of an Gaussian beam with the transversal Gaussian intensity. This has the advantage, that the atom-light interaction is on when the atoms enter the probe cylinder and turns off immediately when the atoms leave the cylinder, which makes the calculation of the transit time simple. As the probe intensity is small compared to the saturation intensity, this approximation of the probe beam is reasonable. Another important fact is the diameter of the cylinder, which is given by two times the beam waist radius of the probe

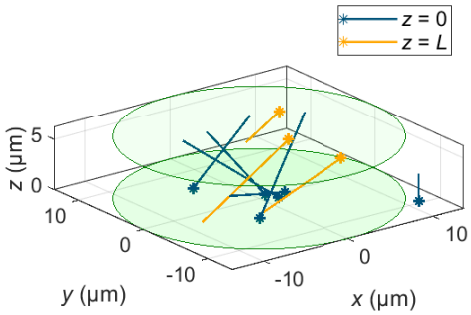

Figure 7.5 Atom start positions and velocities: The atoms (marked with a "∗") start with a velocity vector drawn as a line for each atom. The length of the lines has not the actual scale, only the direction is correct. The green circles represent the beam waist of the LIAD laser with a radius of $w_{\mathrm{LIAD}} = 13.7\,\mu\mathrm{m}$.

beam with $w_{\mathrm{probe}} = 2.0\,\mu\mathrm{m}$. The probe beam is small compared to the desorption beam, which leads to transient effects.
Atoms entering the probe beam need time to interact with the light. This time is called transit time τ_{tt} and leads to the transit time broadening effect as the scattering cross section is broadened by $1/\tau_{\mathrm{tt}}$.
The probe beam cylinder is combined with the kinematic model and shown in figure 7.6. The velocity vectors show the trajectory of the atoms. Some of them do not intersect with the probe cylinder, so they do not interact with the probe light. But in the model a reflection, respective reemission, is included at the cell walls, which leads to a change of the atom trajectory there. That is the reason why the atoms can also enter the probe cylinder after a reemission, which is not drawn in the figures.

7.2.4 Reemission

The last part of the kinematic model is the reflection, respectively the instant reemission, of an atom when it hits the opposite cell wall. This

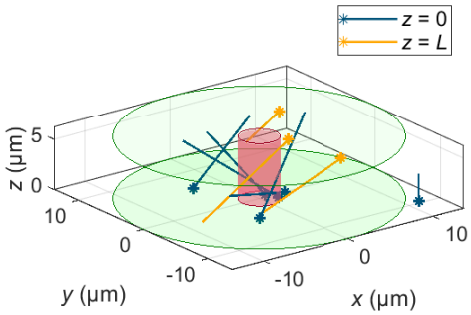

Figure 7.6 Atom start positions and velocities, with probe cylinder: The atoms (marked with a "$*$") start with a velocity vector drawn as a line for each atom. The red cylinder with a radius of $w_{\mathrm{probe}} = 2.0\,\mu\mathrm{m}$ represents the probe beam. The green circles represent the beam waist of the LIAD laser with a radius of $w_{\mathrm{LIAD}} = 13.7\,\mu\mathrm{m}$.

reflection is introduced to reproduce parts of the signal wings observed in the measurement in figure 6.10.
The reflection is implemented into the kinematic model by adding a reflection probability p_{r}. Also the maximum number of reflections is limited to N_{r} to keep the computation time of the simulation within reasonable time limits.
The reemitted atom starts where the atom previously hits the cell wall. The new velocity vector points away from the surface with a new absolute velocity according to the MB distribution. The new direction of the reflected atom is determined by uniform distributed angles ϕ and θ. So the $\cos(\theta)$-Knudsen law is not used for the reflection.

7.3 Sampling methods

The kinematic model described above is based on distributions for the initial position and velocity of the atoms. The simulation should include how an atom flies through the cell starting from every possible start position

and with every possible velocity vector (direction and absolute velocity). Therefore, the position and velocity has to be sampled to run the simulation.

7.3.1 Equidistant sampling method

It is in principle possible to divide a variable in equidistant steps and run the numerical calculation for each step. Afterwards, each step is weighted by the distribution for that variable. For this equidistant sampling a high resolution, i.e. a small step size, is needed to capture all features of the distribution function and the frame has to be large enough to cover also the wings of the distribution.
Such scan over a variable has to be done for all variables in space and velocity, which results in a huge multidimensional matrix containing all possible combinations. The advantage of this equidistant sampling method is, that all combinations are calculated and every combination is calculated only once. But it is obvious, that this method leads to very long computation times, as combinations with a low probability are also calculated with a high resolution. These combinations with low probability do not contribute so much to the resulting signal.

7.3.2 Random sampling method - Monte Carlo method

Another approach to simulate the atoms is the random sampling method. There, the steps for one variable are not equidistant, but random values according to the distribution function are picked for this variable. By doing this several times, a histogram over all random values will give the distribution function. Therefore, there are more values of a variable, where the probability according to the distribution is high and there are less values at the wings.
By picking a large number of random values for one variable at once and plugging them into the calculation, a so called Monte Carlo simulation is performed. This is done for all variables to define the position and velocity.
Also the atoms in the illustration of the kinematic model in figure 7.4, figure 7.5, and figure 7.6 are picked randomly. In the actual simulation a few thousand atoms are picked.

Exemplary random picks for $N_{\mathrm{sim}} = 100\,000$ simulated atoms are shown in figure 7.7 and figure 7.8 for the initial position and velocity, respectively. If an atom has a combination of variables, such that it never enters the probe beam cylinder, a new combination of variables is picked until the atom enters the probe beam sometime. Finally, all atoms enter the probe beam during any transit through the cell volume, at the first transit or after a reflection at the cell walls. This restriction has an influence on the position histograms on the x and y axis. A randomly picked atom, which is already inside the probe cylinder, or close to it, will more likely intersect with it. That is why the position histograms for x and y are not perfect Gaussian curves, but they have a higher probability region in the middle around zero.

7.4 Time-evolution of the simulation

Until now, the kinematic model is set up and N_{sim} atoms are randomly picked. As a next step the model evolves in time. Therefore, the time axis t is cut into discrete steps with a time step width of Δt. For very small Δt the time axis would be quasi continuous, but this would lead to a high computation time. Therefore, a time step width on the order of the time resolution in the measurements is chosen.
At the start time of the simulation, which is before the LIAD pulse, all atoms are adsorbed on the two cell walls. These atoms are released from

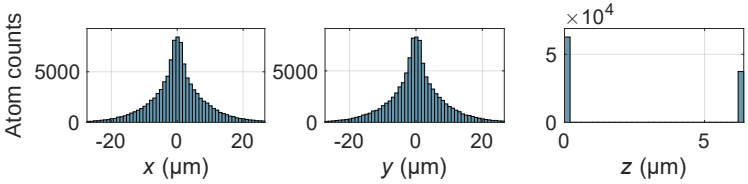

Figure 7.7 Position distribution of the atoms: The histograms show the distribution of the random picked positions for $N_{\mathrm{sim}} = 100\,000$ simulated atoms. The x (left) and y (middle) axis follow a Gaussian curve with an additionally enhanced probability around zero. The z (right) axis has only two entries at $z = 0$ and $z = L$, with the cell thickness $L = 6.24\,\mu\mathrm{m}$. The difference of atoms starting at either cell wall is given by the ratio parameter r.

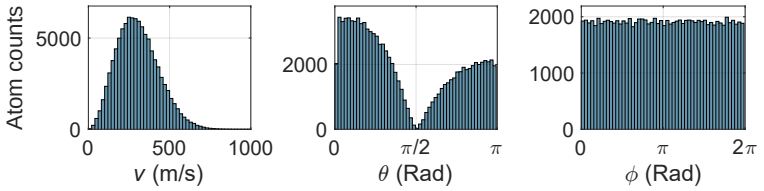

Figure 7.8 Velocity distribution of the atoms: The histograms show the distribution of the random picked velocity components in spherical coordinates for $N_{\mathrm{sim}} = 100\,000$ simulated atoms. The absolute velocity v (left) follows a modified MB distribution with a certain most probable velocity. The distribution of the polar angle θ (middle) follows the $\cos(\theta)$-Knudsen law. The height difference also occurs because of the ratio parameter r. The azimuthal angle ϕ (right) is uniformly distributed.

the cell walls according to the amplitude of the desorption pulse. So at the maximum pulse amplitude most of the atoms are released. The origin of the time axis is set to the maximum of the pulse.
After each time step the current position of all atoms is calculated. The current position is used to determine, if an atom is inside the probe beam cylinder. Only atoms, which are in the probe volume at one time step, are considered for further calculations within this time step.

7.4.1 Calculation of the local density

For the calculation of a local density, the probe cylinder is sliced into N_z slices along the z axis. For each atom in the probe volume the current z position is used to determine, in which slice this atom is. By counting all atoms in one slice and dividing by the slice volume, a density which is z-dependent is calculated. By doing this for all time steps, a time- and z-dependent local density $n_{\mathrm{sim}}(t, z)$ is gained, where the time and z axis has discrete steps for faster computation.
The density value depends linear on the number of simulated atoms N_{sim}. Within the simulation the density value is used to calculate the density-dependent dipole-dipole shift and the density-dependent self-broadening. To decouple the number of simulated atoms from the density value, an additional scaling is used. Therefore, the density value is divided by N_{sim} and multiplied with a parameter N_{density}. This parameter describes the

total number of atoms, which would be present in the kinematic model, to produce a suitable density value. The resulting density is given by

$$n(t,z) = \frac{N_{\text{density}}}{N_{\text{sim}}} n_{\text{sim}}(t,z)\,. \tag{7.13}$$

The time- and z-dependent density is plotted in figure 7.9 for several time steps.
This time- and z-dependent density can be converted to a form, where the change of the density for an atom with a certain z velocity can be seen. In other words, a conversion into the time- and detuning-dependent density is performed.
Therefore, the velocity v_z for each z and t is calculated by

$$v_{z,i,j} = \frac{z_i}{t_j}\,, \tag{7.14}$$

where i and j are all possible indices of the position and time, respectively. With equation 6.13 a detuning value from the z velocity is calculated. By mapping the z axis of $n(t,z)$ on the detuning axis δ, the time- and

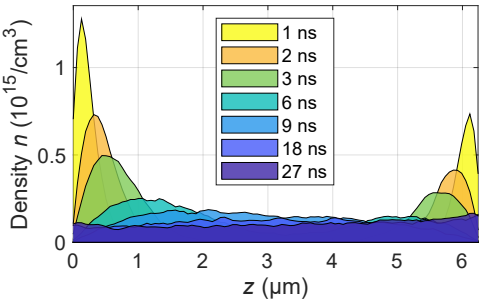

Figure 7.9 Simulated local density: The local density is calculated for $N_z = 100$ slices. During the pulse all atoms are desorbed and enter the cell volume in two thin, dense atom clouds at $t \approx 1\,\text{ns}$. These clouds expand, as the atoms have different z velocities, into the middle of the cell, while the density decreases. After a time of $t \approx 18\,\text{ns}$ is the density almost equally distributed in the cell volume. The cell thickness is $L = 6.24\,\mu\text{m}$. A similar figure has already been published by the author of this thesis in [2].

detuning-dependent density is plotted in figure 7.10.
The map shows, which density a test atom with a certain detuning, respective z velocity, will "feel" while it travels through the micro-cell from one wall to the other. The density in the cell is caused by LIAD with the characteristics discussed above (velocity distribution and desorption ratio of the atoms). For example a test atom with a detuning of $\delta = -2\pi \times 500\,\mathrm{MHz}$ is first in the atom ensemble starting at $z = L$ and $t = 0\,\mathrm{ns}$, so the local density value is high. Then, it flies through the cell and enters the opposite ensemble of atoms, which consists of slow atoms, which are still close to the cell wall at $z = 0$. There the test atom is again in a higher local density, which is visible at $t = 10\,\mathrm{ns}$ for $\delta = -2\pi \times 500\,\mathrm{MHz}$. The test atom will finally hit the other cell wall according to its TOF(δ). As this simulated local density is used in the calculation of the scattering

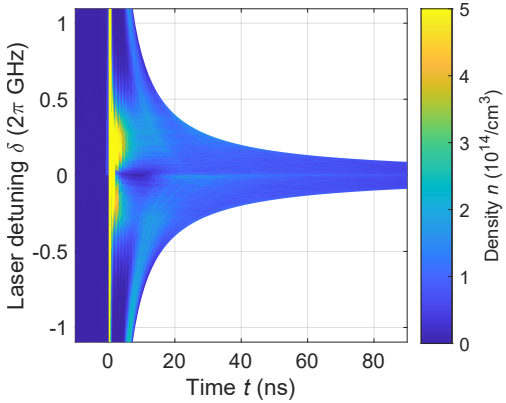

Figure 7.10 Detuning-resolved local density: The local density from figure 7.9 is mapped on a detuning axis, to see the evolution for different z velocities (detunings) of the atoms. Initially, all atoms are on the two cell walls and the density in the cell volume is zero for $t < -1\,\mathrm{ns}$. After the atoms passed the initial local high density regime direct after the desorption process, marked as yellow line around $t \approx 0.5\,\mathrm{ns}$, they enter the opposite atom ensemble according to their z velocity, which is visible as light blue stripes just before the TOF curves. After the atoms hit the other cell wall at TOF, they are gone. The upper limit of the density colorbar is manually decreased for a better visibility of the low density values. The cell thickness is $L = 6.24\,\mu\mathrm{m}$.

cross section, the signal structures observed in figure 7.10 might also occur in the final map of the numerical calculated optical depth. Especially if there are sharp edges between low and high density, these structures can be seen in the optical depth map.

7.4.2 Calculation of the optical depth

Besides the time axis there is also a detuning axis in the simulation, same as in the measured LIAD map. The detuning axis is divided into discrete steps $\Delta\delta$. So for each laser detuning δ and each atom in the probe beam, which has a certain v_z velocity, the atomic detuning Δ_{atom} can be calculated. Additionally, the transit time, which is the time since the atom entered the probe beam, can be calculated for each atom.
As all parameters for each time step and each detuning are known, the scattering cross section can be calculated for each atom using equation 7.8. According to the current position of the atom, the value of the cross section is attributed to one z-slice. By averaging over all cross sections in one slice, the time-, detuning-, and z-dependent average scattering cross section $\sigma(t, \delta, z)$ is determined.
The calculation of the optical depth is based on the Beer-Lambert law. As only the desorbed atoms are simulated and the thermal atoms are neglected, the resulting optical depth map is directly ΔOD. The given density $n(t, z)$ and the scattering cross section $\sigma(t, \delta, z)$ have to be multiplied and integrated along the propagation direction, namely the z axis. The resulting change of the optical depth is

$$\Delta\text{OD}(t, \delta) = \int_0^L \sigma(t, \delta, z) n(t, z) \mathrm{d}z \,. \tag{7.15}$$

7.5 Simulation results

The numerically calculated, time- and detuning-dependent ΔOD map is shown in figure 7.11 for a certain set of simulation parameters. This ΔOD map is based on the kinematic model (see section 7.2), which is combined with a Monte Carlo simulation (see section 7.3).
Visible features in the ΔOD map are the two atom clouds moving in and against the laser propagation direction. The asymmetry is caused by the

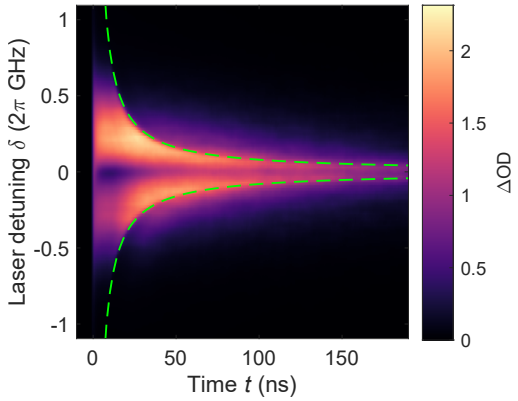

Figure 7.11 Simulated ΔOD: This time- and detuning-resolved map is a Monte Carlo simulation, based on a kinetic model. The ΔOD value show, the evolution of the desorbed atoms. The TOF is drawn with the two dashed green curves. The cell thickness is $L = 6.24\,\mu m$. A similar figure has already been published by the author of this thesis in [2].

ratio r parameter. When the atoms hit the opposite cell wall at TOF, the signal decreases. The signal wings beyond the TOF curves in the simulation are caused by the reemissions, which are included into the kinematic model. Therefore, atoms can enter the probe volume also after a reemission.

Another possible effect to produce the signal wings beyond the TOF curves could be the after-pulse effect. A simulation was run with an EMG pulse, which leads to signal wings for short times, but the wings for long times were not caused by that pulse. In the end, the Blackman pulse in combination with the reemission effect is better suited to reproduce the measurement.

In figure 7.11 the signal at zero detuning is most of the time low, caused by the directed desorption where less atoms flying perpendicular to the cell walls, which would have small v_z. Overall, there is not only a good qualitative agreement with the measurement in figure 6.10, but also a quantitative. The displayed ΔOD values are only scaled by the scaling factor N_{density} for the atomic density and show the result of an optimization of the simulation parameters (see table 7.1).

7.5.1 Simulation parameters

Within the kinematic model, there are several parameters, which can be changed to influence the simulation. Some of the simulation parameters are varied to optimize the agreement between simulation and measurement. Some parameters are set to a fixed value, to fit to the experimental setup of the measurement. For example the beam waist radii and the cell thickness are set to the values, given in the experimental setup. All parameters, and how they are used, are displayed in table 7.1.

Table 7.1 Simulation parameters: These are the parameters used in the simulation. The resulting ΔOD map is shown in figure 7.11. In the column "usage" is defined, whether a parameter is fixed, or optimized.

Parameter	Variable	Value	Usage
Atom number simulation	N_{sim}	10^5	Fixed
Cell thickness	L	6.24 µm	Fixed
Waist probe	w_{probe}	2.0 µm	Fixed
Waist LIAD	w_{LIAD}	13.7 µm	Fixed
Ratio backward/forward	r	0.6	Optimized
Desorption temperature	T_{des}	101 °C	Optimized
$\cos(\theta)$ exponent	m	1	Fixed
Pulse length LIAD	t_{LIAD}	1.1 ns	Fixed
Reflection probability	p_{r}	0.84	Optimized
Reflection counts	N_{r}	15	Fixed
Reflection temperature	T_{r}	133 °C	Optimized
z slices	N_z	100	Fixed
Atom number density	N_{density}	68 262	Optimized
Time start	t_{start}	−10 ns	Fixed
Time end	t_{end}	200 ns	Fixed
Time step	Δt	1 ns	Fixed
Detuning start	δ_{start}	−1.1 GHz	Fixed
Detuning end	δ_{end}	1.1 GHz	Fixed
Detuning step	$\Delta\delta$	20 MHz	Fixed

In the kinematic model, the distribution for the polar angle θ is weighted by the $\cos(\theta)$-Knudsen law with an additional exponent m. By changing this $\cos(\theta)$ exponent to a value $m > 1$, the forward direction is enhanced, where the atoms have a larger z velocity and the simulated ΔOD map has less contribution around zero detuning. This is not fitting to our measurement and the $\cos(\theta)$ exponent of $m = 1$ is used in this simulation.

7.5.2 Optimization

One goal of the simulation is a good reproduction of the measurement by adjusting the simulation parameters. By optimizing the parameters, the difference between the simulated and measured ΔOD is minimized. Therefore, the simulated ΔOD map is subtracted from the measured ΔOD map to gain a difference map. In this difference map a human can see, where the difference is large. But for the automated minimization of the difference, a figure of merit is needed, which can be optimized. The root-mean-square (rms) value of the difference map is chosen as our figure of merit.
The measurement, the already optimized simulation and the difference map are shown next to each other in figure 7.12. The rms value is $rms = 0.2$. This value was reached by a supervised optimization.
It is not practical to optimize all parameters at once, that is why only a few parameters were optimized in one run. The parameter set to be optimized is then changed. This human interplay with the automatic minimization of the rms value is called supervised optimization. For the

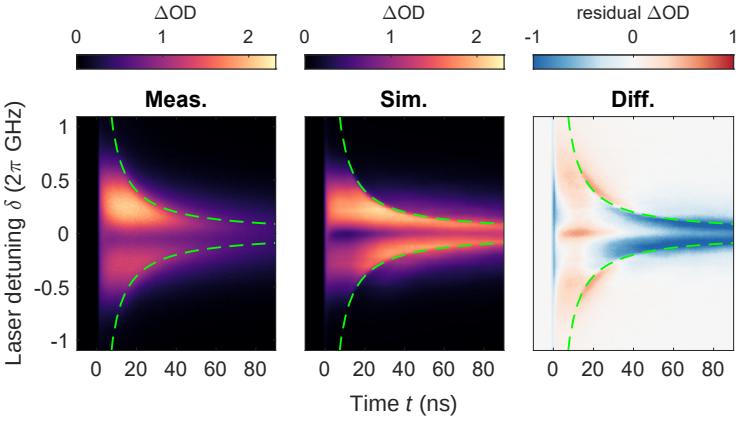

Figure 7.12 Simulated ΔOD: The measured (left) and simulated (middle) ΔOD map are in good agreement. The difference map (right) shows, where the simulation still do not fit to the measurement. The TOF is drawn with the two dashed green curves. The cell thickness is $L = 6.24\,\mu m$.

automatic optimization of several parameters the pattern search algorithm from MATLAB is taken.

Chapter 8

Dipolar interactions

Within our measurements of the LIAD effect in a thinner part of the micro-cell a broadening of the transmission spectra is observed. Following that, systematic measurements were performed to investigate the origin of the broadening effect, accompanied by a line shift of the transition. We conclude, that the observed effects originate from the dipolar interaction between the rubidium atoms in a dense atomic ensemble.

8.1 Steady-state dipolar model

The basic principle of dipolar interaction can be described in the classical limit by the model of coupled Lorentz oscillators [94]. In this model, every atom is a Lorentz oscillator and couples to the neighboring atoms via photons.
In experimental systems, strong dipolar interactions can be observed in dense media. One example are hot alkali vapors in nanometer thick cells. There, the vapor cell is heated to temperatures above 300 °C to increase the atomic density into a regime, where the atoms getting closer than the reduced wavelength $\lambda\!\!\!^{-} = \lambda/(2\pi)$. In other words $n/k^3 \gg 1$, where k is the wavevector. In this case the dipole-dipole interaction between neighboring atoms influences the transmission of probe photons through an atomic ensemble.
In these experiments the dominating broadening effect is the so called self-broadening (see subsection 8.1.3), which depends on the density and on the transition dipole matrix element squared, compared to e.g. the Doppler broadening. Besides the self-broadening, the transition is shifted in fre-

quency (see subsection 8.1.4). This occurs because the atoms are confined in a nanometer thick cell, making these experiments a 2-dimensional (2D) system, where the aligned dipoles can not arrange in the third dimension. This confinement of the dipolar interaction in a 2D system result in a red-shift (laser frequency $\delta < 0$) of the transition [26, 27].

8.1.1 Dipole matrix elements

One central physical quantity used in the dipolar model is the dipole matrix element of a transition. This value states the coupling strength between two energy levels of a transition. The coupling strength is a measure of how good the electron wavefunctions of the two energy levels overlap. If they have a similar electron wavefunction it is "easy" to excite the atom from one to the other energy level and the dipole matrix element is large. The electron wavefunction is dependent on several atomic properties, which is described with several quantum numbers. Therefore, the dipole matrix elements depend on the quantum numbers of the involved energy levels.
The definition of the dipole matrix elements follows the definition in D. Steck [92], which is similar to the definition in P. Siddons et al. [95]. Here, the ground state is labeled with the index g and the excited state with e.
In principle, there is a different transition dipole matrix element d_F for every F-state transition, which gives the strength of the coupling between two F states (the magnetic quantum numbers are neglected). There, F is the quantum number including the total orbital angular momentum of the electron with the quantum number J and the angular momentum of the nucleus with the quantum number I. The variable d_F is used to describe

$$d_F = \langle F_\mathrm{g} || \, e\boldsymbol{r} \, || F_\mathrm{e} \rangle \ , \tag{8.1}$$

where e is the charge of the particle, which is in this case an electron and $\boldsymbol{r}$ is the electron position vector in the frame of the nucleus. The double $||$ bar indicates, that d_F is already a reduced dipole matrix element, as the reduction from the magnetic m_F states was skipped.
In order to neglect the coupling between J and I, all F states are combined with their strength to one state with a J number. This reduces the system

to one reduced transition dipole matrix element d_J, which is defined as

$$d_J = \langle J_\mathrm{g} || \, e\boldsymbol{r} \, || J_\mathrm{e} \rangle \ . \tag{8.2}$$

The reduction is given as

$$\begin{aligned} \langle F_\mathrm{g} || \, e\boldsymbol{r} \, || F_\mathrm{e} \rangle = \langle J_\mathrm{g} || \, e\boldsymbol{r} \, || J_\mathrm{e} \rangle \, (-1)^{F_\mathrm{e}+J_\mathrm{g}+1+I} \\ \sqrt{(2F_\mathrm{e}+1)(2J_\mathrm{g}+1)} \begin{Bmatrix} J_\mathrm{g} & J_\mathrm{e} & 1 \\ F_\mathrm{e} & F_\mathrm{g} & I \end{Bmatrix} , \end{aligned} \tag{8.3}$$

where $\{\}$ is the Wigner 6-j symbol. A further reduction is analogous to the described reduction. Therefore, the total angular quantum number of the electron J is reduced to the orbital angular momentum L by decoupling the spin of the electron S. The reduced dipole matrix element is

$$d_L = \langle L_\mathrm{g} || \, e\boldsymbol{r} \, || L_\mathrm{e} \rangle \ , \tag{8.4}$$

which only depends on the angular momentum L. The reduction with the Wigner 6-j symbol is given as

$$\begin{aligned} \langle J_\mathrm{g} || \, e\boldsymbol{r} \, || J_\mathrm{e} \rangle = \langle L_\mathrm{g} || \, e\boldsymbol{r} \, || L_\mathrm{e} \rangle \, (-1)^{J_\mathrm{e}+L_\mathrm{g}+1+S} \\ \sqrt{(2J_\mathrm{e}+1)(2L_\mathrm{g}+1)} \begin{Bmatrix} L_\mathrm{g} & L_\mathrm{e} & 1 \\ J_\mathrm{e} & J_\mathrm{g} & S \end{Bmatrix} . \end{aligned} \tag{8.5}$$

8.1.2 Rubidium 5S to 5P transitions

The level of reduction, used to describe a system, also depends on the resolution of the probe. The two different J states of rubidium in the excited $5\mathrm{P}_J$ state can be resolved in our system. These are the D_1 and the D_2 transition of rubidium with $5\mathrm{S}_{1/2} \rightarrow 5\mathrm{P}_{1/2}$ and $5\mathrm{S}_{1/2} \rightarrow 5\mathrm{P}_{3/2}$, respectively. Therefore, the d_J reduced dipole matrix elements for the two J states are used. The literature values for the ^{85}Rb isotope are [92]

$$d_{J,D_1} = 2.9931(14)\, e\, a_0 \qquad d_{J,D_2} = 4.227\,53(62)\, e\, a_0 \, . \tag{8.6}$$

There, a_0 is the Bohr radius. For the later description of dipolar interactions, the transition dipole matrix element is used squared. So the squared

values are

$$d^2_{J,D_1} \approx 8.959\, e^2\, {a_0}^2 \qquad d^2_{J,D_2} \approx 17.872\, e^2\, {a_0}^2\,. \tag{8.7}$$

The squared dipole matrix element d_J^2 of the D_2 transition is roughly a factor of 2 larger than the squared one of the D_1 transition.
The degeneracy of the ground state $5S_{1/2}$ is $g_g = 2J_g + 1 = 2(1/2) + 1 = 2$. While for the excited state this is different for the D_1 and D_2 transition. There, the degeneracies are $g_{e,D_1} = 2$ and $g_{e,D_2} = 4$.
Another important parameter is the natural decay rate Γ_0 of the D_1 and D_2 transition of rubidium. The decay rate can be calculated from the experimental measurable natural lifetime τ_0 by

$$\Gamma_0 = \frac{1}{\tau_0}\,. \tag{8.8}$$

The lifetime can be measured for the D_1 and D_2 transition separately. From high-precision measurements [46] the natural decay rate results in

$$\Gamma_{0,D_1} = 2\pi \times 5.75\,\mathrm{MHz}\,, \qquad \Gamma_{0,D_2} = 2\pi \times 6.07\,\mathrm{MHz}\,. \tag{8.9}$$

8.1.3 Self-broadening

One result of the dipolar interactions is the self-broadening (also know as collision broadening), which originates from binary-collisions of two atoms, respective dipoles. The following derivation of the self-broadening equation is based on calculations from L. Weller [96]. There, the resonant dipole-dipole interaction is probed in the weak drive limit.
The starting point is the self-broadening parameter for alkali-metal atoms [41, 42]

$$\beta = 2fcr_0\lambda\sqrt{\frac{g_g}{g_e}}\,, \tag{8.10}$$

where f is the absorption oscillator strength for a transition, c is the speed of light, r_0 is the electron radius, λ is the transition wavelength, and g_g and g_e are the degeneracy of the ground and excited state. The absorption oscillator strength is defined as [97]

$$f = \frac{2}{3}\frac{m_e\omega_0}{\hbar e^2}d_J^2 = \frac{2}{3}\frac{m_e 2\pi c}{\hbar e^2\lambda}d_J^2\,. \tag{8.11}$$

There m_e is the electron mass, $\omega_0 = 2\pi c/\lambda$ is the transition frequency, $\hbar$ is the reduced Planck constant, e is the electron charge, and d_J is the reduced dipole matrix element for the total angular quantum number J. The electron radius is defined as

$$r_0 = \frac{1}{4\pi\epsilon_0}\frac{e^2}{m_e c^2}\,, \tag{8.12}$$

where ϵ_0 is the vacuum permittivity.
If equation 8.11 and equation 8.12 are substituted into equation 8.10, the self-broadening parameter can be written as

$$\beta = 2\frac{2}{3}\frac{m_e 2\pi c}{\hbar e^2\lambda} d_J^2 c \frac{1}{4\pi\epsilon_0}\frac{e^2}{m_e c^2}\lambda\sqrt{\frac{g_\mathrm{g}}{g_\mathrm{e}}} \tag{8.13}$$

$$= \frac{2}{3\hbar\epsilon_0} d_J^2 \sqrt{\frac{g_\mathrm{g}}{g_\mathrm{e}}}\,. \tag{8.14}$$

The degeneracy is $g_\mathrm{g} = 2J_\mathrm{g} + 1$ and $g_\mathrm{e} = 2J_\mathrm{e} + 1$ for the ground state with J_g and the excited state with J_e, respectively.
Finally, the self-broadening is given by the self-broadening parameter and the atomic density n as [42]

$$\Gamma_\mathrm{self} = \beta n = \frac{2}{3\hbar\epsilon_0} d_J^2 \sqrt{\frac{g_\mathrm{g}}{g_\mathrm{e}}} n\,. \tag{8.15}$$

The self-broadening depends on the dipole matrix element of a transition, the degeneracy of the involved states of that transition and the atomic density. For the D_1 and D_2 transition of rubidium the dipole matrix element and the degeneracy have different values. A detailed discussion about the dipole matrix elements can be read in subsection 8.1.1. The values for the D_1 and D_2 transition, used in this thesis, are stated in subsection 8.1.2.
For the self-broadening it is important to know how many sub-states are involved in a transition. This value is captured by the degeneracy of a state. If there are more sub-states in the ground state, the system can decay faster, which leads to a broader spectral line. If there are more sub-states in the excited state, the excited sub-states can exist next to each other, while they do not interact, and thereby lead to a slower decay

of the excited state.
To illustrate the broadening effect, a reference spectrum (with natural and Doppler broadening) and a second spectrum, which is broadened by the self-broadening, is plotted in figure 8.1. There, the spectrum of the D_2 transition is shown in a $L = 0.78\,\mu\text{m}$ thick cell, which has a temperature of $T_{\text{cell}} = 200\,^{\circ}\text{C}$. This temperature leads to a vapor-pressure based thermal density of $n_{\text{thermal}} = 3.8 \times 10^{14}\,\text{cm}^{-3}$ and Doppler broadened lines ($\Gamma_{\text{Doppler}} \approx 107\Gamma_0$) of the transition.
The density-dependent self-broadening leads to an additional broadening of the spectrum of $\Gamma_{\text{self}} = 68\Gamma_0$. This value of the self-broadening is reached for a density of $n_{\text{broad}} = 4 \times 10^{15}\,\text{cm}^{-3}$, which is higher than the thermal density n_{thermal}.

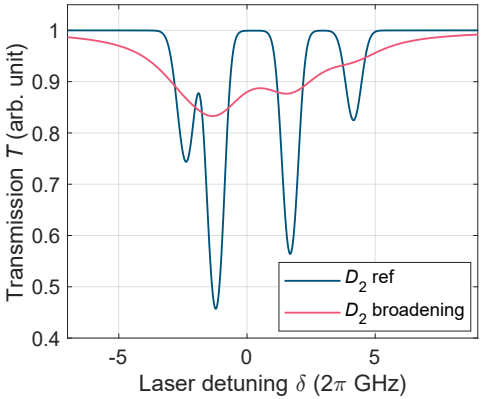

Figure 8.1 Simulated spectrum with self-broadening: The simulated transmission spectrum is calculated for a thermal rubidium vapor as function of the laser detuning. The settings for the simulated transmission are stated in the text. The reference spectrum (blue) is compared to a broadened spectrum with a self-broadening of $\Gamma_{\text{self}} = 68\Gamma_0$ (red). The zero position of the detuning axis is set to the weighted line-center of the reference D_2 transition spectrum. Note, that the artificially broadened spectrum (red) should only illustrate its influence on the spectrum. The spectra are calculated with ElecSus [98].

8.1.4 Dipole-dipole shift

The dipole-dipole shift, discussed in this thesis, covers dipolar interactions of atoms in a quasi 2-dimensional system, where the thickness of the atom ensemble is small compared to the other two dimensions. The atoms are weakly driven, so the number of atoms being in the ground state is high. This type of dipolar interaction, in a so called slab of atoms of thickness L, is described by R. Friedberg et al. [44] (see also [26]) with the equation

$$\Delta_{\mathrm{dd}} = -\left|\Delta_{\mathrm{LL}}\right| + \frac{3}{4}\left|\Delta_{\mathrm{LL}}\right|\left(1 - \frac{\sin 2kL}{2kL}\right) . \tag{8.16}$$

There the dipole-dipole shift Δ_{dd} depends on the Lorentz-Lorenz shift Δ_{LL} and on the thickness L of the atom ensemble (atom slab). The second, thickness-dependent part is a cavity-induced correction term, which is also known as the collective Lamb shift [43, 44].
In an ideal 2D system, where $L = 0$, the dipole-dipole shift Δ_{dd} converges to the Lorentz-Lorenz shift Δ_{LL}. The atoms are confined in 2D where two neighboring dipoles can be arranged side-by-side with parallel orientation of the dipoles or head-to-tail on top of each other. The head-to-tail configuration leads to an attractive force of the two dipoles, while the side-by-side orientation is repulsive. Also, the attractive force is two times stronger than the repulsive force. As in a 2D system, there is the third dimension missing, which is a side-by-side orientation, an attractive force will occur in total. This results, because one head-to-tail and one side-by-side orientation remains. Therefore, the energy of an atomic transition is changed.
For atoms in a high density, i.e. small inter-atomic distance, the transition energy is lower considering dipolar interactions in 2D. This leads to a red-shift of the resonance ($\delta < 0$), because it needs less energy to excite them, as the atoms already gained energy in the dipolar field of the neighboring atoms.
The shift in an ideal 2D system is covered by the Lorentz-Lorenz shift, which is depending on the density n and on the transition dipole matrix element d_J squared. By transferring the original equation by H.A. Lorentz

into our formalism, the Lorentz-Lorenz shift is defined as follows [26, 44]

$$\Delta_{\mathrm{LL}} = -\frac{1}{3\hbar\epsilon_0} d_j^2 n \,. \tag{8.17}$$

The transition dipole matrix element is reduced to the quantum number J, for further details read subsection 8.1.1.
The above mentioned collective Lamb shift leads to a reduction of the dipolar shift when the atom ensemble has a finite thickness (but still close to 2D). The edges of this ensemble lead to a change of the refractive index, which in turn lead to a reflection of light at the edges. This results in a cavity effect where destructive interference occurs [26]. For example, an atom ensemble with a thickness of one wavelength ($L = \lambda$) will only experience a dipole-dipole shift of $\Delta_{\mathrm{dd}} = -1/4|\Delta_{\mathrm{LL}}|$.
To illustrate the shift effect, a reference spectrum without shift and a second shifted spectrum is plotted in figure 8.2. There, the spectrum of the D_2 transition is shown in a $L = 0.78\,\mu\mathrm{m}$ thick cell, with a temperature of $T_{\mathrm{cell}} = 200\,^{\circ}\mathrm{C}$. This temperature leads to a vapor-pressure based thermal density of $n_{\mathrm{thermal}} = 3.8 \times 10^{14}\,\mathrm{cm}^{-3}$ and Doppler broadened lines of the transition.
The dipole-dipole shifted spectrum in a 2D slab has a shift of $\Delta_{\mathrm{dd}} = -12\Gamma_0$. This shift is caused by a density of $n_{\mathrm{shift}} = 4 \times 10^{15}\,\mathrm{cm}^{-3}$ and calculated with equation 8.16. In a real experiment the self-broadening (see figure 8.1) will always occur together with the dipole-dipole shift, leading to a broadened and shifted spectrum.

8.2 Evaluation of the measurements

From section 6.5 it is known, that the optical depth can be increased by LIAD. A high optical depth means, that the density is high in the cell volume. By reaching high density values, where the dipolar interaction becomes dominant, the effects discussed in section 8.1 are observable.
To reach the high density regime, defined as $n/k^3 \gg 1$, the intensity of the LIAD pulse is increased. For increasing LIAD intensity two limitations arise. One limitation is the damage of the micro-cell. For to high LIAD laser pulse intensities the glass or the sapphire coating is getting brown. The physical-chemical effect of the cell getting brown is not clear, but it

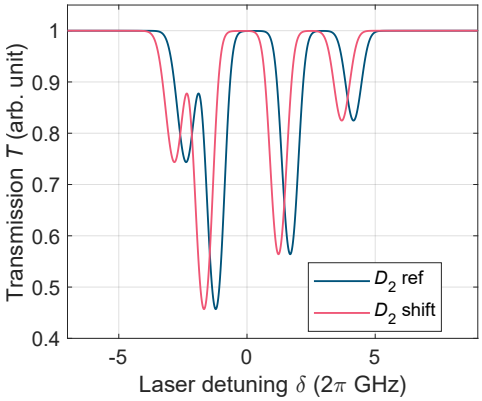

Figure 8.2 Simulated spectrum with dipole-dipole shift: The simulated transmission spectrum is calculated for a thermal rubidium vapor as function of the laser detuning. The settings for the simulated transmission are stated in the text. The reference spectrum (blue) is compared to a shifted spectrum with a dipole-dipole shift of $\Delta_{\mathrm{dd}} = -12\Gamma_0$ (red). The zero position of the detuning axis is set to the weighted line-center of the reference D_2 transition spectrum. Note, that the artificially shifted spectrum (red) should only illustrate its influence on the spectrum. The spectra are calculated with ElecSus [98].

might be a reaction of rubidium with the glass, where rubidium atoms are implanted into the glass. Nevertheless, the spot, where the cell is getting brown, has less transmission of the LIAD and probe light. Therefore, the measurement spot is changed after the transmission dropped to a certain value ($\approx 90\,\%$).

The second limitation is the detection limit of the SPCM. For high optical depths, almost zero photons are measured in transmission on an atomic resonance. On the other hand, the SPCM has a certain count rate of events, even if there are no photons present. This so called dark count rate R_{dark} is specified in the datasheet for the SPCM and also measured in a reference measurement without light to be $R_{\mathrm{dark}} \approx 1.5 \times 10^3\,\mathrm{c/s}$. As the average count rate is $R_{\mathrm{avg}} \approx 1 \times 10^6\,\mathrm{c/s}$ during the measurements, a peak value of the optical depth of $\mathrm{OD}_{\mathrm{peak}} = -\ln(R_{\mathrm{dark}}/R_{\mathrm{avg}}) \approx 6.5$ can be detected. Higher values for the OD can not be detected, as one would detect less photons then the dark count rate, which is not possible.

Alternatively, the measurement could be performed with a higher average photon count rate. This is not possible, as the rate is already at the limit of the SPCM, and otherwise photons would be missed, which occur as double photons.

8.2.1 Measurements in a thin cell

To have a quasi 2D system and to omit the detection limit, measurements are performed in a thinner part of the cell where the cell thickness is $L = 0.78(2)\,\mu\text{m}$. Additionally, in a quasi 2D system the discussed dipole-dipole shift theory from subsection 8.1.4 can be applied.
With the small cell thickness a regime is reached, where the z length of the probe volume is small compared to the x and y length. This also leads to a small background OD, which depends on the local cell thickness L. Therefore, the optical depth caused by the desorption pulse can be increased further, before the detection limit is reached.
The measurement in the thinner part of the cell is performed similar to the measurement described in section 6.5. The time- and detuning-resolved transmission is measured, which is transferred into a $\Delta\text{OD}(t, \delta)$ map. The experimental parameters for the measurements are a cell thickness of $0.78(2)\,\mu\text{m}$, a cell temperature of $200\,^\circ\text{C}$, and a reservoir temperature of $180\,^\circ\text{C}$. The probe laser is scanned over the D_2 line. The peak-intensity of the LIAD laser is changed for each measurement.
Two exemplary measurements are shown in figure 8.3 with the same experimental parameters, except the different peak-intensity of the LIAD laser. The map on the left is taken with an intensity $I = 2.6(3)\,\text{MW}\,\text{cm}^{-2}$ and the map on the right has an intensity $I = 211(21)\,\text{MW}\,\text{cm}^{-2}$, which is roughly 80 times larger.
The low intensity measurement in figure 8.3 (left) shows the full spectrum of the D_2 transition along the laser detuning axis, for a fixed time t. There are also dips visible at the resonances, which occur similar to the measurement shown in figure 6.10. For times shortly after the LIAD pulse, the spectrum is broadened by the Doppler broadening of the desorbed atoms and by the transit time broadening. At longer times the spectrum is getting narrower and vanishes, as the desorbed atoms hit the cell walls, or leave the probe volume. The estimated density for the low intensity, from

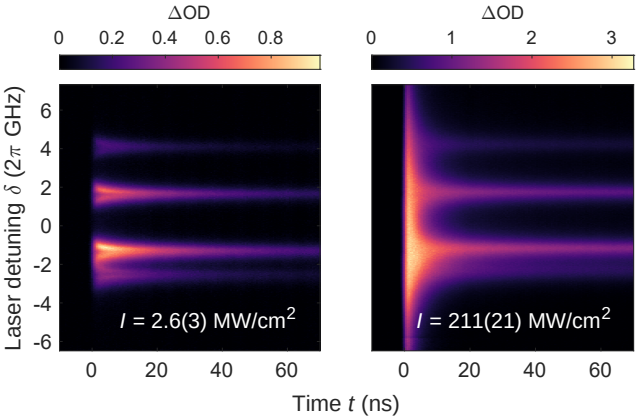

Figure 8.3 Time- and detuning-resolved ΔOD: These measurements are performed in a thinner part of the cell with $L = 0.78(2)\,\mu m$. One map corresponds to a low peak-intensity (left) of the desorption pulse, while the other map corresponds to a high peak-intensity (right) of the LIAD pulse. The high intensity also causes a high atomic density, leading to a broadening and shift of the D_2 transition for short times $t < 5\,ns$. Zero laser detuning is set to the weighted line-center of the D_2 transition. The shown data are a 21 h (left) and a 4 h (right) measurement. A similar figure has already been published by the author of this thesis in [2].

the fitted broadening, is $n_{\text{broadening}} \approx 1.9 \times 10^{15}\,\text{cm}^{-3}$ (at $t = 2\,ns$), which leads to $n/k^3 \approx 3.6$ where dipole-dipole interactions can be neglected.
Due to the lack of an explicit scaling behavior, it is assumed that the number of desorbed atoms, respectively the atomic density, is monotonically increasing with the intensity of the LIAD pulse. Therefore, the density for the high intensity measurement is higher compared to the low intensity measurement. The estimated density for the high intensity is $n_{\text{broadening}} \approx 7.4 \times 10^{16}\,\text{cm}^{-3}$ (at $t = 2\,ns$), which leads to $n/k^3 \approx 142$ where dipole-dipole interactions have a significant influence on the spectrum.
In figure 8.3 (right) a strong broadening can be observed in the first nanoseconds after the LIAD pulse ($t < 5\,ns$).This broadening is attributed to the density-dependent self-broadening. A fit to the spectrum at $t = 2\,ns$ results in a broadening of $\Gamma_{\text{self}} \approx 590\Gamma_0$. The detailed description of the

fitting routine can be found in subsection 8.2.2.
The broadening is accompanied by a shift of the line-center towards lower energies. This red-shift of the transition is attributed to the density-dependent dipole-dipole shift. The measurement in figure 8.3 (right) has a shift of $\Delta_{\mathrm{dd}} \approx -80\Gamma_0$ at $t = 2\,\mathrm{ns}$. It is hard to see the shift effect in the ΔOD map, but a slice along the detuning axis for a specific time shows a clear shift of the broadened transition (see also figure 8.4).
The broadening and shift effects are vanishing with time as the desorbed atoms hit the other cell wall or leave the probe volume hence make the atomic cloud dilute, similar to the low density case. So at $t > 18\,\mathrm{ns}$ all hyper-fine transitions of the ground state of the D_2 line are visible. On the timescale of $t = 20\,\mu\mathrm{s}$, which is the period of the pulse repetition, the system relaxes into the thermal equilibrium.

8.2.2 ElecSus fitting

For a more quantitative discussion on the broadening and shift, an electric susceptibility model is utilized to fit our measurements. There, the software ElecSus[1] [98] is used, which is based on the programming language Python.
In ElecSus, the electric susceptibility of an alkali-metal vapor is calculated, which is then used to state the dissipative and dispersive properties of the vapor. Input parameters to calculate the transmission spectrum are the length of the atomic sample, the temperature, the polarization of the probe electric field and the magnetic field, which is applied to the atoms. Additional parameters are a Lorentzian broadening and a shift of the spectrum, which are used to fit the electric susceptibility model to the measured transmission.
The measured map is sliced into spectra for every time step. During the fitting routine, first the spectra for longer times $t > 30\,\mathrm{ns}$ are fitted, where no extra broadening is observed. The resulting optimized parameters are used as start parameters for the next fit one time step earlier. For the fitting process, the Marquardt–Levenberg methode [99] is chosen, which is included in the ElecSus software. The output of each fit are the op-

[1] The model in ElecSus is based on steady-state behavior of an isotropic atomic vapor, hence it can not capture the full transient dynamics in our desorbed atomic ensemble.

timized parameters, the 1σ standard error of each parameter, as well as the normalized root-mean-square (rms) deviation between the modeled and measured transmission. The parameters, which are fixed to a specific value and which are optimized during the fit, are listed in table 8.1.

Table 8.1 ElecSus parameters: These are the parameters used in the fitting routine of the transmission spectra. In the column "usage" is defined, whether a parameter is fixed, or optimized. The values given for the optimized parameters are the initial values.

Parameter	**ElecSus key**	**Value**	**Usage**
Element	Elem	Rb	Fixed
Transition	Dline	D2	Fixed
Electric field vector	E_in	$\frac{1}{\sqrt{2}}\begin{pmatrix}1\\1\\0\end{pmatrix}$	Fixed
Magnetic field	Bfield	0 G	Fixed
Temperature (for density)	T	200 °C	Optimized
Lorentzian broadening	GammaBuf	$2\pi \times 100$ MHz	Optimized
Frequency shift	shift	$-2\pi \times 10$ MHz	Optimized
Doppler temperature	DoppTemp	0 °C	Fixed
Temperature constrain	Constrain	False	Fixed
Cell thickness	lcell	0.78 µm	Fixed

There is a treatment of the self-broadening already included in ElecSus. This means at a higher cell temperature the density is increasing and thereby also the intrinsic self-broadening gets broader/stronger. For our system, the quantity of the self-broadening actually is the needed value. Therefore, the intrinsic self-broadening in the code of ElecSus is removed to fit the broadened spectrum with the broadening factor Γ_{buf}, which is normally used to include the buffer gas broadening. The factor Γ_{buf} is the width of a Lorentzian curve, which is used to represent the self-broadening. As stated in table 8.1, no magnetic field is applied to the rubidium vapor and the electric field of the probe laser is linearly polarized. For the two temperature values, the constraint between the density and the Doppler broadening of the atoms is turned off. The density is therefore fitted via the temperature, while the Doppler broadening (defined by a Doppler temperature) is kept low, according to $T_{\mathrm{Doppler}} = 0\,^{\circ}\mathrm{C}$. This Doppler temperature is physical not realistic, but for our system

with a large Lorentzian broadening the Doppler broadening is negligible ($\Gamma_{\text{Doppler}} \approx 107\Gamma_0 < \Gamma_{\text{self}} \approx 590\Gamma_0$). Further discussion of the density related to the temperature can be read in subsection 8.3.4.
Exemplary fits to our measurements for a few time steps are shown in figure 8.4. The fits are in good agreement with the measured data points. For a better visibility only every third data point is shown. The errorbars of the measured data in vertical direction show the uncertainty of the measured transmission.
The transmission uncertainty is calculated for each data point with the number of measured photon counts N_{photon}. This is done via the standard deviation of the Poissonian distribution of the photon counts, which is defined as $\Delta N_{\text{photon}} = \sqrt{N_{\text{photon}}}$. The inverse transmission uncertainty

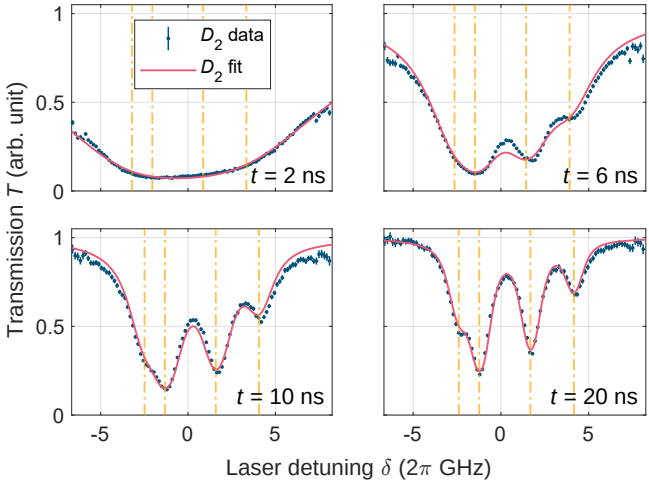

Figure 8.4 ElecSus fit: The measured data points of a D_2 spectrum (blue) are fitted with an electric susceptibility model (red). Each spectrum corresponds to one time step t, which is labeled in the tile plots. The displayed spectra are slices from the map shown in figure 8.3 (right). The fitted positions of the two ground state hyperfine transitions for the two rubidium isotopes are marked with four yellow dashed lines. Note, that only every third data point is shown for better visibility and the vertical errorbars show the uncertainty of the transmission. Zero laser detuning is set to the weighted line-center of the D_2 transition.

is also used as weights of the data points for the ElecSus fits. Therefore, the code of ElecSus is modified to pass the weights as argument to the actual fitting method.
The broadening of the spectrum is clearly visible in figure 8.4. To illustrate the shift of the spectrum, the two ground state hyperfine transitions for the two rubidium isotopes are marked as guide to the eye. These four lines are shifted according to the fitted value for the individual time steps. The fit cannot be fully trusted at $t = 2\,\mathrm{ns}$ since the wings must be taken into account for a proper determination of the width of the spectrum. Since our scan range was not larger, we cannot rule out a systematic error in fitting. Consequently, the values of the fitted broadening in the first few nanoseconds are probably overestimated. (For more details on the fits, see Appendix B.)

8.3 Transient density-induced dipolar interactions

It is already visible in figure 8.4, that the broadening and line shift is changing on a fast timescale with $t \ll \tau_0$, where τ_0 is the natural decay of the atomic state. According to this, these observations are called transient density-induced dipolar interactions, in contrast to the normally observed steady-state dipolar interactions, e.g. in constant heated, nanometer thick cells [26]. To determine the transient behavior, the electric susceptibility model is fitted to every time step to extract the broadening and shift, while the time binning is $\Delta t = 0.5\,\mathrm{ns}$.

8.3.1 Transient broadening

From the fitted spectra, a Lorentzian shaped broadening is obtained for each time step. As the background signal is already subtracted, only the signal caused by the desorbed atoms is fitted. The fitted broadening is attributed to the self-broadening, which is shown in figure 8.5.
The experimental parameters for these measurements are a cell thickness of $0.78(2)\,\mu\mathrm{m}$, a cell temperature of $200\,^\circ\mathrm{C}$, and a reservoir temperature of $180\,^\circ\mathrm{C}$. The probe laser is scanned over the D_2 line.
To further investigate if the observed broadening is density dependent, the intensity of the LIAD laser is changed to perform the same experi-

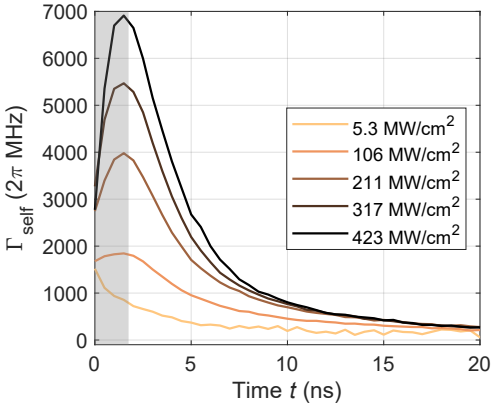

Figure 8.5 Self-broadening depending on the LIAD intensity and time: From the ElecSus fits to a set of D_2 spectra for different LIAD intensities, the self-broadening Γ_{self} over time t is determined. The time binning is $\Delta t = 0.5\,\text{ns}$ and the data points are connected with lines for better traceability. The evolution of the broadening for $t < 2\,\text{ns}$ is not meaningful (gray area), as our measurement resolution is at its limit, the LIAD pulse is still present there, and the electric susceptibility fit is not working perfectly due to the broadened spectrum. The intensity values in the legend are the peak-intensity of the LIAD pulse for the respective measurement. For a higher intensity more atoms are desorbed, which leads to a higher density and thereby to a larger self-broadening. The average measurement time for one LIAD pulse intensity is 4 h.

ment at different cloud densities. As the measurements in figure 8.5 show, the broadening is larger for higher LIAD intensities, which is expected, following the assumption, that more atoms are desorbed for higher LIAD intensities. For long times, with $t > 18\,\text{ns}$, the broadening vanishes, as the density decreases when the atoms hit the other cell wall or leave the probe volume.

The observed self-broadening in these measurements is one order of magnitude larger than other broadening effects, like the Doppler broadening with $\Gamma_{\text{Doppler}} = 2\pi \times 650\,\text{MHz}$. Therefore, the dipole-dipole interaction is the dominating effect in the first 10 ns.

8.3.2 Transient shift

Analogous to the broadening, the shift of the D_2 transition is also retrieved from the electric susceptibility fits for each time step. The fits to the measurement show a negative line shift on the frequency axis, which is a red-shift of the transition. The shift is attributed to the dipole-dipole shift, which is shown in figure 8.6.
For low LIAD intensities, the shift is superimposed with the asymmetric line shape observable in the measurement, shown in figure 6.10. As the atomic density is low for the LIAD intensity of $I = 5.3(5)\,\mathrm{MW\,cm^{-2}}$, the dipole-dipole shift is on the same order of magnitude as this asymmetry and therefore the ElecSus fit will return almost zero shift.
With increasing LIAD intensity the density is increasing, which leads to a

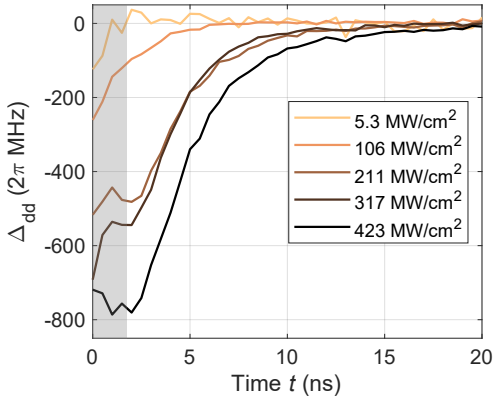

Figure 8.6 Dipole-dipole shift depending on the LIAD intensity and time: From the ElecSus fits to a set of D_2 spectra for different LIAD intensities, the dipole-dipole shift Δ_{dd} over time t is determined. The data points for each measurement are connected for a better traceability. The LIAD peak-intensity of the respective measurement is displayed in the legend. The fitted shift for short times $t < 2\,\mathrm{ns}$ (gray area) is not meaningful, as discussed in the text. For the lowest intensity there is no significant shift, which might be the case, because of the asymmetric line shape for low intensities. This asymmetry (see figure 6.10) might cancel the dipole-dipole shift. The average measurement time for one LIAD pulse intensity is 4 h.

stronger red-shift due to the dipole-dipole interactions. In figure 8.6 it is clearly visible, that the shift is not well defined for short times $t < 2\,\mathrm{ns}$, as the data points do not follow any trend. There, the measured transmission spectra have a shape, which is different from the susceptibility model and can not be fitted nicely. Also the desorption pulse has its falling edge until $t \approx 1\,\mathrm{ns}$, which leads to false counts on the SPCM. So the desorption pulse might deform the spectrum for short times. Additionally, there can be other effects, which lead to a shift or an asymmetry of the spectra. One possible effect can be the van der Waals force between an atom and a surface. Depending on the atom and the surface this force can be attractive [83, 84, 100] or repulsive [101] when the atoms are close (in the range of 10–100 nm) to the surface.
With a higher time resolution it will be possible to measure the effects in the first two nanoseconds $t < 2\,\mathrm{ns}$, but in our measurement it is only possible to state values for the broadening and shift for times $t \geq 2\,\mathrm{ns}$. For the further discussion of the transient evolution of the broadening and shift, the data point at $t = 2\,\mathrm{ns}$ is used as the first value. Compared to the natural lifetime of the D_2 transition, which is $\tau_0 = 26.2\,\mathrm{ns}$ [46], our observation of the transient evolution of the broadening and shift is one order of magnitude faster.

8.3.3 Comparison of the D_1 and D_2 transitions

In our experimental setup there is the opportunity to exchange the probe laser. All previous shown measurements and also the Monte Carlo simulation have been performed with the D_2 transition at a wavelength of 780 nm. To compare those measurements with a second set of measurements, a probe laser at a wavelength of 795 nm is used, which is probing the D_1 transition of rubidium.
The main difference between the two transitions is the different total angular momentum in the excited state, given by the quantum number J_e. For the D_1 transition this is $J_\mathrm{e} = 1/2$ and for the D_2 transition it is $J_\mathrm{e} = 3/2$. Connected to this, also the transition dipole matrix element, reduced to J, is different, which is given in equation 8.6.
For measurements with identical experimental parameters, except the probe wavelength, there should be a different value for the self-broadening

and dipole-dipole shift for D_1 and D_2. From the measurement sets, one measurement each with a LIAD peak-intensity of $I = 317(32)\,\mathrm{MW\,cm^{-2}}$ is chosen. The fitted broadening and shift is plotted in figure 8.7.

Our system is probing a transient density-induced behavior of dipolar interactions. To observe possible intrinsic transient effects of dipolar interactions beyond the density-induced effects a higher temporal resolution is needed. To describe our measurements, the steady-state dipolar model is applied, while every time step is considered to be in the steady-state regime individually. This is fairly valid, as the many-body interactions are equilibrating due to motional dephasing on a time scale of $\approx 1\,\mathrm{ns}$.

The transient broadening figure 8.7 (left) is high for times directly after the desorption pulse ($t \approx 2\,\mathrm{ns}$). With increasing time, the atomic density and thereby also the self-broadening decreases, as the atoms hit the other cell wall, or leave the probe volume. According to equation 8.15 and dif-

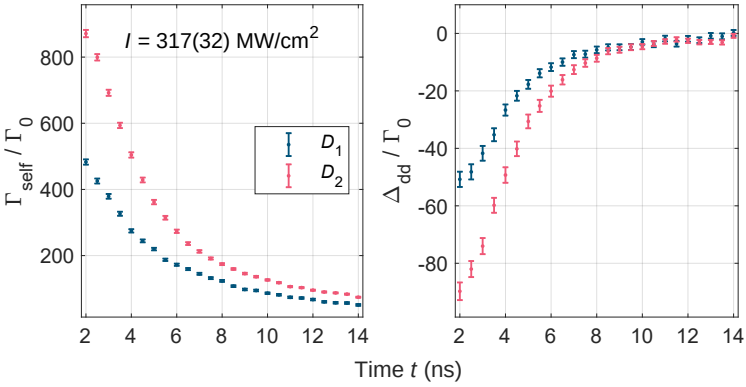

Figure 8.7 Comparison of the D_1 and D_2 transition: The fitted broadening (left) and shift (right) for the two transitions is given in multiple of the respective natural decay rate Γ_0. The self-broadening and dipole-dipole shift for the D_2 transition (red) is stronger than for the D_1 transition (blue), as expected from the values in equation 8.7. Further discussion is in the text. The error bars are the standard deviation of the ElecSus fits in vertical direction and the total time jitter in horizontal direction. The LIAD peak-intensity is $I = 317(32)\,\mathrm{MW\,cm^{-2}}$. The measurement time is 2.5 h (D_1) and 3 h (D_2). A similar figure has already been published by the author of this thesis in [2].

ferent transition dipole moments, an expected difference between the D_1 and D_2 transition is visible.
The behavior of the dipole-dipole shift in figure 8.7 (right) is similar to the transient evolution of the broadening. The strong red shift decreases with increasing time and approaches zero. There is also a difference between the D_1 and D_2 transition, as expected.
According to the steady-state model, there is a certain ratio between the D_1 and D_2 transition of rubidium, given by d_J^2 and the degeneracy of the excited states g_e. For the self-broadening this gives a theoretical ratio of

$$r_{\text{broadening}} = \frac{\Gamma_{\text{self},D_2}}{\Gamma_{\text{self},D_1}} = \frac{d_{J,D_2}^2}{d_{J,D_1}^2} \sqrt{\frac{g_{e,D_1}}{g_{e,D_2}}} \approx \sqrt{2}\,. \tag{8.18}$$

For the dipole-dipole shift the degeneracy does not play a rule, and as the geometry of the cell is not changing (cell thickness $L \approx \lambda_{\text{probe}}$ for D_1 and D_2, respectively), the ratio is only depending on the dipole matrix element squared. The resulting theoretical ratio for the dipole-dipole shift is

$$r_{\text{shift}} = \frac{\Delta_{\text{dd},D_2}}{\Delta_{\text{dd},D_1}} = \frac{d_{J,D_2}^2}{d_{J,D_1}^2} \approx 2\,. \tag{8.19}$$

To compare the theoretical ratios with the measured values in figure 8.7, the time-dependent ratios are calculated from these data points. The ratios with error bars are shown in figure 8.8.
The error bars in vertical direction are calculated via error propagation from the standard deviation of the individual broadening and shift values. The horizontal error bar is the total time jitter of the measurements. As the cloud becomes dilute, the shift values are small for $t > 10\,\text{ns}$ and the error bars in vertical direction are getting large. Therefore, it is not possible to state a ratio for the shift for $t > 10\,\text{ns}$.
The time evolution of the broadening ratio has some deviations from the value of the theoretical steady-state model. In the beginning at $t = 2\,\text{ns}$ the ratio is $r_{\text{broadening}} \approx 2$ and approaches the theoretical steady-state value of $r_{\text{broadening}} \approx \sqrt{2}$ at a time of $t \approx 7\,\text{ns}$. The ratio then is almost constant until the end of the selected time-window. A difference between the measurement and the steady-state model is observable in the first few nanoseconds.

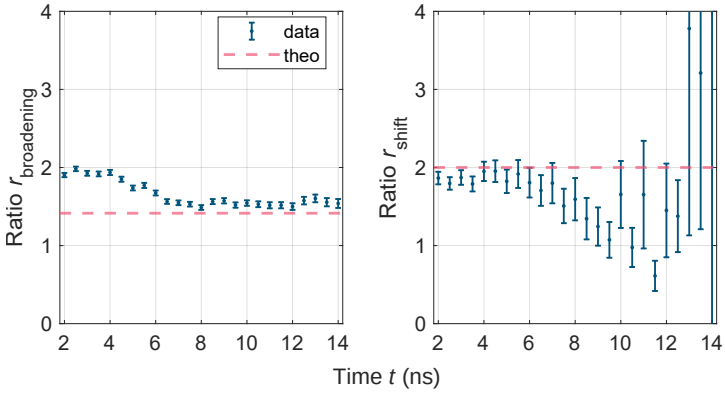

Figure 8.8 Ratios of the D_1 and D_2 transition: For the broadening, the ratio D_2 over D_1 is given by $r_{\text{broadening}}$ (left, blue). The analog ratio for the shift is given by r_{shift} (right, blue). The theoretical steady-state values for the ratios are marked with a dashed line, respectively for the broadening and shift (red). The time-dependent evolution of the ratios and the error bars is discussed in the text. The LIAD peak-intensity is $I = 317(32)\,\text{MW}\,\text{cm}^{-2}$. The used data is shown in figure 8.7.

There is room for interpretations to explain the found deviations. It seams, that the degeneracy and thereby the number of involved levels, which is lowering the ratio to $\sqrt{2}$, only matters after 7 ns. Before, there is the bare ratio of the dipole matrix elements squared visible for the broadening. Another possible explanation is a systematic error of the fitted broadening. The shown errors in figure 8.7 are the standard deviation of the fit, which misses the effect, that the wings of the signal are not captured. Especially for the D_2 transition with a stronger broadening, the wings are not fully captured in the measured scan range in the first 5 ns. Therefore, it is possible that the electric susceptibility fit to our data overestimates the width of the D_2 spectrum. In consequence, the ratio of the broadening deviates from the theoretical ratio. (For more details on the fits, see Appendix B.) For the ratio of the shift, a different behavior is observed, where the ratio in the beginning at $t = 2$ ns has the same value as the theoretical, steady-state model predicts. This value is $r_{\text{shift}} \approx 2$. This is an indication, that the shift can be determined properly from our data. Only the ratio for

longer times $t > 10\,\text{ns}$ is not meaningful, as the errors are getting large.
To further investigate the deviation of the broadening ratio, two additional datasets with different LIAD intensities are plotted with their ratio in figure 8.9. There, the trend of the ratio of the broadening is similar in all three measurements. The ratio is above the theoretical value and approaches it after $\approx 7\,\text{ns}$. For the higher LIAD intensity, the deviation of the ratio is even stronger, which strengthen the assumption, that the fitted broadening is not captured correctly, as the wings of the signal for negative and positive detunings are missing.
All in all it is visible that there is a clear difference of the ratio of the broadening between the steady-state model and the measurement in the first $7\,\text{ns}$. After that, the ratio follows the dipolar model, which holds also true for the ratio of the shift.

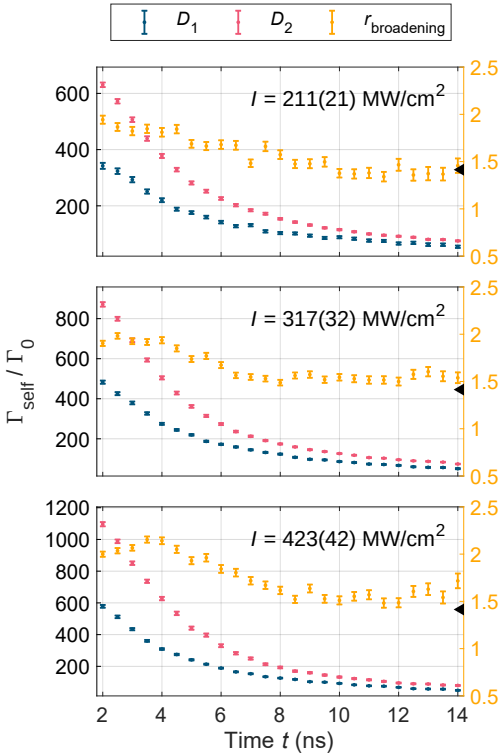

Figure 8.9 Broadening and ratio for different densities: The broadening is plotted for the D_1 (blue) and D_2 (red) transition for different LIAD intensities, which correspond to different atomic densities. For higher intensities, the self-broadening is larger. The ratio of the broadening $r_{\text{broadening}}$ (yellow) is plotted on the right vertical axis, where the theoretical value is marked with a black triangle. All three measurements show a similar behavior of the deviating ratio, which finally approaches the theoretical value. A similar figure has already been published by the author of this thesis in [2].

8.3.4 Transient density

There is a certain density in the micro-cell given by the vapor-pressure. This background density is determined by the temperature of the reservoir, which is 180 °C, leading to density of $n_{\text{background}} \approx 10^{14}\,\text{cm}^{-3}$. For the evaluation of the measurements of the LIAD effect, the background is subtracted and only the desorbed atoms are considered. Here, density values gained from the measurements in the thin cell are stated.
A first approach would be to use the fitted temperature from the ElecSus model. The resulting density is based on the vapor-pressure for a constant temperature in an isotropic medium. This density is not useful in our anisotropic system of desorbed atoms, which move in a defined direction.
As alternative,the self-broadening and dipole-dipole shift values are used to extract a density. Therefore, equation 8.15 and equation 8.16 are taken to calculate a time-dependent density from the broadening and shift values, which are plotted in figure 8.7. The resulting density curves are shown in figure 8.10.
The exact evolution of the transient density can be different in reality, but one notices, that the curves look similar for the two transitions and also for the broadening and shift. The values are at least on the same order of magnitude. At a time $t = 2\,\text{ns}$, the density is $n_{\text{broadening}} \approx 4.3 \times 10^{16}\,\text{cm}^{-3}$, which is two orders of magnitude larger than the background density. In that density regime the dipolar interaction is strong, as the atoms are on average closer than the reduced wavelength $\lambda\!\!\!^{-}$. This is also expressed by

$$n_{\text{broadening}}/k^3 \approx 82\,, \tag{8.20}$$

where the density is significant larger than the wavevector cubed.

8.4 Conclusion

With our pulsed LIAD method, transient density values are reached, which are comparable to vapor cell experiments, where the cells are heated above 300 °C [26]. The density is increased to a regime, where dipolar interactions with a ground state transition are observable. The D_1 and D_2 transition of rubidium are used, to probe the atom ensemble generated by LIAD. Therefore, a strong broadening, the so called self-broadening,

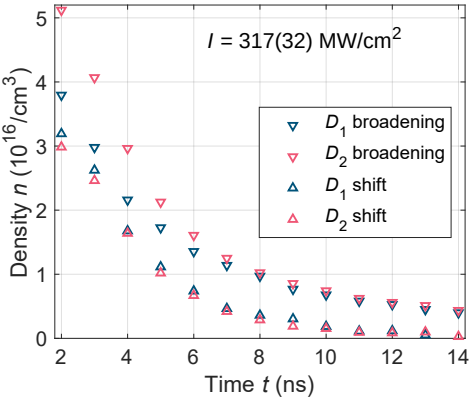

Figure 8.10 Density from broadening and shift: The density values are calculated using equation 8.15 and equation 8.16 from the broadening (marker: ∇) and shift (marker: $\triangle$). The calculations are done for the D_1 transition (blue) and the D_2 transition (red). Note, that only every second value is shown for better visibility and the error bars are not shown, but they are smaller than the size of the marker symbols. The LIAD peak-intensity is $I = 317(32)\,\mathrm{MW\,cm^{-2}}$. The used data is shown in figure 8.7.

and a red-shift of the transition, caused by the dipole-dipole shift, which depends on the Lorentz-Lorenz shift are measured. By comparing the two transitions with different angular quantum number J, and thereby different dipole matrix elements d_J, it is confirmed that the observed effects are caused by dipolar interactions between rubidium atoms.
With our transient density-induced measurement on the nanosecond timescale, a deviation from the steady-state dipolar model in the first 7 ns is visible. These deviations are mainly attributed to systematic errors in the evaluation of the broadening. However, it can not be excluded that there are actual intrinsic transient effects of the dipole-dipole interaction. Besides that the observation of dipolar interactions in a transient density-induced regime are consistent with the established steady-state dipolar model.

8.5 Further ideas

A big advantage of our system is the controllable trigger of the desorption pulse, which allows to switch the density within nanoseconds. This method opens the field for various experiments, where a local, high density is needed on the nanosecond timescale.
The fast switching of the density can for example be used with integrated photonic structures [102]. There it is proposed, to use the desorbed atoms with a photonic crystal cavity [103, 104], such that the atoms fly through the holes in the photonic crystal cavity and interact locally with the guided light mode.
There, it becomes possible to realize large optical nonlinearities in vapor cell experiments, which is the basis for switchable beamsplitters, routers and nonlinear quantum optics. As the atoms are desorbed on the nanosecond timescale, optical systems with a GHz bandwidth are feasible.
Instead of just measuring the transmitted photons, one can also use two single-photon counting modules in a Hanbury Brown-Twiss setup [105]. There, the transmitted photons are separated by a 50:50 beam splitter on two SPCMs. With this kind of setup it is possible to calculate the correlation between two photons, which originate from the atomic sample.
The idea is to observe a change of the light statistics, while the atomic density is increased with LIAD and the dipolar interactions play a role. This should be measured with a locked probe laser frequency, to accumulate data where the LIAD effect produces the strongest signal. Then the correlation between photons, detected on the two detectors, can be calculated for each time step.

Conclusion and outlook

In the course of this thesis, two essential building blocks for our approach of a single-photon source were investigated. The single-photon generation is based on thermal rubidium Rydberg atoms, which are excited within a four-wave mixing (FWM) process. This is all done in a confined volume inside a micrometer-sized vapor cell to exploit the effect of the Rydberg blockade.

One of the building blocks is the FWM process itself, which was improved in terms of a second generation experiment. We decided to use an inverted FWM scheme, where the excitation and deexcitation from the 6P intermediate states into the $32S_{1/2}$ Rydberg state are addressed using Yb-doped fiber amplifier laser systems. The ground state transition of the inverted FWM is excited by a 422 nm diode laser. The fiber amplifier laser systems allow a significant increase of the repetition rate into the 100 kHz regime, compared to the previous experiment at only 50 Hz. Both the time-jitter < 10 ps and amplitude-jitter $< 1\,\%$ are low, while pulse peak powers of 100 W are achieved.

We performed simulations of the FWM process in order to define the requirements for the laser systems. As no commercially available laser system can meet our requirements, a customized fiber amplifier is needed to amplify Fourier-limited pulses at wavelengths around 1016 nm. Two custom-made fiber amplifier systems have been built in collaboration with the Fraunhofer Institute for Applied Optics and Precision Engineering (IOF) in Jena, which are integrated into rack cases shown in figure 8.11. The commissioning of these systems allowed us to characterize the pulse

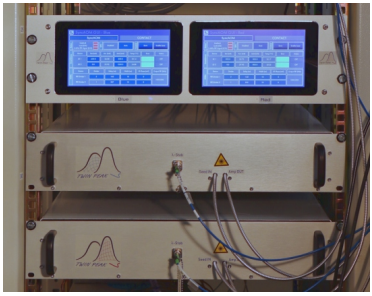

Figure 8.11 Photo of the fiber amplifiers: The two fiber amplifiers are integrated into two rack cases. The controller above is used to set the power and the AOM synchronization.

generation, which is essential for the dynamics of the FWM process. As a first proof of the capabilities of the new laser systems, Rydberg Rabi oscillations were measured in a three-level system, where oscillation frequencies close to 1 GHz have been observed. The results are similar to previously performed measurements in the other excitation scheme [18]. The observation of Rabi oscillations shows, that this system can be coherently driven faster than any dephasing mechanism, which would destroy the coherence in the system. This proves that the coherent FWM process leading to the emission of coherent photons is possible.

The second building block is the controlled increase of the atomic density via light-induced atomic desorption (LIAD) on nanosecond timescales. A nanosecond pulsed, 532 nm laser was set up as desorption laser to investigate the time- and detuning-dependent increase of the OD. In this experiment, it is possible to reach a regime where the density is so high that dipolar interactions were observed in a thermal rubidium vapor. The density, respectively the number of desorbed atoms, can be controlled via the intensity of the desorption laser. The size of the atomic ensemble is defined by the waist of the desorption beam and by the local cell thickness inside the wedge-shaped micro-cell. By switching the density within $\approx 2\,\mathrm{ns}$ from $n_{\mathrm{background}} \approx 10^{14}\,\mathrm{cm}^{-3}$ to $n_{\mathrm{LIAD}} \approx 10^{16}\,\mathrm{cm}^{-3}$, it becomes possible to study dipolar interactions in a transient density. Therefore, the interactions build up on a nanosecond timescale, which is much faster than the natural atomic lifetime of $\tau_0 = 26.2\,\mathrm{ns}$ for the D_2 transition. With a weak probe laser, a strong broadening and line shift of the D_1 and D_2 absorption spectrum was observed. The broadening and line shift depend on the density and dipole moment. For the D_2 transition a self-broadening of up to $\Gamma_{\mathrm{self},D_2} \approx 840\Gamma_0$ and a dipole-dipole shift of up to $\Delta_{\mathrm{dd},D_2} \approx -90\Gamma_0$ were measured at $t = 2\,\mathrm{ns}$ after the desorption pulse, which had an intensity of $I = 317(32)\,\mathrm{MW\,cm}^{-2}$ corresponding to $n_{\mathrm{LIAD}} \approx 4.3 \times 10^{16}\,\mathrm{cm}^{-3}$. In comparison, the broadening without LIAD is given by the Doppler width of the thermal atoms, which is $\Gamma_{\mathrm{Doppler}} \approx 107\Gamma_0$ for $T = 200\,^{\circ}\mathrm{C}$.
The transient density-induced dipolar interactions in our measurement are described by the well established steady-state dipolar model. This is observable in the ratios between the D_1 and D_2 transitions, which show almost the same values as the theoretical model predicts. Minor deviations

from the theory probably come from a systematic error in the evaluation, namely a to small frequency scan range of the laser.
Whether the dipolar interactions possess intrinsic transient dynamics remains an open question. With our measurements we can neither confirm nor disprove that such effects exist, since our temporal resolution is not sufficient and the transient density overlays possible intrinsic transient dynamics of the dipolar interaction itself.
Additionally it was possible to investigate the properties of the desorption process itself in less dense regimes. Therefore, a kinematic model of desorbed atoms was developed to simulate an OD map numerically. By comparing the Monte Carlo simulation with our measurements, the simulation parameters could be optimized to find a fitting 3D velocity distribution of the desorbed atoms, which is challenging as only one dimension is probed. The resulting velocity distribution in the model shows, that the atoms get desorbed with an absolute velocity distribution similar to the Maxwell-Boltzmann distribution and an angular distribution as defined by the $\cos(\theta)$-Knudsen law. To reach a good agreement between the measurement and simulation, a reemission or reflection of the atoms must be included when they hit the opposite cell wall. The simple model does not capture all features observed in the measurement, but still provides a starting point for more sophisticated desorption models.

The observations in this thesis show, that the Rydberg excitation within the inverted FWM process works as expected from the simulations. The next steps will be the observation of FWM photons at 420 nm in a larger cell, e.g. in a 220 µm thick vapor cell. During the last weeks, writing this thesis, my colleagues managed to observe the first FWM signal using the new fiber amplifier systems. Other challenging issues like the volume confinement and the wavelength separation have to be tackled, to be able to observe the first blue antibunched photons in our experiment.

On the other hand, the desorption process with the emission of atoms from the surface can be combined with integrated photonic structures. The idea is to increase the density close to a waveguide to enhance the atom-light interaction, which increases the non-linearity [106]. For example, the exotic velocity distribution of the desorbed atoms may help to “shoot” the atoms through the holes of a photonic crystal cavity [103].

Another approach is the integration of a microscopic optical cavity into a vapor cell, based on two highly reflective windows. Therefore, the atom-light interaction is enhanced by the cavity, if the resonances of the atom and the cavity overlap. One technical challenge is to manufacture such a micro cavity, because the high-reflection coatings can easily be destroyed at high temperatures during the assembly of a vapor cell. After a successful fabrication, it will be difficult to tune the resonance of the micro cavity to hit the atomic resonance. It will probably be necessary to use both thermal expansion of the cavity and external pressure on the vapor cell via a piezo crystal.

Appendix

Appendix A

LIAD with rotated cell

The asymmetry, observable in our measurement of the LIAD effect (e.g. in figure 6.10), is not expected and might occur because of different surface properties. To prove this, a similar kind of micro-cell is used for two measurements, while the second measurement is performed with a 180° rotated cell. The results are shown in figure A.1.
The experimental parameters for these measurements are a cell thickness of $L = 3.9(1)\,\mu\text{m}$, a cell temperature of 150 °C and a reservoir temperature

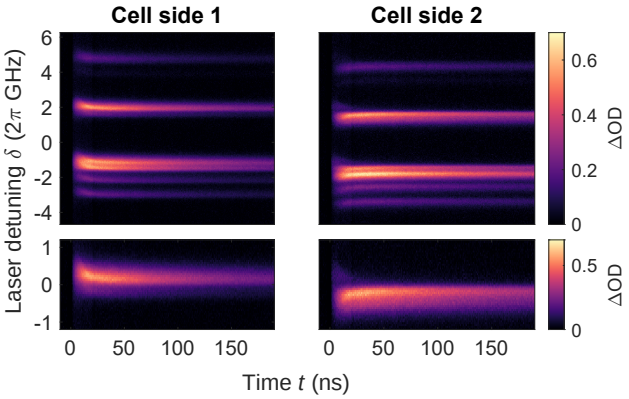

Figure A.1 ΔOD for rotated cell: The ΔOD is measured for one side of the cell (left column) and for a 180° rotated cell at the same spot (right column). The full D_2 spectra (top row) are taken to determine the sign of the detuning axis. A zoom-in on the ^{85}Rb $F_g = 2$ transition (bottom row) shows a clear change of the asymmetry when rotating the cell by 180°.

of 130 °C. The probe laser is scanned over the D_2 line. The peak-intensity of the LIAD laser is at $I = 2.5(3)\,\mathrm{MW\,cm^{-2}}$.
The measurements show, that the asymmetry can be roughly inverted when rotating the cell by 180°. Thereby, the number of atoms flying in or against laser propagation direction also changes. The asymmetry in our measurements can therefore very likely be assigned to surface properties [107]. The sapphire coating in the micro-cell can have different properties on each side, e.g. due to the manufacturing process. The cells are molten together at their outer edge, which is done by hand and not evenly. As a result, the coating on both sides is different, leading to different desorption rates.

Appendix B

Details on the ElecSus fits

To extract the information about the broadening and shift from our measured data, the susceptibility model, included in ElecSus, is used. Here, some exemplary fits are shown, which result in the statements and figures of chapter 8. There, the comparison of the D_1 and D_2 transition leads to a deviation of the ratio of the broadenings to the theoretical steady-state value. To give a possible explanation for that, the ElecSus fits are examined more closely.

The exemplary fits for the D_1 and D_2 transition are shown in figure B.1 for different time steps. The LIAD peak-intensity for both measurements is $I = 317(32)\,\mathrm{MW\,cm^{-2}}$. Note, that only every third data point is shown for better visibility and the vertical errorbars show the uncertainty of the transmission. Zero laser detuning is set to the weighted line-center of the respective transition. The four fitted line positions are the two hyperfine-splitted ground state transitions for the two rubidium isotopes. These lines are shifted according to the fitted shift value for the respective time step.

The fit at $t = 0.5\,\mathrm{ns}$ shows, that the electric susceptibility model fit can not capture the measured data, as the spectrum is broad and at the same time has some narrow, unexplained peaks. One explanation could be the an-isotropic velocity distribution of the desorbed atoms.

For $t = 2\,\mathrm{ns}$ and $t = 4\,\mathrm{ns}$ the broadening of the D_2 spectra are overestimated by the fit, as the red curve at the wings is below the data points. This is probably caused by the scan range of the laser being too small. For the D_1 spectra this overestimation is not so strong, as the absorption is weaker, caused by the weaker transition dipole matrix element.

For times $t > 7\,\text{ns}$ the fits are capturing the measured data with a good agreement.

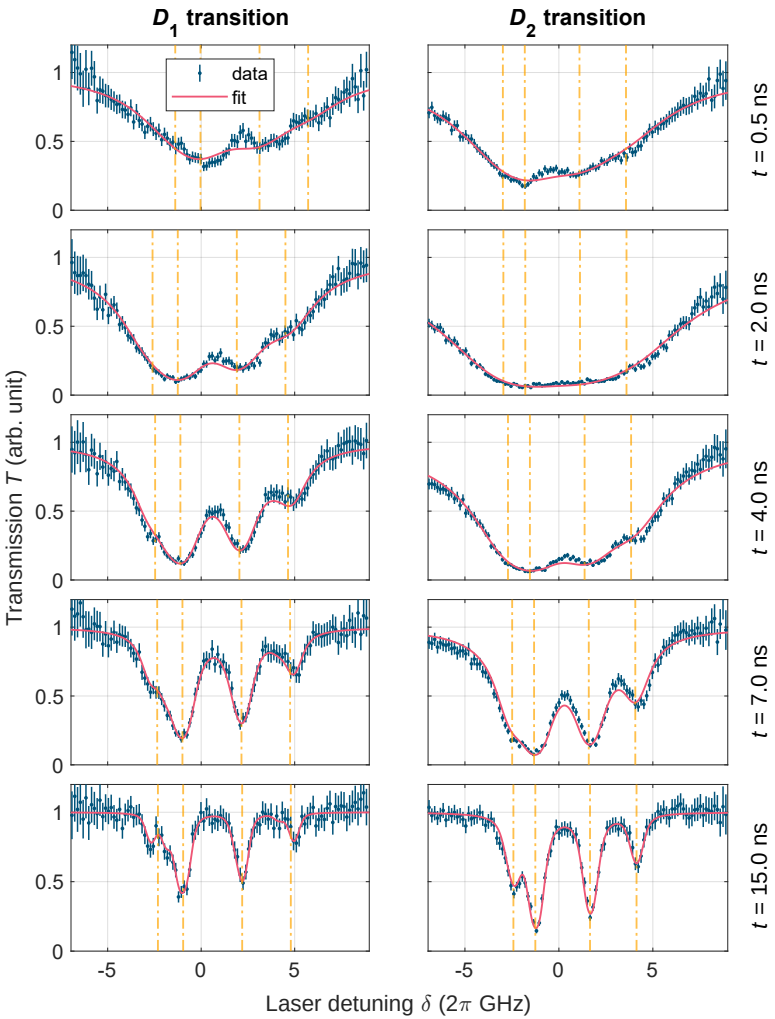

Figure B.1 ElecSus fit: The measured data points (blue) of the D_1 (left) and D_2 (right) spectrum are fitted with an electric susceptibility model (red). Each spectrum corresponds to one time step t, which is labeled next to each row. The four fitted line positions (yellow) result from the fit. Details are in the text. A similar figure has already been published by the author of this thesis in [2].

Bibliography

[1] O. de Vries et al., *Highly customized 1010 nm, ns-pulsed Yb-doped fiber amplifier as a key tool for on-demand single-photon generation*, Opt. Express **28**, 17362–17373 (2020). pp. iii, xiii, 7, 31–35, 38, 41

[2] F. Christaller, M. Mäusezahl, F. Moumtsilis, A. Belz, H. Kübler, H. Alaeian, C. S. Adams, R. Löw, and T. Pfau, *Transient density-induced dipolar interactions in a thin vapor cell*, Phys. Rev. Lett. **128**, 173401 (2022). pp. iii, xiii, 55, 62, 64, 72, 75, 92, 95, 109, 117, 121, VII

[3] I. Mirgorodskiy, F. Christaller, C. Braun, A. Paris-Mandoki, C. Tresp, and S. Hofferberth, *Electromagnetically induced transparency of ultra-long-range Rydberg molecules*, Phys. Rev. A **96**, 011402 (2017). p. iii

[4] A. Paris-Mandoki, C. Braun, J. Kumlin, C. Tresp, I. Mirgorodskiy, F. Christaller, H. P. Büchler, and S. Hofferberth, *Free-Space Quantum Electrodynamics with a Single Rydberg Superatom*, Phys. Rev. X **7**, 041010 (2017). p. iii

[5] R. P. Feynman, *Simulating physics with computers*, International Journal of Theoretical Physics **21**, 467–488 (1982). pp. ix, 1, 9

[6] E. Knill, R. Laflamme, and G. J. Milburn, *A scheme for efficient quantum computation with linear optics*, Nature **409**, 46–52 (2001). pp. ix, 1, 9

[7] J. L. O'Brien, *Optical quantum computing*, Science **318**, 1567–1570 (2007). pp. ix, 1, 9

[8] V. Scarani, H. Bechmann-Pasquinucci, N. J. Cerf, M. Dušek, N. Lütkenhaus, and M. Peev, *The security of practical quantum key distribution*, Reviews of Modern Physics **81**, 1301–1350 (2009). pp. ix, 1

[9] L. M. Duan, M. D. Lukin, J. I. Cirac, and P. Zoller, *Long-distance quantum communication with atomic ensembles and linear optics.* Nature **414**, 413–8 (2001). pp. ix, 1

[10] K. Azuma, K. Tamaki, and H.-K. Lo, *All-photonic quantum repeaters*, Nature Communications **6**, 6787 (2015). pp. ix, 1

[11] H. J. Kimble, M. Dagenais, and L. Mandel, *Photon antibunching in resonance fluorescence*, Phys. Rev. Lett. **39**, 691–695 (1977). pp. ix, 1, 9

[12] A. Kuhn, M. Hennrich, and G. Rempe, *Deterministic single-photon source for distributed quantum networking*, Phys. Rev. Lett. **89**, 067901 (2002). pp. ix, 1

[13] M. D. Lukin, M. Fleischhauer, R. Côtè, L. M. Duan, D. Jaksch, J. I. Cirac, and P. Zoller, *Dipole blockade and quantum information processing in mesoscopic atomic ensembles*, Phys. Rev. Lett. **87**, 037901 (2001). pp. ix, 1, 9

[14] Y. O. Dudin and A. Kuzmich, *Strongly interacting Rydberg excitations of a cold atomic gas*, Science **336**, 887–889 (2012). pp. ix, 1, 10

[15] T. Peyronel, O. Firstenberg, Q. Y. Liang, S. Hofferberth, A. V. Gorshkov, T. Pohl, M. D. Lukin, and V. Vuletić, *Quantum nonlinear optics with single photons enabled by strongly interacting atoms*, Nature **488**, 57–60 (2012). pp. ix, 1, 10

[16] F. Ripka, H. Kübler, R. Löw, and T. Pfau, *A room-temperature single-photon source based on strongly interacting Rydberg atoms*, Science **362**, 446–449 (2018). pp. ix–xi, 1, 2, 10, 26

[17] A. K. Mohapatra, T. R. Jackson, and C. S. Adams, *Coherent optical detection of highly excited Rydberg states using electromagnetically induced transparency*, Phys. Rev. Lett. **98**, 113003 (2007). pp. x, 1, 36, 47

[18] B. Huber, T. Baluktsian, M. Schlagmüller, A. Kölle, H. Kübler, R. Löw, and T. Pfau, *GHz Rabi flopping to Rydberg states in hot atomic vapor cells*, Phys. Rev. Lett. **107**, 243001 (2011). pp. x, xi, 1, 3, 43, 50, 126

[19] F. Ripka, Y.-H. Chen, R. Löw, and T. Pfau, *Rydberg polaritons in a thermal vapor*, Phys. Rev. A **93**, 053429 (2016). pp. x, 1, 33

[20] M. M. Müller, A. Kölle, R. Löw, T. Pfau, T. Calarco, and S. Montangero, *Room-temperature Rydberg single-photon source*, Phys. Rev. A **87**, 053412 (2013). pp. x, 2

[21] A. Kölle, G. Epple, H. Kübler, R. Löw, and T. Pfau, *Four-wave mixing involving Rydberg states in thermal vapor*, Phys. Rev. A **85**, 063821 (2012). pp. x, 2

[22] B. Huber, A. Kölle, and T. Pfau, *Motion-induced signal revival in pulsed Rydberg four-wave mixing beyond the frozen-gas limit*, Phys. Rev. A **90**, 053806 (2014). pp. x, 2

[23] T. Baluktsian, C. Urban, T. Bublat, H. Giessen, R. Löw, and T. Pfau, *Fabrication method for microscopic vapor cells for alkali atoms*, Opt. Lett. **35**, 1950–1952 (2010). pp. x, 2

[24] R. Heidemann, U. Raitzsch, V. Bendkowsky, B. Butscher, R. Löw, L. Santos, and T. Pfau, *Evidence for coherent collective Rydberg excitation in the strong blockade regime*, Phys. Rev. Lett. **99**, 163601 (2007). pp. x, 2, 24, 55

[25] J. B. Balewski, A. T. Krupp, A. Gaj, S. Hofferberth, R. Löw, and T. Pfau, *Rydberg dressing: understanding of collective many-body effects and implications for experiments*, New Journal of Physics **16**, 063012 (2014). pp. x, 2, 24, 55

[26] J. Keaveney, A. Sargsyan, U. Krohn, I. G. Hughes, D. Sarkisyan, and C. S. Adams, *Cooperative Lamb shift in an atomic vapor layer of nanometer thickness*, Phys. Rev. Lett. **108**, 173601 (2012). pp. x–xii, 2, 3, 100, 105, 106, 113, 122

[27] T. Peyrot, Y. R. P. Sortais, A. Browaeys, A. Sargsyan, D. Sarkisyan, J. Keaveney, I. G. Hughes, and C. S. Adams, *Collective Lamb shift of a nanoscale atomic vapor layer within a sapphire cavity*, Phys. Rev. Lett. **120**, 243401 (2018). pp. x–xii, 2, 3, 100

[28] A. Gozzini, F. Mango, J. H. Xu, G. Alzetta, F. Maccarrone, and R. A. Bernheim, *Light-induced ejection of alkali atoms in polysiloxane coated cells*, Il Nuovo Cimento D **15**, 709–722 (1993). pp. x, 2, 57

[29] M. Meucci, E. Mariotti, P. Bicchi, C. Marinelli, and L. Moi, *Light-induced atom desorption*, EPL (Europhysics Letters) **25**, 639 (1994). pp. x, 2, 57

[30] E. B. Alexandrov, M. V. Balabas, D. Budker, D. English, D. F. Kimball, C.-H. Li, and V. V. Yashchuk, *Light-induced desorption of alkali-metal atoms from paraffin coating*, Phys. Rev. A **66**, 042903 (2002). pp. x, 2, 57

[31] K. Rębilas and M. J. Kasprowicz, *Reexamination of the theory of light-induced atomic desorption*, Phys. Rev. A **79**, 042903 (2009). pp. x, 2, 57

[32] P. A. Petrov, A. S. Pazgalev, M. A. Burkova, and T. A. Vartanyan, *Photodesorption of rubidium atoms from a sapphire surface*, Optics and Spectroscopy **123**, 574–577 (2017). pp. x, 2, 57

[33] E. Talker, P. Arora, R. Zektzer, Y. Sebbag, M. Dikopltsev, and U. Levy, *Light-induced atomic desorption in microfabricated vapor cells for demonstrating quantum optical applications*, Phys. Rev. Applied **15**, L051001 (2021). pp. x, 2, 57

[34] A. Belz, *Viel-Wellen-Mischen zu Rydbergzuständen von thermischen Alkalidämpfen zur Anwendung in fortgeschrittener nichtlinearer Optik*, Bachelor thesis (Universität Stuttgart, 2018). pp. xi, 2, 29

[35] B. Heinrich, *Simulation des kohärenten Vier-Wellen-Mischens mit einem wechselwirkenden Rydbergzustand*, Bachelor thesis (Universität Stuttgart, 2020). pp. xi, 2, 29

[36] Y. O. Dudin, L. Li, F. Bariani, and A. Kuzmich, *Observation of coherent many-body Rabi oscillations*, Nature Physics **8**, 790 (2012). pp. xi, 3

[37] B. P. Anderson and M. A. Kasevich, *Loading a vapor-cell magneto-optic trap using light-induced atom desorption*, Phys. Rev. A **63**, 023404 (2001). pp. xi, 3, 57

[38] S. N. Atutov et al., *Fast and efficient loading of a Rb magneto-optical trap using light-induced atomic desorption*, Phys. Rev. A **67**, 053401 (2003). pp. xi, 3, 57

[39] C. Klempt, T. van Zoest, T. Henninger, O. Topic, E. Rasel, W. Ertmer, and J. Arlt, *Ultraviolet light-induced atom desorption for large rubidium and potassium magneto-optical traps*, Phys. Rev. A **73**, 013410 (2006). pp. xi, 3, 57

[40] V. Lorenz, X. Dai, H. Green, T. Asnicar, and S. Cundiff, *High-density, high-temperature alkali vapor cell*, The Review of scientific instruments **79**, 123104 (2009). pp. xii, 3

[41] E. Lewis, *Collisional relaxation of atomic excited states, line broadening and interatomic interactions*, Physics Reports **58**, 1–71 (1980). pp. xii, 3, 102

[42] L. Weller, R. J. Bettles, P. Siddons, C. S. Adams, and I. G. Hughes, *Absolute absorption on the rubidium D_1 line including resonant dipole-dipole interactions*, Journal of Physics B: Atomic, Molecular and Optical Physics **44**, 195006 (2011). pp. xii, 3, 102, 103

[43] W. E. Lamb and R. C. Retherford, *Fine structure of the hydrogen atom by a microwave method*, Phys. Rev. **72**, 241–243 (1947). pp. xii, 3, 105

[44] R. Friedberg, S. Hartmann, and J. Manassah, *Frequency shifts in emission and absorption by resonant systems of two-level atoms*, Physics Reports **7**, 101–179 (1973). pp. xii, 3, 105, 106

[45] H. Dobbertin, R. Löw, and S. Scheel, *Collective dipole-dipole interactions in planar nanocavities*, Phys. Rev. A **102**, 031701 (2020). pp. xii, 3

[46] U. Volz and H. Schmoranzer, *Precision lifetime measurements on alkali atoms and on helium by beam–gas–laser spectroscopy*, Physica Scripta **T65**, 48–56 (1996). pp. xiii, 79, 102, 116

[47] M. Knudsen, *The Kinetic Theory of Gases. Some Modern Aspects* (London, Methuen & Co., 1934). pp. xiv, 85

[48] F. Ripka, *A single-photon source based on strongly interacting thermal Rydberg atoms*, PhD thesis (Universität Stuttgart, 2019). pp. 7, 15, 18, 19, 26, 33, 62, 63, 68

[49] A. Belz, *Towards a high repetition single-photon source using a Rydberg blockade in a vapor cell*, Master thesis (Universität Stuttgart, 2021). pp. 7, 15, 36, 43, 47, 49, 51

[50] P. Michler, A. Kiraz, C. Becher, W. V. Schoenfeld, P. M. Petroff, L. Zhang, E. Hu, and A. Imamouglu, *A quantum dot single photon turnstile device*, Science **290**, 2282–2285 (2000). p. 9

[51] C. Kurtsiefer, S. Mayer, P. Zarda, and H. Weinfurter, *Stable solid-state source of single photons*, Phys. Rev. Lett. **85**, 290–293 (2000). p. 9

[52] C. Brunel, B. Lounis, P. Tamarat, and M. Orrit, *Triggered source of single photons based on controlled single molecule fluorescence*, Phys. Rev. Lett. **83**, 2722–2725 (1999). p. 9

[53] F. Diedrich and H. Walther, *Nonclassical radiation of a single stored ion*, Phys. Rev. Lett. **58**, 203–206 (1987). p. 9

[54] P. G. Kwiat, K. Mattle, H. Weinfurter, A. Zeilinger, A. V. Sergienko, and Y. Shih, *New high-intensity source of polarization-entangled photon pairs*, Phys. Rev. Lett. **75**, 4337–4341 (1995). p. 9

[55] N. Somaschi et al., *Near-optimal single-photon sources in the solid state*, Nature Photonics **10**, 340–345 (2016). p. 10

[56] B. Huber, *Coherent Rydberg dynamics and interaction above room temperature: the frozen gas regime and beyond*, PhD thesis (Universität Stuttgart, 2014). p. 15

[57] L. Mandel and E. Wolf, *Optical coherence and quantum optics* (Cambridge University Press, 1995). p. 16

[58] Y.-H. Chen, F. Ripka, R. Löw, and T. Pfau, *Pulsed Rydberg four-wave mixing with motion-induced dephasing in a thermal vapor*, Appl. Phys. B **122(1)**, 1 (2016). p. 17

[59] G. Lindblad, *On the generators of quantum dynamical semigroups*, Communications in Mathematical Physics **48**, 119–130 (1976). p. 17

[60] T. Baluktsian, *Rydberg interaction between thermal atoms: van der Waals-type Rydberg-Rydberg interaction in a vapor cell experiment*, PhD thesis (Universität Stuttgart, 2013). p. 18

[61] P. Siddons, *Light propagation through atomic vapours*, Journal of Physics B: Atomic, Molecular and Optical Physics **47**, 093001 (2014). p. 22

[62] T. F. Gallagher, *Rydberg atoms*, Cambridge Monographs on Atomic, Molecular and Chemical Physics (Cambridge University Press, 1994). p. 23

[63] J. B. Balewski, A. T. Krupp, A. Gaj, D. Peter, H. P. Büchler, R. Löw, S. Hofferberth, and T. Pfau, *Coupling a single electron to a Bose–Einstein condensate*, Nature **502**, 664 (2013). p. 23

[64] T. F. Gallagher, *Rydberg atoms*, Reports on Progress in Physics **51**, 143 (1988). p. 24

[65] D. Tong, S. M. Farooqi, J. Stanojevic, S. Krishnan, Y. P. Zhang, R. Côté, E. E. Eyler, and P. L. Gould, *Local blockade of Rydberg excitation in an ultracold gas*, Phys. Rev. Lett. **93**, 063001 (2004). p. 24

[66] D. Comparat and P. Pillet, *Dipole blockade in a cold Rydberg atomic sample [invited]*, J. Opt. Soc. Am. B **27**, A208–A232 (2010). p. 24

[67] M. Saffman, T. G. Walker, and K. Mølmer, *Quantum information with Rydberg atoms*, Rev. Mod. Phys. **82**, 2313–2363 (2010). p. 24

[68] N. Šibalić, J. Pritchard, C. Adams, and K. Weatherill, *ARC: an open-source library for calculating properties of alkali Rydberg atoms*, Computer Physics Communications **220**, 319–331 (2017). pp. 27, 44

[69] R. B. Blackman and J. W. Tukey, *The measurement of power spectra from the point of view of communications engineering — part i*, Bell System Technical Journal **37**, 185–282 (1958). p. 30

[70] F. Beier, H.-J. Otto, C. Jauregui, O. de Vries, T. Schreiber, J. Limpert, R. Eberhardt, and A. Tünnermann, *1009nm continuous-wave ytterbium-doped fiber amplifier emitting 146w*, Opt. Lett. **39**, 3725–3727 (2014). p. 33

[71] E. D. Black, *An introduction to pound–drever–hall laser frequency stabilization*, American Journal of Physics **69**, 79–87 (2001). p. 34

[72] M. Seltenreich, *Eigenschaften eines digitalen, vielseitigen und erweiterbaren Systems zur Laserfrequenzstabilisierung*, Bachelor thesis (Universität Stuttgart, 2021). p. 36

[73] M. Fleischhauer, A. Imamoglu, and J. P. Marangos, *Electromagnetically induced transparency: optics in coherent media*, Rev. Mod. Phys. **77**, 633–673 (2005). pp. 36, 47

[74] iXblue, *MBC-DG-LAB manual*, `https://photonics.ixblue.com/sites/default/files/2021-02/MBC-DG-LAB_0.pdf`, accessed on 03.02.2022. p. 36

[75] R. Paschotta, J. Nilsson, A. Tropper, and D. Hanna, *Ytterbium-doped fiber amplifiers*, IEEE Journal of Quantum Electronics **33**, 1049–1056 (1997). pp. 36, 37

[76] S. Koppenhöfer, *Charakterisierung eines Lasersystems bei 420 nm zur Durchführung eines Experiments mit einzelnen Photonen*, Bachelor thesis (Universität Stuttgart, 2020). p. 52

[77] G. N. Gol'tsman, O. Okunev, G. Chulkova, A. Lipatov, A. Semenov, K. Smirnov, B. Voronov, A. Dzardanov, C. Williams, and R. Sobolewski, *Picosecond superconducting single-photon optical detector*, Applied Physics Letters **79**, 705–707 (2001). p. 52

[78] F. Moumtsilis, *Enhancing optical densities in vapour cells by light induced atomic desorption with nanosecond pulses*, Master thesis (Universität Stuttgart, 2021). pp. 55, 69

[79] A. Burchianti, A. Bogi, C. Marinelli, E. Mariotti, and L. Moi, *Light-induced atomic desorption and related phenomena*, Physica Scripta **T135**, 014012 (2009). p. 57

[80] S. S. Nekrashevich and V. A. Gritsenko, *Electronic structure of silicon dioxide (a review)*, Physics of the Solid State **56**, 207–222 (2014). pp. 57, 58

[81] J. A. Sedlacek, E. Kim, S. T. Rittenhouse, P. F. Weck, H. R. Sadeghpour, and J. P. Shaffer, *Electric field cancellation on quartz by Rb adsorbate-induced negative electron affinity*, Phys. Rev. Lett. **116**, 133201 (2016). p. 57

[82] T. E. Madey, B. V. Yakshinskiy, V. N. Ageev, and R. E. Johnson, *Desorption of alkali atoms and ions from oxide surfaces: relevance to origins of Na and K in atmospheres of Mercury and the Moon*, Journal of Geophysical Research: Planets **103**, 5873–5887 (1998). p. 57

[83] M. Oria, M. Chevrollier, D. Bloch, M. Fichet, and M. Ducloy, *Spectral observation of surface-induced van der waals attraction on atomic vapour*, Europhysics Letters (EPL) **14**, 527–532 (1991). pp. 57, 116

[84] V. Sandoghdar, C. I. Sukenik, E. A. Hinds, and S. Haroche, *Direct measurement of the van der waals interaction between an atom and its images in a micron-sized cavity*, Phys. Rev. Lett. **68**, 3432–3435 (1992). pp. 57, 116

[85] J. Cowin, D. Auerbach, C. Becker, and L. Wharton, *Measurement of fast desorption kinetics of d2, from tungsten by laser induced thermal desorption*, Surface Science **78**, 545–564 (1978). p. 58

[86] G. Wedler and H. Ruhmann, *Laser induced thermal desorption of carbon monoxide from fe(110) surfaces*, Surface Science **121**, 464–486 (1982). p. 58

[87] T. V. Perevalov and V. A. Gritsenko, *Application and electronic structure of high-permittivity dielectrics*, Physics-Uspekhi **53**, 561–575 (2010). p. 58

[88] A. Burchianti, A. Bogi, C. Marinelli, E. Mariotti, and L. Moi, *Optical recording in Rb loaded-porous glass by reversible photoinduced phase transformations*, Opt. Express **16**, 1377–1384 (2008). pp. 58, 59

[89] I. Lee, J. E. Parks, T. A. Callcott, and E. T. Arakawa, *Surface-plasmon-induced desorption by the attenuated-total-reflection method*, Phys. Rev. B **39**, 8012–8014 (1989). p. 58

[90] P. Noack, *Lichtinduzierte atomare Desorption mit Nanosekundenimpulsen*, Bachelor thesis (Universität Stuttgart, 2019). p. 61

[91] D. Malacara and A. Cornejo, *Testing of aspherical surfaces with Newton fringes*, Appl. Opt. **9**, 837–839 (1970). p. 65

[92] D. A. Steck, *Rubidium 85 D line data*, available online at `http://steck.us/alkalidata` (revision 2.2.3, 9 July 2021). pp. 79, 100, 101

[93] G. Comsa and R. David, *Dynamical parameters of desorbing molecules*, Surface Science Reports **5**, 145–198 (1985). p. 85

[94] H. Lorentz, *The theory of electrons and its applications to the phenomena of light and radiant heat*, Dover books on physics (Dover Publications, 2003). p. 99

[95] P. Siddons, C. S. Adams, C. Ge, and I. G. Hughes, *Absolute absorption on rubidium d lines: comparison between theory and experiment*, **41**, 155004 (2008). p. 100

[96] L. Weller, *Absolute Absorption and Dispersion in a Thermal Rb Vapour at High Densities and High Magnetic Fields*, PhD thesis (Durham University, 2013). p. 102

[97] C. Foot, *Atomic physics*, Oxford master series in physics (Oxford University Press, 2005). p. 102

[98] M. A. Zentile, J. Keaveney, L. Weller, D. J. Whiting, C. S. Adams, and I. G. Hughes, *Elecsus: a program to calculate the electric susceptibility of an atomic ensemble*, Computer Physics Communications **189**, 162–174 (2015). pp. 104, 107, 110

[99] I. Hughes and T. Hase, *Measurements and their uncertainties: a practical guide to modern error analysis* (OUP Oxford, 2010). p. 110

[100] C. I. Sukenik, M. G. Boshier, D. Cho, V. Sandoghdar, and E. A. Hinds, *Measurement of the casimir-polder force*, Phys. Rev. Lett. **70**, 560–563 (1993). p. 116

[101] H. Failache, S. Saltiel, M. Fichet, D. Bloch, and M. Ducloy, *Resonant van der waals repulsion between excited cs atoms and sapphire surface*, Phys. Rev. Lett. **83**, 5467–5470 (1999). p. 116

[102] R. Ritter, N. Gruhler, H. Dobbertin, H. Kübler, S. Scheel, W. Pernice, T. Pfau, and R. Löw, *Coupling thermal atomic vapor to slot waveguides*, Phys. Rev. X **8**, 021032 (2018). p. 124

[103] H. Alaeian, R. Ritter, M. Basic, R. Löw, and T. Pfau, *Cavity QED based on room temperature atoms interacting with a photonic crystal cavity: a feasibility study*, Applied Physics B **126**, 25 (2020). pp. 124, 127

[104] U. P. Dharanipathy, M. Minkov, M. Tonin, V. Savona, and R. Houdré, *High-Q silicon photonic crystal cavity for enhanced optical nonlinearities*, Applied Physics Letters **105**, 101101 (2014). p. 124

[105] R. H. Brown and R. Q. Twiss, *Correlation between photons in two coherent beams of light*, Nature **177**, 27–29 (1956). p. 124

[106] J. L. O'Brien, A. Furusawa, and J. Vučković, *Photonic quantum technologies*, Nature Photonics **3**, 687 (2009). p. 127

[107] S. Ghosh, A. R. Bhagwat, C. K. Renshaw, S. Goh, A. L. Gaeta, and B. J. Kirby, *Low-light-level optical interactions with rubidium vapor in a photonic band-gap fiber*, Phys. Rev. Lett. **97**, 023603 (2006). p. IV

Danksagung

Zum Schluss möchte ich mich bei allen bedanken, die durch ihre Unterstützung während der letzten Jahre zur Entstehung und zum Gelingen dieser Doktorarbeit beigetragen haben. Unter anderem möchte ich mich bedanken bei

- Prof. Tilman Pfau, der es mir als mein Doktorvater ermöglicht hat, das Single-Photon Projekt weiter zu führen - für seine Geduld und seine Ideen, wenn es mal nicht so schnell voran ging.
- Prof. Harald Giessen und Prof. Hans Peter Büchler für die Übernahme des Mitberichts bzw. des Prüfungsvorsitzes.
- Max Mäusezahl, Felix Moumtsilis, Annika Belz, Oliver de Vries, Artur Skljarow, Harald Kübler, Robert Löw und Hadiseh Alaeian für das Korrekturlesen dieser Arbeit.
- Robert Löw, Harald Kübler und Tilman Pfau für die Betreuung meiner Arbeit, für ihre motivierende Art und ihren immensen Erfahrungsschatz.
- Hadiseh Alaeian und Charles S. Adams, die in unseren Meetings immer wieder neue Ideen und Erklärungen zu unseren Messungen beigetragen haben.
- Fabian Ripka, von dem ich ein Experiment übernehmen durfte, welches modular weiterentwickelt werden konnte.
- Max Mäusezahl und Felix Moumtsilis, die das Experiment übernommen haben und es mit viel Motivation und Präzision fortführen.
- Hao Zhang für die effektive Zusammenarbeit und Planung der Zukunft des Experiments.
- Artur Skljarow für die Diskussion über dipolare Wechselwirkungen mit einzelnen Atomen.
- Annika Belz, Felix Moumtsilis, Philipp Noack, Benjamin Heinrich, Simon Koppenhöfer und Moritz Seltenreich, die im Rahmen ihrer

Master- und/oder Bachelorarbeiten motiviert zum Gelingen des Projektes beigetragen haben.

- Oliver de Vries und dem Team am IOF Jena für die Planung und Realisierung zweier Faserverstärker Systeme.
- Fabian Munkes, Harald Kübler, Daniel Weller und Nicolas Zuber für die ununterbrochene Unterstützung bei der institutsinternen IT-Infrastruktur.
- dem 3. Stock für die tolle Arbeitsatmosphäre und die regelmäßige gegenseitige Hilfe bei physikalischen und technischen Herausforderungen. Zudem bedanke ich mich für die gute Zusammenarbeit bei experiment-übergreifenden Projekten.
- allen Institutsmitgliedern für das außerordentlich freundschaftliche Arbeitsklima und die große Hilfsbereitschaft.
- Kati Kriesch, Karin Otter und Astrid Buck für das Erledigen sämtlicher Verwaltungsaufgaben und die Hilfsbereitschaft bei allem, was nicht mit Physik zu tun hatte.
- Thomas Dieterle und Christoph Braun, die mit mir seit dem ersten Tag das Physikstudium bestritten haben.
- meiner Familie, die mich jederzeit bei meinem Studium unterstützt hat und auch für eine gute Work-Life-Balance sorgte.